FUNDAMENTAL STUDY ON PERFORMANCE EVALUATION OF PROTECTION STRUCTURE FOR IMPACT BY ROCKFALL

Dissertation

FUNDAMENTAL STUDY ON PERFORMANCE EVALUATION OF PROTECTION STRUCTURE FOR IMPACT BY ROCKFALL

落石による衝撃に対する防護構造物の性能評価に関する基礎研究

Graduate School of
Natural Science and Technology
Kanazawa University

Division of Environmental Design

Student ID No. 1624052011

Name: TRAN LE HOANG TRUNG

Chief advisor: Prof. HIROSHI MASUYA

Date of Submission: June, 2019

Abstract

Natural hazards has always been an issue of concern owing to their dangerous influences on infrastructures, assets, and human lives. Therefore, strengthening for reinforced concrete (RC) structures or building up protection structures have been developed sharply in recent years. It can be said that externally bonded fiber-reinforced polymer (FRP) bars have been used to strengthen existing RC structures worldwide because this technique has been increased obviously the strength of slab, beam, and column in existing bridges and buildings. Moreover, many types of protection fence have been frequently built in mountain areas because these structures can perform an outstanding capacity for dissipating low-to-medium impact energy of rockfall in accordance to a rational arrangement of energy absorbers.

The main contents are to study the following: (1) the static and dynamic behaviors of RC beams strengthened by FRP bar in both experimental and numerical simulation models; (2) rockfall protection fences based on both experimental and analytical approaches; and (3) applicability for a performance based design involves RC beams strengthened FRP bar.

The main results mention that the externally bonded FRP bars to the tensile region of RC beams by near-surface mounted method has enhanced in the flexural strength of the beam. Strengthened beams performed well linear elastic behavior until the applied static load over 150 kN, and the tensile capacity of FRP bar can achieve nearly 50% its design capacity under ultimate load. Numerical simulation results agreed fairly well with experimental results; therefore, this study is considered to be preliminary in reference to the use of numerical models for replacing or modifying the parameters of the full-scale tests with externally bonded FRP systems. On the other hand, the experimental models of protection fence are designed rationally about the length of span, the height of posts, and the arrangement of energy absorbers as well. As expected, their dynamic behaviors regarding the absorbed capacity of impact energy, displacement, rope tensions, etc. performed perfectly.

Acknowledgments

Firstly, I would like to express my honest gratitude and high appreciation to my academic supervisor, Prof. Hiroshi Masuya, for his nonstop supports, valuable comments and helpful suggestions, which powerfully inspire me to pursue and finish perfectly the doctoral course at Kanazawa University. Moreover, my successful studies have been contributed importantly by Dr. Nishita, Ishii (Protect Engineering Ltd.,), Mr. Yamaguchi, Ohshita (Graduated students of Kanazawa University) and Vietnamese friends. I am deeply thankful to their enthusiastic assistances.

Finally, this thesis will close temporarily my study at Kanazawa University and will open a new page regarding the topic of dynamic behaviors for protection structures in my home land.

Contents

List of Figures

List of Tables

Chapter 1 Introduction

1.1 Objectives and scope of the study

Infrastructure is generally constructed to withstand its intended loading without failing due to fracture, deformation, or fatigue. To construct such structure, an engineer must first consider mechanical properties of used materials, such as toughness, strength, weight, hardness, and elasticity, and then determine the size and shape necessary for the material to support the desired load for a long life. Furthermore, reinforced concrete structure needs to perform well their flexural strength until the ultimate stage, or protection fence structure against rockfall need a high yield strength of wire net, an excellent flexural strength of posts, and a high rigidity of anchorages, etc. In addition, the entire structure must be able to support its load without the failure of weakest link because this plays an important role in the lifespan of structure.

Nowadays, a wide range of protective structures has been built like fence, net, shelf, rock shed, etc. to prevent the impact of rockfall as shown in Figure 1.1 (Masuya, 2008). Herein, the dynamic behavior of these structures under impact generally involves in the kind of structure and the dynamic characteristic of material closely. Therefore, there are further difficulties in the design of public structures due to many problems unsolved concerning impact behaviors of structures and dynamic characteristics of materials.

a) Fence

b) Net

c) Shelf

d) Rock shed

Figure 1.1 Typical protection structures against rockfall

Many countries including Japan, Italy, Switzerland, France, United States, and others, have developed many different types of protection structures. In Europe, different types of fences were constructed to establish many practical design and construction solutions, and to establish guidelines for the approval of rockfall protection kits (ETAG–027, 2008; Gerber, 2001; Peila and Ronco, 2009). In Japan, many impact tests have been conducted for rockfall protection structures to confirm their ultimate capacity (Tachibana et al., 2010; Berger et al., 2010; Masuya and Yamamoto, 1999) Correspondingly, the revised version of the handbook of rockfall measures (Japan Road Association, 2017) has been recently published in which the concept of performance-based design has been adopted.

Failure of structure involves in many types of problems that may not be easy to predict before or during the construction. However, the failure mostly can be traced to some of main causes. The first is that the structure is not strong and rigid enough to support the load, due to either its size, shape, or initial choice of material. If the structure or component is not strong enough, rapid damage can occur when the structure is loaded beyond its critical stress level. The second type of failure is from fatigue or corrosion, caused by instability in the geometry of structure, design miss, or insufficient material properties. These failures usually begin when cracks form on beams, column, and slab. These cracks grow as the material is repeatedly stressed and unloaded, eventually reaching a critical length and causing the structure to suddenly fail under normal loading conditions. The final cause of failure is from unexpected problems of natural hazards such as rockfall, landslide, typhoon, earthquake, and so on. These problems influence seriously on infrastructures, assets, and human lives.

Figure 1.2 shows the failure of rock shed at Etizen, Japan, July 1989 and the damaged protection wall of road at Yamanaka, Japan, December 2004. It can be seen that a large deformation of cracks and crushes appeared on these reinforced concrete (RC) structures under impact load of rockfall. Therefore, the study of various methods to strengthen RC structures is extremely necessary. One of popular methods is externally bonded Fiber Reinforced Polymer (FRP) bars because this method has been used to strengthen and reinforce existing concrete structures around the world since the mid-1980s. The number of projects using FRP bars worldwide has increased significantly since a few 20 years ago (Abdullah and Kadir, 2016; Fossum, 2000). This reinforcement was developed as an alternative method to traditionally external reinforcing techniques such as steel plate bonding and steel or concrete column jacketing. Technique including external post-tensioning and epoxy-bonding steel plates have been used successfully to increase the strength of slab, beam, and column in existing bridges and buildings. The advantages of composite materials involve in immunity to corrosion, a low volume to weight ratio, and many delivery shapes.

a) Collapse of rock shed

b) Disaster of new road by rockfall

Figure 1.2 Damage of protective structures

On the other hand, many rockfall protective structural countermeasures including galleries, embankments, nets, and fences have been developed, tested, and applied against the ravages of rockfall hazards. For the gallery and embankment, these structures seem to have a certain influence on the structure in service due to landslide, debris mass, and dead load covering on their body for a long time. For the net and fence, its mechanical behavior performed well when absorbing impact energy of rockfall. Impact energy is transferred through special connecting elements of protection fence to the relevant foundations. A key feature of protection fence is that the structure can absorb rather high energy levels through the development of large elasto-plastic of the system. This is achieved by the displacement of the wire net and the activation of the energy dissipating devices mounted on the connecting wire ropes (Figure 1.3(a)). Especially, the deformation of post also decreases significantly the impact energy of rockfall. However, the post of fence can badly damage when rock impact directly on it (Figure 1.3(b)). The posts of protection fence can made by steel, steel filled with concrete mortar or reinforced concrete. Therefore, the damage of post could address by the method of externally bonded FRP bars to tensile side of post because this technique has improved clearly the flexural and shear performance of concrete structures (Parretti and Nanni, 2004; W. Jung et al., 2017).

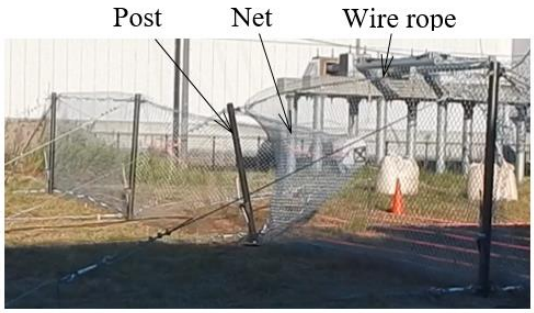

a) Deformation of net and wire rope

b) Damage of post

Figure 1.3 Structure of protection fence

1.2 Contents of research

This study consists of two main parts, reinforced concrete (RC) beams strengthened with fiber-reinforced polymer (FRP) bar by Near-Surface Mounted (NSM) method and protection fences against low-to-medium impact energy. They have been investigated to possibly treat the failure and damage of structure. For the time being, strengthening fiber-reinforced polymer (FRP) bar by Near-Surface Mounted (NSM) method has been used effectively and popularly in many types of structures against the deformation, high stress. To design such a structure with the ideal of performance-based design, it is necessary to evaluate the limitation capacity of structure as well as get insight into structural response. Experimental approach in cooperation with numerical simulation has been performed which can been thought the most rational economic and promising method. Basing on these points of view, this research generally focuses on the performance of RC beams strengthened with FRP bar by NSM method under static and impact load.

Besides studying the reinforcement RC structure by FRP NSM method, this topic studied also two types of protection fence against rockfall. It can be said that rockfall ricks as well as other natural hazards are evolving more uncertainty and frequently. Therefore, research on improving the capacity of rockfall protection structure basing on the better knowledge of structural insight behavior is importance and necessary. The recent researches on rockfall protection structures have obtained remarkable achievements so far, however, there have been some remained limitations, needed to advance. Among these limitations, dynamic behavior of devices absorbed impact energy and high flexible structures of posts or wire rope should be revealed more both experimental and analytical models.

It is generally considered that experimental results under limited conditions are not enough for practical measure, because it is impossible to cover all protection fences under various conditions of rockfall. Therefore, the utilization of numerical simulation to this kind of problem is investigated in this study. Numerical models is built in a new version of commercial software LS-DYNA in which there are many improved commands to model more conveniently and appropriately for both RC beams strengthened by FRP NSM method and protection fence. This constituted an effective and reliable design tool in order to study the impact behavior of general structures based on these analyses.

References

A. F. Fossum and J. T. Fredrich. Cap plasticity models and compactive and dilatant pre-failure deformation. American Rock Mechanics Symposum, 2000.

A. H. Abdullah, M. R. A. Kadir, "NSM FRP Reinforcement for Strengthening Reinforced Concrete Beams-Overview," ZANCO Journal of Pure and Applied Sciences, vol. 28, pp. 178-200, 2016.

R. Parretti and A. Nanni, "Strengthening of RC Members Using Near-Surface Mounted FRP Composite: Design Overview," Journal of Advances in Structural Engineering, Vol. 7 No. 5, 2004.

W. Jung, J. Park et al., "Flexural Behavior of Concrete Beam Strengthened by Near-Surface Mounted CFRP Reinforcement Using Equivalent Section Model," Journal of Hidawi, Advances in Materials Science and Engineering, Article ID 9180624, 2017.

Christoph Berger, Yoichi Nishita, Tomohiro Fujii, Full-scale testing of rock fall barriers for small-scale impact energy. Proceedings of the 10th Symposium on Impact Problem of Structures, Japan Society of Civil Engineering (2010)

Critina, G. Laura, G. Stefato, de M. Guido, G and Francesco, U. Three-dimensional numerical modelling rock protection barriers. Computers and Geotechnics. 44, 58–72 (2012)

ETAG-027, Guideline for European technical approval of falling rock protection kits, European Organization for Technical Approvals (2008)

Gerber W, Guide for the approval of rockfall protection kits. Swiss Agency for the Environment, Forests and Landscape (SAEFL) and Swiss Federal Research Institute WSL Berne (2001)

Japan Road Association, Rockfall Mitigation Handbook, Maruzen (2017)

Masuya, H., Performance based design of protection structure under impact action. Proceeding of International Symposium on Structure under Earthquake, Impact, and Blast Loading, 217–224 (2008)

Masuya, H. and Yamamoto, M., Load resistant factor of rock-sheds in heavy snow area. Proceeding of Joint Japan Swiss Scientific Seminar on Impact Load by Rock Falls and Design of Protection Structure, 121–127 (1999)

Chapter 2 Static and dynamic analysis of RC beams strengthened by FRP NSM method

In this chapter involves, the series of experiment and corresponding numerical simulation were investigated for static and dynamic behaviors of reinforce concrete (RC) beams strengthened with fiber-reinforced polymer (FRP) bars by near surface mounted (NSM) method. Besides evaluating the flexural static capacity of the strengthened beams, the main characteristics of impact at the different velocity levels for the beams strengthened with and without FRP NSM method were also discussed. In numerical simulation, the reliable assumptions of constitutive models and contact conditions of the beams were considered adequately, and the results in simulation compared carefully to that in experiment. It was shown that RC beams strengthened with FRP NSM method improved clearly their flexural capacity under static and impact load.

2.1 Overview

Externally bonded fiber-reinforced polymer (FRP) bars have been used to strengthen and reinforce existing concrete structures around the world since the mid-1980s. The number of projects using FRP bars worldwide has increased significantly a few 20 years ago because this reinforcement was developed as an alternative method to traditionally external reinforcing techniques such as steel plate bonding and steel or steel column jacketing. The technique has been applied to increase the strength of slab, beam, and column in existing bridges and buildings.

Nowadays, applying the technique of externally bonded FRP bars by Near-Surface Mounted (NSM) method becomes widespread (Alkhrdaji et al., 2000; Emmons et al., 2001). Figure 2.1 shows reinforcement by FRP bars for damaged bridge deck where FRP bars were used to not only sufficiently improve flexural capacity, but also effectively resist to the expansion of cracks of reinforced concrete structures.

Figure 2.1 Reinforced bridge deck by FRP bars

The main types of fibers used in civil engineering applications are Carbon Fiber Reinforced Polymer (CFRP), Glass Fiber Reinforced Polymer (GFRP), and Aramid Fiber Reinforced Polymer (AFRP). There are companies produced these materials including CarboDur (Sika Corporation), Forca Tow Sheet (Tonen Corporation), and Replark (Mitsubishi). High strength composite plates are known as an extension of the steel plating method. The advantages of composite materials involved in immunity to corrosion, a low volume to weight ratio, and many delivery shapes. The shape of FRP can be divided into bars, cables, 2-D and 3-D grids, sheet, plates, etc. CFRP material appeared at first to be one of the best approaches for the external strengthening of concrete structures. CFRP is composite materials built from the combination of carbon fiber and the epoxy resin matrix. Therefore, the composite possesses very high strength and elastic modulus in the fiber direction. Its fatigue properties are also outstanding, and the transversal strength of the composite is low, however, this drawback is not relevant for strengthening the application.

The CFRP Forca Tow Sheet was applied on Shirota Bridge in Kyushu province, Japan. Due to relaxing of the allowable loads (from 200 to 250 kN) the stress in flexural and shear reinforcing bars of the bridge slab exceeded the allowable limit of 1200 kg/cm^2. The CFRP strengthening was designed to reduce the stress below the allowable value. After the reinforcement, the measurements were done with the strain gauges mounted at flexural and shear reinforcing bars. The result attained a substantial decrease in deflection and stress by more than 30 %. To confirm the long-term reinforcing effect, the strain gauges were monitored over one year period. The results clearly indicate that the reinforcing effect is still effective after one year as discussed by A. Naaman et al., 1977.

There are some studies in terms of this technique performed to survey the behavior of structures strengthened by FRP bars. Recently, FRPs have replaced steel plates and emerged as a better material for externally strengthen for beams and columns. The members can gain better resistance and protection against environmental conditions (Abdullah and Kadir, 2016). This is a well-accepted technology that is becoming popular among designers and contractors because this technique has improved clearly the flexural and shear performance of concrete structures (Parretti and Nanni, 2004; W. Jung et al., 2017). Two popular types of FRP bars used for NSM method are round bars typically delivered to the site in the form of single bars or in a roll depending on bar diameter; rectangular bars or strip typically delivered to the site in a roll. The discovery of FRP NSM reinforcement open a new trend of research and engineering community because its benefits outweigh any drawbacks. It is easy to install into the grooves by epoxy resin or cement grout which cover effectively FRP bars against environmental impact because epoxy resin or cement grout can be used for its rapid setting and bond strength.

However, there are still a lot of drawbacks in order to effectively verify the behaviors of RC beams strengthened by FRP NSM method because many problems concerning directly the contact between FRP bars and concrete, and the dynamical properties of FRP bars have still remained unclear. This content can contribute a better understanding of the influence of FRP NSM method on both static and dynamic behaviors of RC beams. Additionally, numerical simulation had been done to reproduce successfully the static and dynamic behavior of the beams. These results are also premise to conduct further studies for impact issues in terms of different velocity levels and various strengthened methods on RC structures.

2.2 Fundamental data of the beams in static experiment

2.2.1 Test specimen detail

FRP bars to strengthen RC beams was produced by Forca Tow Anchors (FTA-C1-48-250 and FTA-C1-72-250) of Nippon Steel Sumikin Co., Ltd with initial shape of the sheet as shown in Figure 2.2(a). The total number of small strands in the sheet consists of two types, 48 and 72 carbon fiber strands (CFS). There were different stages to strengthen RC beams with the initial shape of fiber as a sheet by NSM method. Firstly, this sheet was mixed with epoxy resin as shown in Figure 2.2(b). After that, it was bonded into grooves made on the bottom concrete surface of beams as shown in Figure 2.2(c), in which the surface of grooves was prepared carefully as removing all dust and weak concrete. Finally, the FRP bar was buried in the groove as a rectangular bar with a length of 1.5 m (Figure 2.2(d)).

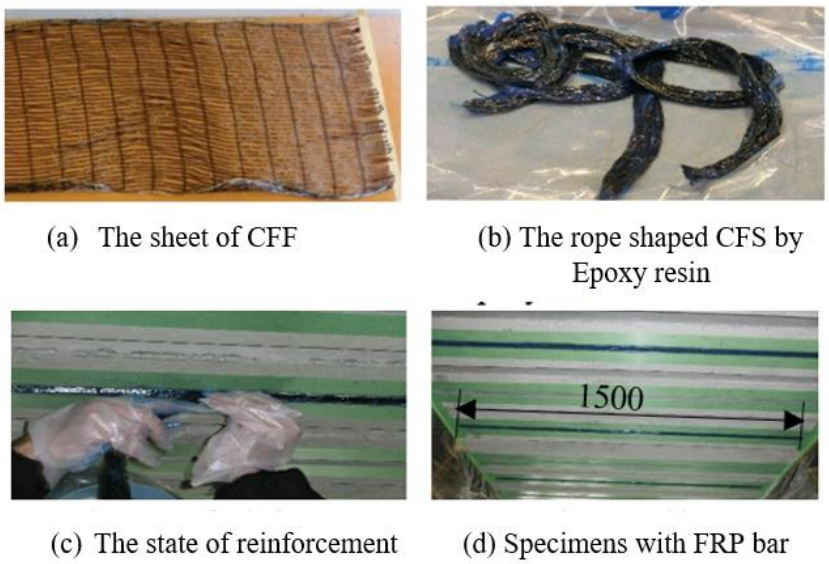

(a) The sheet of CFF

(b) The rope shaped CFS by Epoxy resin

(c) The state of reinforcement

(d) Specimens with FRP bar

Figure 2.2 Reinforced method

Table 2.1 and Table 2.2 respectively show material properties of FRP bar and reinforcing bars, and Figure 2.3 illustrates the detail of RC beams and the arrangement of reinforcing bars. The beam shown in Figure 2.3(a) is normal RC beams (SN1 and SN2) without the reinforcement of FRP NSM method. The beams shown in Figure 2.3(b) are RC beams with the reinforcement of NSM FRP of which names are SR48-1, S48-2 and S72-1, S72-2. They were strengthened with 48 and 72 CFs respectively by NSM method. After strengthening, the cross sections of 48 and 72 strands were 44 mm^2, 66 mm^2 respectively. All of the sections of concrete was rectangular with a wide of 200 mm, and a height of 300 mm. The length of specimens was 2200 mm. Main reinforcing bars of diameter 10 mm (D10) and 19 mm (D19) were arranged at upside and down side, respectively. The stirrups of diameter 13 mm (D13) were used. The span length of beams was 1600 mm and the length of FRP bars was 1500 mm.

Table 2.1 Material properties of FRP bars

Name	48 CFS	72 CFS
The total number of strands	48	72
Cross section (mm^2)	44	66
Young modulus (GPa)	237	237
Fineness - g - (g/km)	1650	1650
The number of filaments - K	24	24
Typical density (g/cm^3)	1.8	1.8
Ultimate tensile strength (MPa)	3990	3990

Table 2.2 Material properties of reinforcing bars

Name	D10	D13	D19
Yield strength (MPa)	295	295	345
Tensile strength (MPa)	431	431	494

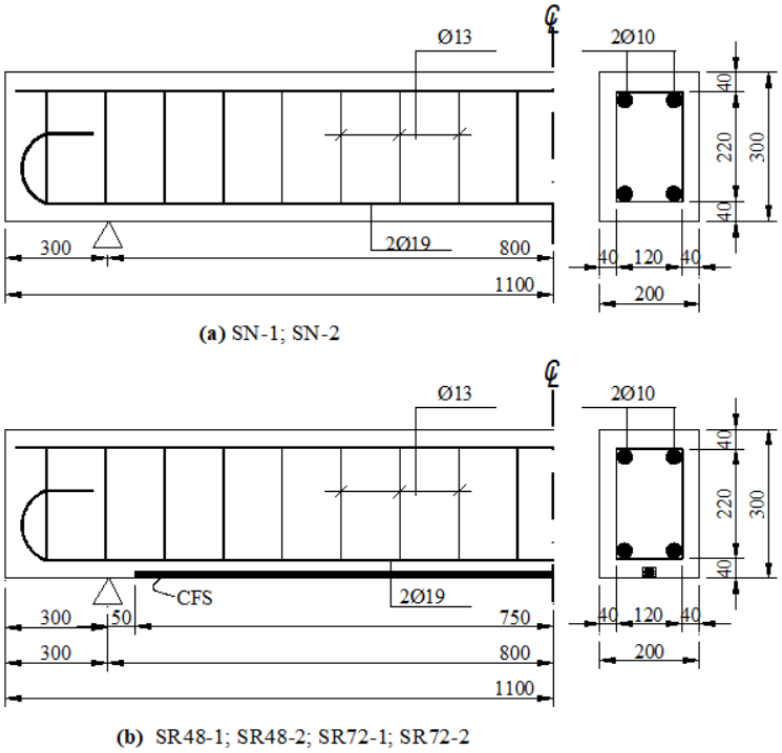

Figure 2.3 Detail of specimens (Unit: mm)

2.2.2 Test procedure

The loading test was performed to confirm the static behavior of RC beams strengthened by FRP bar and normal beams as shown in Figure 2.4. A 3000 kN hydraulic jack and one load cell were placed the middle of span for applying and measuring the imposed loading. In order to obtain the deflection properties of the entire specimen, displacement meters were installed vertically at the loading position. Moreover, strain gauges were also installed to confirm the strain variation of concrete, steel, and FRP bar.

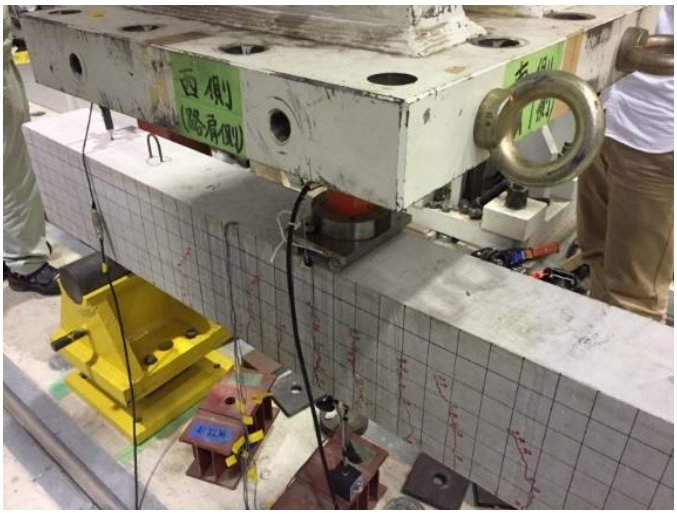

Figure 2.4 Static loading experiment

2.2.3 Crack patterns

Figure 2.5 presents the crack patterns of specimens. From the figures, it can be seen that the crack patterns of the tested beams under static load possessed mainly vertical (flexural) cracks. Most flexural cracks occurred around the bottom of the specimens; conversely, there is a few shear cracks appeared far away from the position of applied load and next to supports. It means that failures of all beams tested under static load were governed by both flexural and shear modes. In addition, the crack patterns of both RC beams strengthened by FRP NSM method and normal RC beams were distributed similarly. These cracks were observed carefully for all beams, their widths developed gradually when increasing the static load and their lengths extended from the bottom to the top of the beams. However, the crack patterns of strengthened beams, except for beam SR 72-2, exhibited smaller width and shorter length than that of normal beams when surveying at the middle of beams. It can be said that the strengthening of FRP by NSM method can lead to effective resistance to the expansion of cracks.

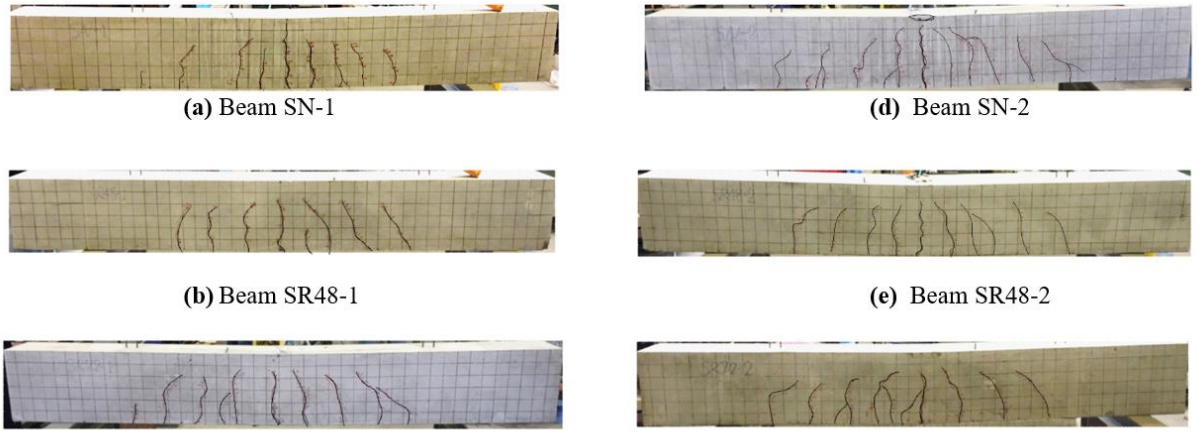

(a) Beam SN-1 **(d)** Beam SN-2

(b) Beam SR48-1 **(e)** Beam SR48-2

(c) Beam SR72-1 **(f)** Beam SR72-2

Figure 2.5 Distribution of cracks under static load

2.2.4 Load–displacement curves

The relationships between load and displacement in static experiments are shown in Figure 2.6. At the early stage of loading, the slope of curves of these beams was almost the same, which means that the contribution of FRP bars had not been activated yet. When the applied load was higher than 130 kN, the behavior of SN-1 and SN-2 no longer performed linear elastic stage because of the yield of rebars. While, the strengthened beams remained linear elastic behavior until the applied load over 150 kN. As expected, the beams strengthened by FRP bars performed better the flexural strength than the normal beams, especially for beam SR48-1 because this is one of strengthened beams exhibited high bending capacity with minimum displacement.

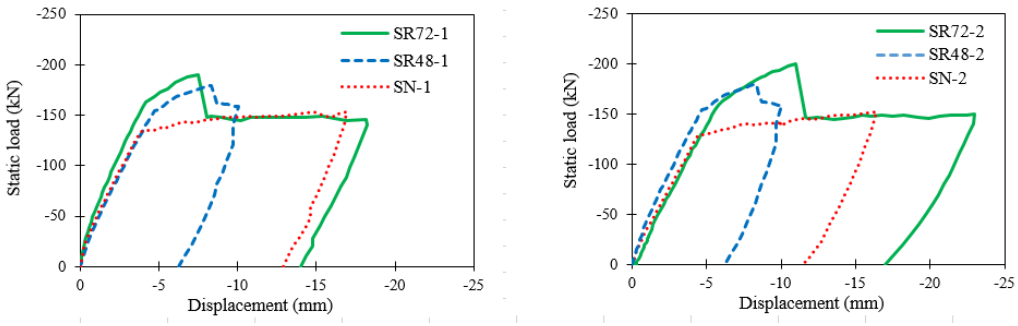

Figure 2.6 Static load-displacement relationship of experiment

Table 2.3 presents the yield loads and maximum loads in the experiment, where the range of maximum load of SR48 and SR72 is from 179 kN to 199 kN. While, the maximum load of SN2 and SN1 are 151 kN and 153 kN, respectively. Therefore, the increase in the maximum load of the strengthened beams is from 1.18 to 1.31 times compared with the normal beams. As a result, the flexural strength of the beams strengthened by FRP NSM method is greater than that of normal RC beams under static load. Moreover, it has become clear that an increase in the number of strands of FRP bars can leads to an increase in the flexural strength of RC beams.

Table 2.3 Experimental results

Specimens	Yield load (kN)	Maximum load (kN)
SN-1	134	153
SN-2	134	151
SR48-1	155 (155/134 =1.16)	179 (179/152 =1.18)
SR48-2	160 (160/134 =1.19)	188 (188/152 =1.24)
SR72-1	163 (163/134 =1.22)	190 (190/152 =1.25)
SR72-2	165 (165/134 =1.23)	199 (199/152 =1.31)

2.2.5 Load–strain curves

Figures 2.7 and 2.8 show the strain results of main rebars, concrete, and FRP bar obtained from the experiment. The strain results at each position of the main rebars shown in Figure 2.7 is the average values of strain gauges obtained from similar specimens. Overall, the variation of strain at the observed positions (L1, L2, U1 and U2) shows similar tendencies in both the cases without (SN) and with (SR48 and SR72) the use of FRP NSM method. Particularly, the strain of main rebars at the bottom region of cross-section (positions L1 and L2) performed tensile behaviors; whereas the top region (positions U1 and U2) showed compressive behaviors when the load was applied to the specimens.

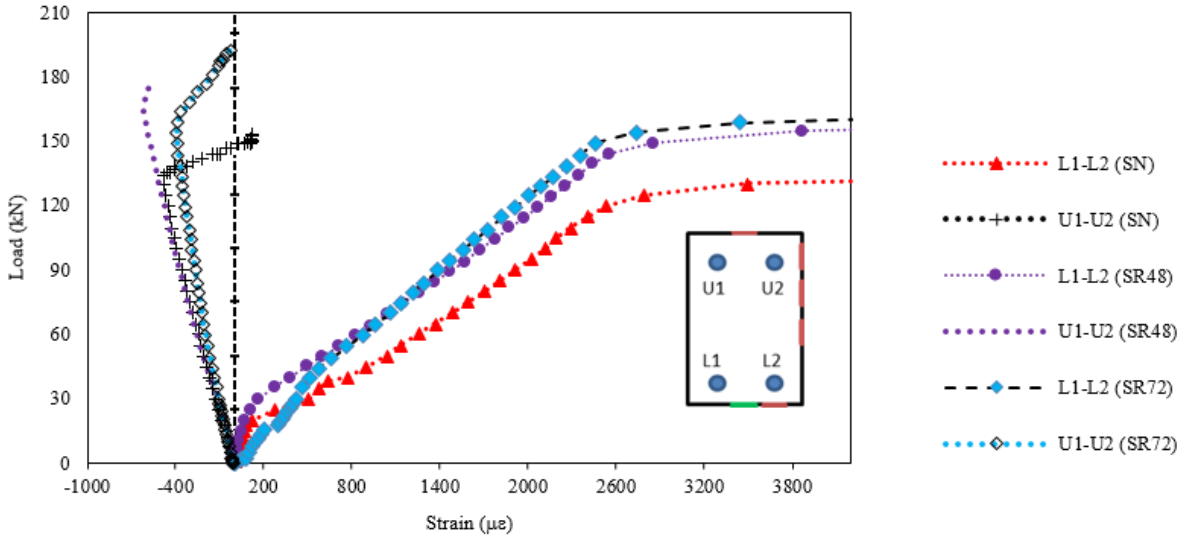

Figure 2.7 Load-strain relationships of main rebars

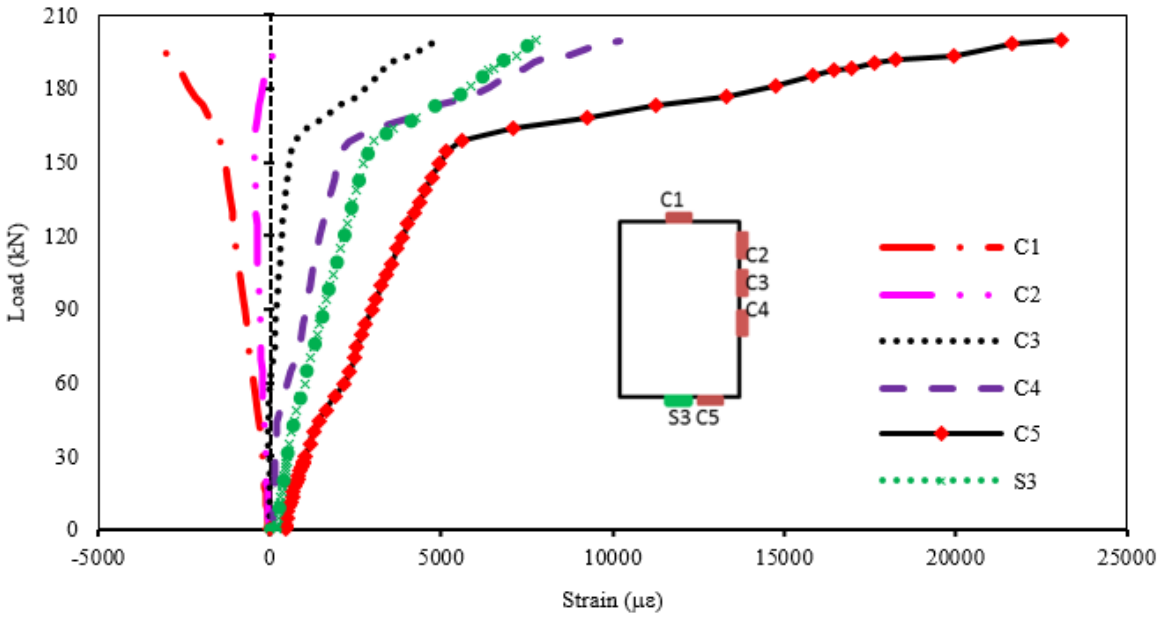

Figure 2.8 Load-strain relationships of concrete and FRP bar (SR72-2)

From Figure 2.7, the bottom rebars L1 and L2 performed yielding behavior when the applied load were 134 kN, 157 kN, and 164 kN for SN, SR48 and SR72, respectively. The corresponding strain values were measured to be about 2092 με, 2185 με, and 2074 με. Thus, the increase in the yield load is from 1.16 to 1.23 times, the difference in the obtained strain values is minimal. It can be noted that the presence of FRP bar leads to such a positive result for the yield of the main rebars at the bottom of the strengthened beams SR48 and SR72. In addition, positions U1 and U2 where compressive state occurred initially, and then this state became tensile direction because the neutral axis at the cross-section tended to shift the upper region as the load increased.

In addition, the strains of concrete and FRP bar were also observed at the mid−span of beam SR72-2 as shown in Figure 2.8. The strain of concrete at mid−span was measured in both compressive region (C1 and C2) and tensile region (C3, C4 and C5). As can be seen the tensile strain of concrete turned into rapidly growing when the load was applied, which caused the crack patterns as shown in Figure 2.5. In terms of the results calculated from the strain of concrete, the strains was 1582 με in compression (position C1), and 7074 με in tension (position C5). The neutral axis depth of the beam assumed the linear distribution of strain in the cross-section is approximately 55 mm at 163 kN.

Regarding the tensile deformation of FRP bar at position S3, the maximum tensile strain was measured to be ~7788 με at the final loading level (Load P_{max} = 199 kN) and the corresponding tensile stress was estimated to be 1845.76 N/mm^2, which is equivalent to about 46% of the ultimate tensile stress of FRP bar used (3990 N/mm^2). From this obtained result, it can be confirmed that the tensile capacity of FRP bar strengthened RC beam by NSM method can achieve nearly half its tensile capacity in design under ultimate load.

2.3 Performance of the beams under impact tests

2.3.1 Outline of impact tests

The material properties of concrete and reinforcing bars and FRP bars strengthened RC beams under impact tests is similar that of static tests. Specimens were also divide two types including normal beams (DN1 and DN2) and strengthened beams with 48 and 72 strands by NSM method (DR48-1, DR48-2 and DR72-1, DR72-2).

The free-falling devices for impact experiment were set up at the Structure Engineering laboratory of Kanazawa University (Figure 2.9). The various specimens were impacted respectively at the middle of span by a steel weight which was fallen along two guide rails from a specific height. The shape of weight used in the collision consists of a box solid, (800×300×240) mm with mass of 450 kg and a cylinder solid with r = 1407 mm in radius of curvature to contact. In addition, the positions of supports were installed by tie-down steel frames that can hold tightly on specimens, and prevent RC beams from bouncing out of the supports when occurring the impact.

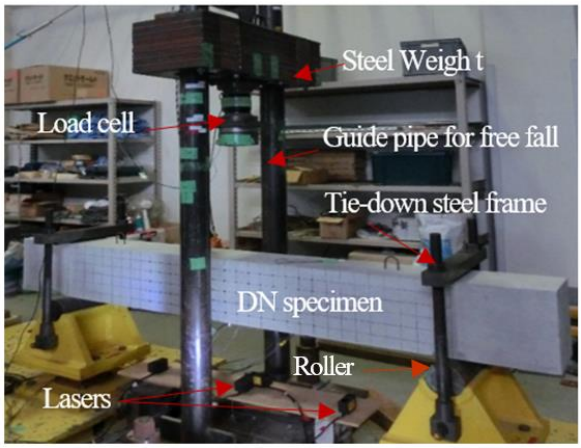

Figure 2.9 Apparatus of impact experiment

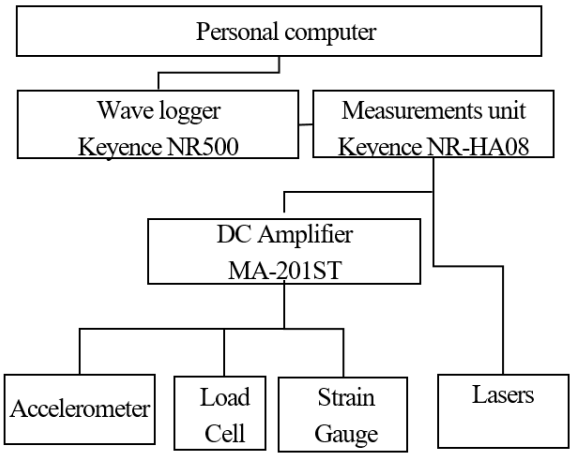

Figure 2.10 Measurement system

Regarding the impact velocity (V_{col}) for each specimens, beam DN-1 was carried out the repeated impact with V_{col} = 1 m/s, 2 m/s, 3 m/s, 4 m/s, 5 m/s respectively. Whereas, the remained beams were tested only the initial (single) impact, such as beams DN-2; DR48-1; DR72-1 with V_{col} = 5 m/s, and DR48-2, DR72-2 with V_{col} = 6 m/s. Measurement is presented in Figure 2.10. Used devices were an accelerometer (Kyowa Electronic Instruments Co., Ltd., AS-100HA), load cell (Kyowa Electronic Instruments Co., Ltd., LUK-1TBS), lasers (Keyence Corporation, LB300), and strain gauges (Tokyo Sokki Kenkyujo Co.,Ltd., FLA-10-11-3-LT). Concretely, an accelerometer was installed at the center of the weight to measure its acceleration. There are four lasers put under the specimens in order to measure the displacement of the beams. The impact force and reaction forces were confirmed by respective load cell, and the strain of concrete, steel and FRP bar were determined by the data from strain gauges. All output data was recorded by digital recorder with a rate 20 kHz for 0.5 second. Particularly, the high speed camera (300 frame/s) was placed at the most appropriate positions to monitor the interaction between the beams and steel weight.

2.3.2 Characteristic value of impact

Figure 2.11 illustrates the relation of impact force to time (*P-t*), and the relation of impact force to displacement (*P-δ*) of the beams. The characteristic values acquired from those relations:

- Impulse (I_p) is the one of physical amounts, which is gotten by the integration with impact force-time curve.
- The energy of impact (E_p) is the physical amount integrated with impact force-displacement curve.
- The mean impact force (P_m): impulse (I_p) divided by duration of impact force (T_d).

The characteristic values of impact are summarized in Table 2.4 and Table 2.5. From the results of No. 1 to No. 5, it was known that the maximum displacement (δ_{max}) of beam DN-1 as shown in Table 2.5 increased gradually corresponding to the increase of absorbed energy.

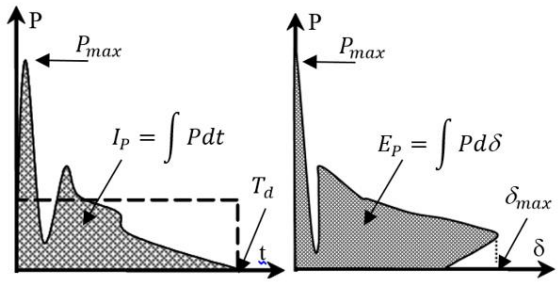

Figure 2.11 Impact force and characteristic values of impact

Table 2.4 Overview of impact test

No	Specimen	Falling weight (kg)	Impact velocity V_{col} (m/s)	Kinetic energy E_{col} (J)	Momentum M_{col} (Ns)
1	DN-1	450	1.0	225	450
2	DN-1	450	2.0	900	900
3	DN-1	450	3.0	2025	1350
4	DN-1	450	4.0	3600	1800
5	DN-1	450	5.0	5625	2250
6	DN-2	450	5.0	5625	2250
7	DR48-1	450	5.0	5625	2250
8	DR48-2	450	6.0	8100	2700
9	DR72-2	450	6.0	8100	2700

Table 2.5 Experimental results

No	Impulse I_p (Ns)	Duration time T_d (ms)	Mean force P_m (kN)	Absorbed energy E_p (J)	Displacement δ_{max} (mm)
1	728.6	12.9	56.5	143.0	1.5
2	1531.5	16.6	92.3	560.1	3.5
3	2119.3	17.8	119.1	1118.9	10.0
4	2563.1	20.6	124.4	2186.6	22.8
5	3092.8	22.1	139.9	2860.5	29.5
6	3006.0	20.6	145.9	2950.0	27.9
7	3052.7	19.6	155.8	2716.8	24.5
8	3580.5	23.1	155.0	3573.8	51.2
9	3572.0	23.2	153.9	4260.2	42.5

In addition, the maximum displacement (δ_{max} = 24.5 mm) of beam DR48-1 is clearly 12% smaller than that of beam DN-2, δ_{max} = 27.9 mm. The maximum displacement (δ_{max} = 42.5 mm) of DR72-2 is clearly 17% smaller than that of beam DR48-2, δ_{max} = 51.2 mm. This comparison indicates the effectiveness of applying FRP NSM method in improving the flexural capacity of RC beams as expected in advance, of which similar tendency was also reported (Norimitsu Kishi et al., 2017).

Cracks patterns are shown in Figure 2.12. Most bending cracks occurred in the bottom of the specimens; conversely, the formation of bending shear cracks appeared far away from impact position and next to supports. These cracks were observed carefully for all beams, their widths opened when increasing gradually the impact velocity, and their lengths developed from the bottom of the beams to the top. It is also interesting to note that there is small concrete fragmentation at the collision point, and the separation of FRP bar from concrete for beams DR48-1, DR48-2, DR7-1 and DR7-2 as shown in Figure 2.13.

In addition, the crack patterns of both RC beams strengthened with FRP NSM method and normal RC beams were distributed in two-third of the beam span, and the difference of distributable length was very small. However, the crack patterns of DR72-1 and DR72-2 exhibited smaller width and less bending cracks than other beams. It can be thought that an increase in the number of FRP bar to strengthen RC beams can lead to effective resistance to expansion of cracks.

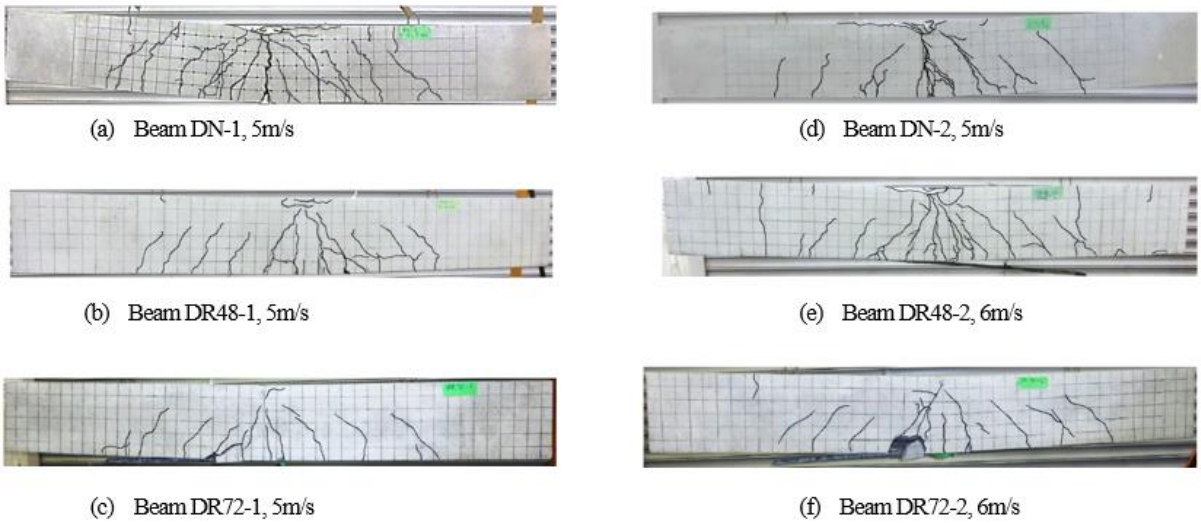

Figure 2.12 Distribution of cracks after impact

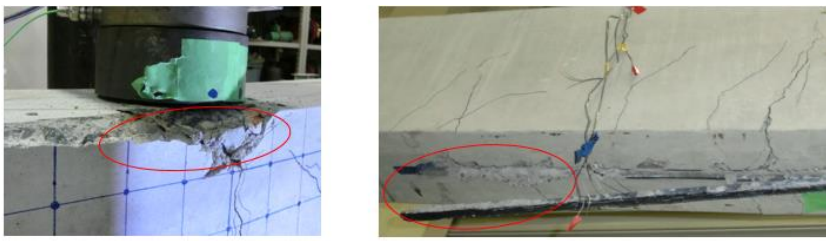

(a) Concrete fragmentation **(b)** Peeling of FRP bar

Figure 2.13 The failures of beam DR48-1, 5m/s

Table 2.6 The comparison of impact force and reaction force

Specimen	Impact velocity V_{col} (m/s)	Max impact force P_{max} (kN)	Reaction force R (kN)	R/P_{max}
DN-1	1.0	132.6	100.0	0.75
DN-1	2.0	286.1	212.3	0.74
DN-1	3.0	426.4	232.8	0.55
DN-1	4.0	570.3	245.7	0.43
DN-1	5.0	718.3	317.2	0.44
DN-2	5.0	764.5	341.1	0.45
DR48-1	5.0	699.7	282.1	0.40
DR48-2	6.0	784.3	426.3	0.54
DR72-2	6.0	828.7	360.6	0.44

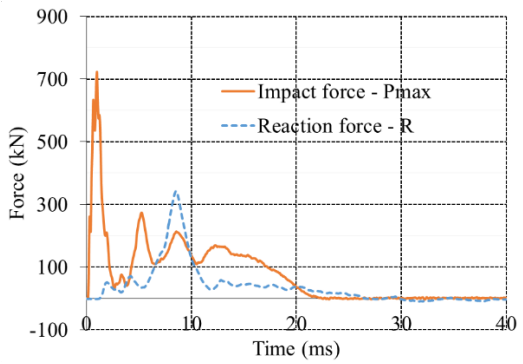

a) Beam DN-1, 5m/s

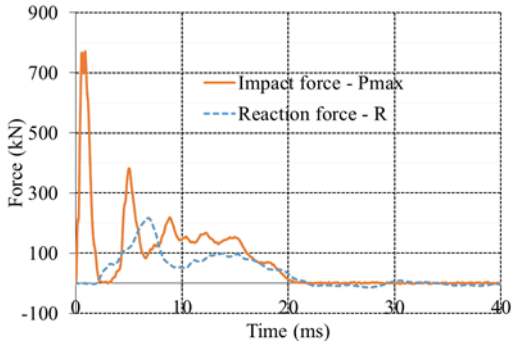

b) Beam DN-2, 5m/s

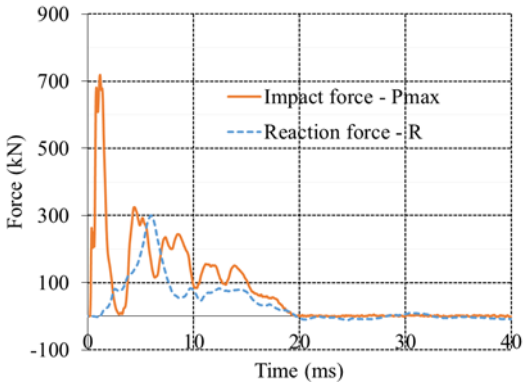

c) Beam DR48-1, 5m/s

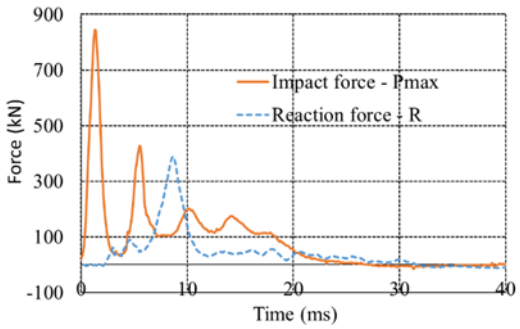

d) Beam DR72-2, 6m/s

Figure 2.14 Time history of impact force and reaction force

2.3.3 Impact force and reaction force.

The time response of impact force and reaction force is illustrated in Figure 2.14. The values of these forces is recorded exactly by load cells. The zero point of time axis corresponds to prompt in impacting. Table 2.6 shows the response rate of reaction force to impact force. The rate of DR48-2 is 0.54, while beam DR72-2 possesses the rate of 0.44. It can be said that the rise of number of FRP bar can lead to more slight fluctuation of waveforms.

Concrete differences between impact force and reaction force are shown in terms of maximum value, time, and fluctuation of waveforms in a period of 40 ms. In the first span from 0 ms to 10 ms, it can be seen that impact force and fulcrum reaction force peaked at about 1.5 ms and 5 ms respectively, and the maximum value of the reaction force occurred at the time when the wave of impact force rebounded. After that, these forces fluctuated lightly and decreased gradually from 10 ms to 20 ms, and both of them became minimal after 20 ms.

In addition, beams DN-1, DN-2 and DR48-1 with the impact velocity of 5 m/s , the time duration of impact force (T_d) of beam DR48-1 (19.6 ms) is less insignificant than that of beams DN-1 and DN-2 (22.1 ms and 20.6 ms respectively). Moreover, the maximum impact force of DR48-1 is approximately 96% value of DN-1 and its maximum value of reaction force is approximately 88% value of DN-1. As a result, the small different values of impact force, reaction force and the time duration lead to the small effectiveness of strengthening of FRP bar of 48 strands on RC beam. The differences may be caused by peeling of FRP bar after impact as shown in Figure 2.13(b).

2.4 Numerical simulation of the beams

Numerical simulation had been done to reproduce the static and dynamic behavior of RC beams with and without the strengthening of FRP NSM method. It would be possible to study such behavior of general structure by analysis. Finite element models (FEM) of the beams are illustrated in Figure 2.15 and Figure 2.16. These 3D models were built by various type of elements such as the concrete was meshed into 11400 eight-node solid elements with a size of 25 mm for static model, and into 67344 eight-node solid elements with size of 12.5 mm for dynamic model. Besides the beam elements were applied to model reinforcing bars, shell elements were modelled the static applied, and solid elements were used for a steel weight of impact. Moreover, solid elements were adopted to model FRP bars, which were designed to the cross section of 44 mm^2 and 66 mm^2 for beams SR48 (DR48) and SR72 (DR72), respectively.

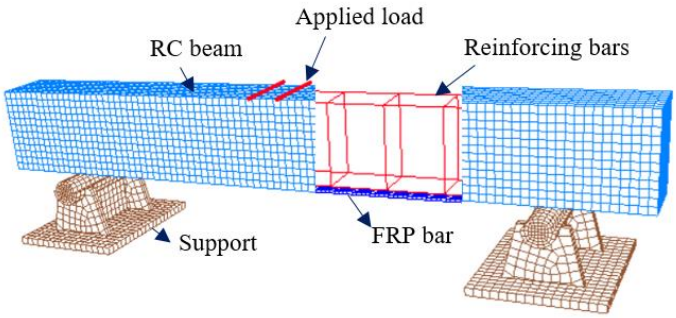

Figure 2.15 Static model of the beam built in LS-Dyna

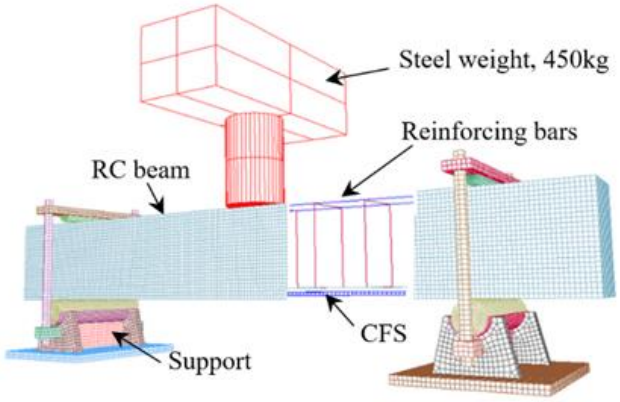

Figure 2.16 Dynamic model of the beam built in LS-Dyna

2.4.1 Constitutive model of concrete

Regarding theoretical background, concrete is a pressure dependent material, therefore, the general form of the yield function can be written as :

$$Y(I_1, J_2, J_3) = 0 \tag{2.1}$$

where I_1 1st invariant of stress tensor, which represents volumetric responses; J_2 and J_3 are the 2nd and 3rd invariants of deviatoric stress tensor and they account for deviatoric responses. In general, the primary difference between various concrete constitutive models is how the deviatoric and volumetric responses are characterized.

Karagozian & Case Concrete (KCC) model – Mat 072 for static models

Intended for analyzing RC structural responses to blast and impact loadings, the KCC model was initially developed in early 1990s in DYNA3D and was ported to LS-DYNA in 2004. This model allows automatic generation of all the parameters by inputting only the unconfined compressive strength and density of the concrete. It has been applied in analyzing many RC structures subjected to quasi-static, blast, and impact loads (Malvar et al., 1997, Crawford et al., 1997). A comprehensive model review and validation application is provided in Reference (Crawford et al., 2011).

The KCC model has three independent strength surfaces and they can be formulated in a generalized form as:

$$F_i(p) = a_{0i} + \frac{p}{a_{1i}+a_{2i}p} \tag{2.2}$$

where *i* stands for *y, m, r*. i.e., the yield strength surface, the maximum strength surface and the residual strength surface, and $p = -I_1/3$ is the pressure. a_{ji} ($j=0, 1, 2$) are parameters calibrated from test data. The default parameters are based on data presented in Reference (Joy and Moxley, 1993).

The failure surface is interpolated between the maximum strength surface and either the yield strength surface or the residual strength surface according to the following form:

$$F(I_1,J_2,J_3) = \begin{cases} r(J_3)\left[\eta(\lambda)\left(F_m(p) - F_y(p)\right) + F_y(p)\right] & \lambda(J_2) \le \lambda_m \\ r(J_3)\left[\eta(\lambda)\left(F_m(p) - F_r(p)\right) + F_r(p)\right] & \lambda(J_2) > \lambda_m \end{cases} \tag{2.3}$$

Here λ is modified effective plastic strain or the internal damage parameter, which is a function of J_2 and other parameters (such as damage evolution parameter, hardening parameter). η(λ) is a function of the internal damage parameter λ, with η(0)=0, η(λ)=1, and $\eta(\lambda \ge \lambda_{max})=0$. As can be seen in Figure 2.17, the material response is considered linear up until point 1 (yield strength). After yielding, a hardening plasticity response occurs until point 2 (maximum strength), is reached as λ increase to λ_m. After reaching the maximum strength, softening occurs until a residual strength as λ further increases up to λ_{max}, which is based on the amount of confinement, is obtained. $r(J_3)$ is a scale factor, which introduces the dependence to J_3 so that brittle (under low confinement) to ductile transition (under high confinement) is properly modelled.

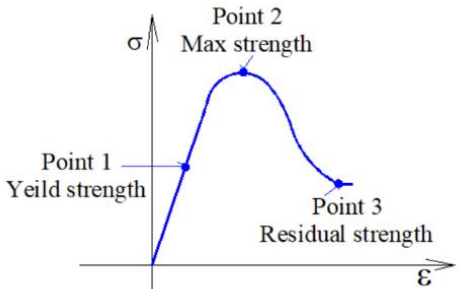

Figure 2.17 Strength model for concrete, Mat072

Continuous Surface Cap (CSC) Model – Mat 145 for dynamic models

The Continuous Surface Cap Model (MAT 145) proposed by Shwer and Murray is selected to model the concrete under impact load. This model can be expressed that the perfect combination of shear failure surface and compaction (cap) surface creates a smooth and continuous surface. This unique feature can prevent the separation of shear and volumetric

behaviors, and can capture the plastic volume growth. More importantly, the smooth of interaction position between the shear surface and cap surface can avoid an error in terms of excessive amount of time to analyze this position in simulation.

The Continuous Surface Cap Model treats plastic flow and accumulation damage as separate process derived from the theory of effective stress and strain equality in continuum damage mechanics. It is predicted that plastic flow is controlled by the shear stresses, which can capture stable deformation with maintaining modulus of elasticity. Meanwhile, accumulation damage involves the growth, interaction and combination of micro-cracks, micro-voids and similar faults in the micro-structure of concrete, which can cause a gradual decrease in the strength and modulus (Fossum and Fredrich, 2000; Hua and Jidong, 2015).

This model is formulated in terms of three stress invariants, as follows

$$I_1 = \sigma_1 + \sigma_2 + \sigma_3 \tag{2.4}$$

$$J_2 = \frac{1}{6}\{(\sigma_1 - \sigma_3)^2 + (\sigma_1 - \sigma_2)^2 + (\sigma_2 - \sigma_3)^2\} \tag{2. 5}$$

$$J_3 = \frac{1}{3} S_{ij} S_{jk} S_{ki} \tag{2.6}$$

Where I_1 is the first invariant of the Cauchy stress tensor, J_2 is the second invariant of deviator stress, and J_3 is the third stress invariant proposed by Rubin; the deviator stress tensor (S_{ij}) can be linked to the stress tensor (σ_{ij}) by $S_{ij} = \sigma_{ij}\ \delta_{ij}/3$.

The failure surface is illustrated in Figure 2.18(a) can be mathematically described by a combination of shear failure surface $F_f(I_1)$ and cap surface $F_c(I_1, \kappa)$, as follow

$$f(I_1, J_2, J_3, \kappa) = J_2 - R^2(I_1, J_3) F_f^2(I_1) F_c(I_1, \kappa) \tag{2.7}$$

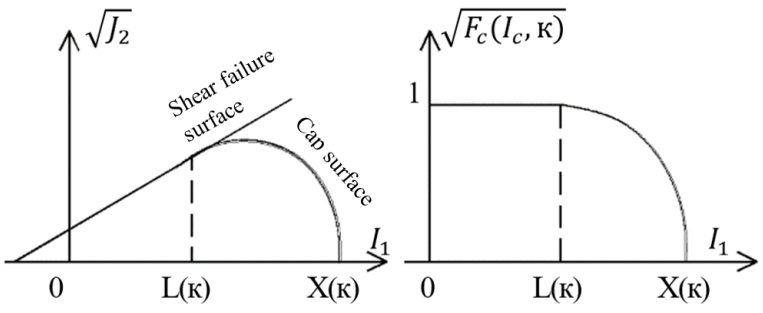

(a) (b)

Figure 2.18 Compressive meridional profile of the yield surface in the MAT 145: (a) Smooth cap failure function, (b) Non-dimensional function used for cap portion

where κ is cap hardening parameter, R (I_1, J_3) is the Rubin scaling function.

The shear failure surface $F_f(I_1)$ is given by Equation 2.8, and the cap surface $F_c(I_1, \kappa)$ in Figure 2.18(b) is given by Equation 2.9

$$F_f(I_1) = \alpha - \gamma\, exp(-\beta I_1) + \theta I_1 \tag{2.8}$$

$$F_c(I_1, \kappa) = 1 - \frac{(I_1 - L_{(\kappa)})\{|I_1 - L_{(\kappa)}| - (I_1 - L_{(\kappa)})\}}{2(X_{(\kappa)} - L_{(\kappa)})^2} \tag{2.9}$$

Regarding to the definition of damage in this model, there are two main types of damage including brittle and ductile damage. Brittle damage corresponds to the tensile mean stress and ductile damage corresponds to the compressive mean stress. The influence of failure mechanisms such as cracking in tension and crushing in compression can be controlled by the parameters of ductile and brittle damage (Hua Jiang et al., 2012).

In addition, "MAT_ADD_EROSION" function in LS-DYNA is employed to automatically remove concrete elements, which no longer contribute to resisting the impact force. The erosion is a numerical tool to avoid great mesh distortions. This erosion feature has been commonly adopted in studying the impact and blast response (LS-Dyna, 2010).

Moreover, this model is also regarded to model strain rate effects which may calculate the strength increase in concrete. A viscoplastic formulation with fluidity coefficient parameter is added to likely calculate the strength increase. The strain softening behavior for the cracks of concrete occurs at a post-peak decrease in strength. The elasto-plastic response can be recovered by setting the parameters of damage (Hua Jiang et al., 2012).

The Shwer & Murray cap model (A three-invariant smooth cap model) was used. There are 12 parameters α_i, β_i, γ_i, and θ_i $(i = 1, 2, 3)$ defined to the shear failure surface. Five parameters W, D_1, D_1, X_0, and S use for the cap surface, and four parameters A^+, B^+ and A^-, B^- for damage. The parameters used in this study are presented in Table 2.7. Mass density ρ = 2500 kg/m^3, Young's modulus E = 28.43 MPa, Poisson's ratio ν = 0.167, compressive strength f_c' = 35.81 MPa for the mechanical properties of concrete material were used.

2.4.2 Constitutive model of reinforcing bars and CFS

For the constitutive model of reinforcing bars, an elastic-plastic material model called "Mat Piecewise Linear Plasticity" (Mat 24) is adopted to model the reinforcing bars. The kinematic hardening behaviors is considered in this model, that is predicted the yield surface remains constant in size and translates in the direction of yielding (LS-Dyna, 2010), as shown in Figure 2.19.

In addition, this model also allows users to define parameters for the strain rate curve. Under impact and blast loads, the relation of dynamic increate factor (DIF) to strain rate needs to be adopted because the strength increase of the reinforcing bars was observed up to more than 50% (Malvar and Crawford, 1998). The DIF for reinforcing bars defined by Malvar is used in this simulation.

The relationship between both the tensile and compressive strength DIF of steel and strain rate is given by the following Eq. 5

$$DIF = \left(\frac{\dot{\varepsilon}}{10^{-4}}\right)^{\alpha} \tag{2.10}$$

Here, $\alpha = 0.074 - \frac{0.04 f_y}{414}$.

where, f_y is yield stress of reinforcing bars as shown in Table 2. Mass density ρ = 7850 kg/m^3, Young's modulus E = 200 MPa, Poisson's ratio ν = 0.3 for steel material were used.

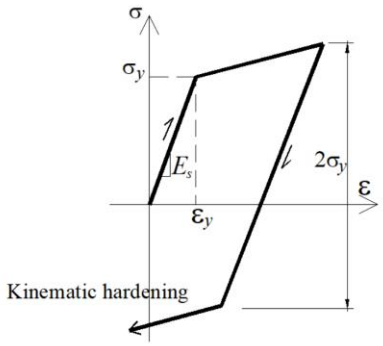

Figure 2.19 The model of elastic-plastic behavior with kinematic hardening

Table 2.7 Parameters setting of the concrete model

α	θ	γ	β	X_0	D_1	D_2
9.62	0.34	4.28	0.04	84.84	6.1e-4	2.2e-6
α_1	θ_1	γ_1	β_1	W	S	A^-
0.82	0.00	0.24	0.01	0.07	2.15	1.00
α_2	θ_2	γ_2	β_2	B^-	A^+	B^+
0.76	0.00	0.26	0.01	0.10	1.00	2.51

For the constitutive model of CFS, the stress-strain relationship of CFS is shown as elastic behavior via experimental observation. Therefore, the LS-DYNA material model named "Mat

Elastic" (MAT 001) is selected, in which the ultimate strength f_u, strain ε_u and Young's modulus E are 3990 MPa, 0.017 m/m and 237 GPa, respectively.

2.4.3 Contact conditions

This model consists of different components including steel weight, concrete, reinforcing bars, FRP bar, and supports. They interacted to each other to transfer impact wave and dissipate energy. Thanks to this, the precise reproduction of contact behaviors between those components might be an essential factor. The interactions used in the models are divided into two following groups. (1) Automatic surface to surface, assigned for reaction between steel weight and concrete, support and concrete; (2) Automatic surface to surface tiebreak, contacted between FRP bar and concrete. On the other hand, the method of incorporating reinforcing bars into the concrete was described by Constrained Lagrange in Solid technique.

The LS-DYNA contact algorithm named "Contact Automatic Surface to Surface" is employed to simulate the contact between the steel impactor and the beam, and between the supports and the beam. This technique allows to create pairs of surfaces that can connect the nodes on the surfaces together during the analysis (LS-Dyna, 2010).

On the other hand, the technique "Constrained Lagrange in Solid" effectively addresses penalty coupling of beams to solid elements, in which the slave sets for the beam elements of reinforcing bars and the master sets for the solid elements of the beam (LS-Dyna, 2010).

Tiebreak contact is used to model the slip relationship between concrete and FRP bar. The tiebreak allows the separation of the surfaces under tensile load by setting the parameters of tensile failure strength (NFLS) and shear failure strength (SFLS). These parameters are typical properties for epoxy adhesives. In this simulation, NFLS = 56 MPa, and SFLS = 44 MPa are applied (Demetrios M. Cotsovos, 2010).

2.5 Comparison of experiment and simulation

2.5.1 Static models

Figure 2.20 shows the relations of static load to displacement in the experiment (Exp) and numerical simulation (FEM) Overall, the curves and values of yield load and maximum load were in good agreement for all cases. Regarding normal RC beam, the yield and maximum load of the simulation are 136 kN and 150 kN respectively, which is approximately experimental values. The displacement peaks at around 16 mm for both simulate and experiment. It became clear that the static behavior of model SN in simulation is similar that of the test. In addition, the results of models SR48 and SR72 also tend to be similar together. The maximum load of SR48 in simulation (P_{max} = 180 kN) is 4.3 % smaller than that of experiment (P_{max} = 188 kN for SR48-2), and the maximum load of SR72 in simulation (P_{max} = 192 kN) is 3.5 % smaller

than that of experiment (P_{max} = 199 kN for SR72-2). The deviations of maximum loads are minimal when comparing between experimental and numerical values.

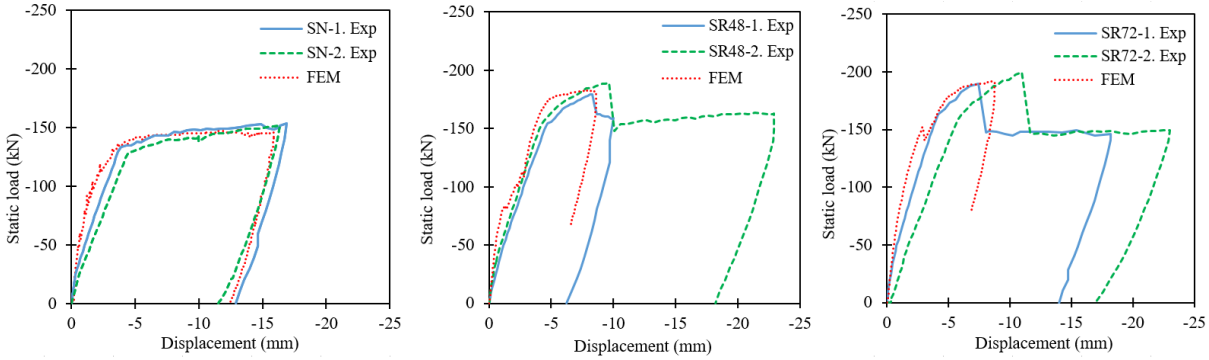

Figure 2.20 Load- Displacement relationship

2.5.2 Dynamic models

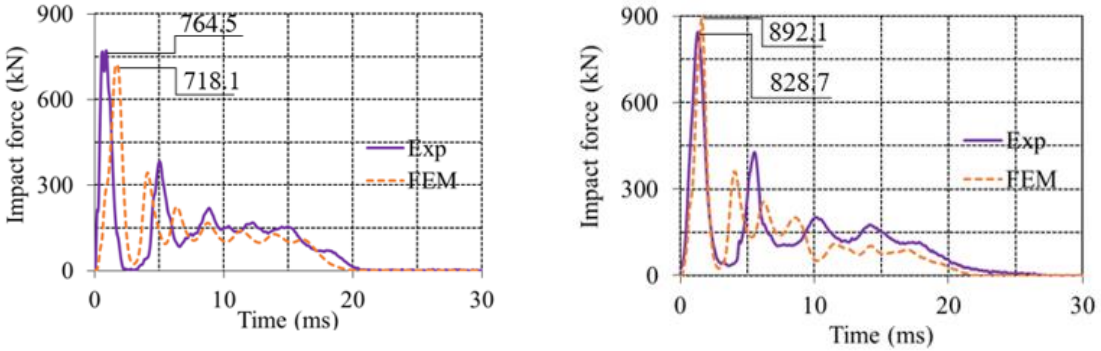

(a) DN-2, 5m/s (b) DR72-2, 6m/s

Figure 2.21 Comparison of impact force-time duration curve

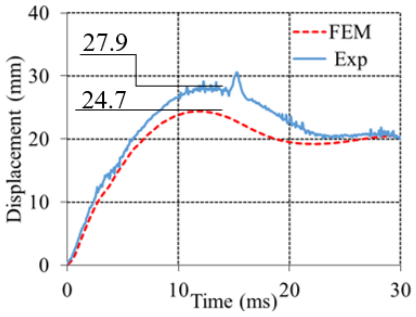

Figure 2.22 Displacement-time duration curve of DN-2, 5m/s

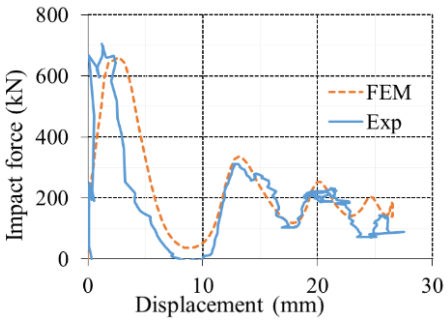

Figure 2.23 Impact force-displacement curve of DR48-1, 5m/s

Table 2.8 Summary values between experiment and simulation under impact load

Type	Impact velocity [m/s]	Impact force of Exp [kN]	Impact force of FEM [kN]	Displac-ement of Exp [mm]	Displac-ement of FEM [mm]
DN-2	5	764.5	718.1	27.9	24.7
DR48-1	5	699.7	675.2	24.5	22.5
DR48-2	6	784.3	807.5	51.2	48.3
DR72-2	5	828.7	892.1	42.5	39.6

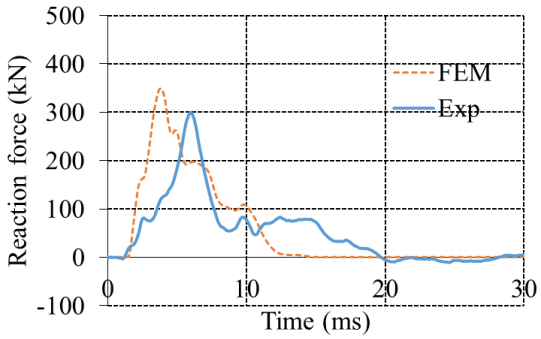

Figure 2.24 Fulcrum reaction force-time curve of DR48-1, 5m/s

The time histories of impact force of DN-2, 5m/s and DR72-2, 6m/s as shown in Figure 2.21. Summary values of impact force and displacement between experiment and simulation is shown in Table 2.8. It became clear that, the shape of waves and the maximum values were in good agreement. For impact force, the maximum value of experiment (P_{max} = 764.5 kN) is 6.0 % larger than that of simulation, P_{max} = 718.1 kN for DN-2, 5 m/s in Figure 2.21a, and the maximum value of DR72-2, 6m/s in experiment (P_{max} = 828.7 kN) is 7.1 % smaller than that of simulation, P_{max} = 892.1 kN in Figure 2.21b. so the deviations of impact force is insignificant.

The time histories of displacement of DN-2, 5m/s as shown in Figure 2.22, and the relationship of impact force and displacement of DR48-1, 5m/s is illustrated in Figure 2.23**.** For displacement in Figure 2.22, the slope of the curves between experiment and analysis is almost the same at the early stage of impact for DN-2, 5 m/s. It can be seen that these maximum displacement peak at the same time of around 12 ms, and the value of simulation, δ_{max} = 24.7 mm is 11% smaller than that of experiment, δ_{max} = 27.9 mm. This small difference can be considered to define the ductile and brittle damage for the model MAT 145 of concrete. For the relation of impact force to displacement in Figure 2.23, beam DR48-1, 5 m/s is definitely compatible because their fluctuation is the same not only in the initial wave, but also in the subsequent vibrating waveform.

On the other hand, the comparison of fulcrum reaction force between experiment and analysis is shown in Figure 2.24. The shape of reaction force from the analysis seems to be a little difference than that from the experiment. The maximum values of this force in the analysis is higher and its waveform ends earlier than that in experiment. This difference can be caused by the contact between the rollers of support and the surface of the concrete, which was not perfectly flat and smooth in the test as compared to that of the numerical model.

2.6 Summary of outcomes

In this chapter, the static and dynamic behaviors of RC beams with and without the strengthening of FRP NSM method performed in both experimental and numerical models. The achievements of research are summarized as follows:

1) It has been concretely shown that externally bonded FRP bars to the tensile region of RC beams by NSM method has enhanced clearly in the flexural strength, and resisted to the expansion of cracks under static and impact loading condition
2) Beam SR48-1 is one of the reinforced beams performed the clearest linear elastic behavior until the applied static load over 150 kN
3) The use of FRP bar can create positive influence on the yield of the main rebars at the bottom of the strengthened beams SR48 and SR72 under static load
4) The tensile capacity of FRP bar strengthened RC beam by NSM method can achieve nearly half its tensile capacity in design under ultimate load
5) Regarding dynamic models, RC beams strengthened with FRP bar or normal RC beams were conducted with a weight of 450 kg, and impact velocity from 1 m/s to 6 m/s. The maximum displacement of strengthened beam is clearly 12% smaller than that of normal beam, so the presence of FRP bar leads to such a positive result for the deformation of strengthened beams.
6) The strengthened beams finally discontinued due to peeling of FPR bars from the substrate. The occurrence of bonding failure at the epoxy-concrete interface in terms of the specimens strengthened by FRP NSM method is difficult to control when impact with high speed
7) The values of impact force, reaction force and the time duration is insignificantly different when comparing between normal beams and strengthened beams. The reinforcement of FRP NSM method do not positive effect on these impact characteristic.
8) The assumptions involved the constitutive models and contact conditions of the components of beam were adopted adequately in numerical analysis

9) Numerical simulation results agreed fairly well with experimental results, and this constituted an effective and reliable design tool in order to study the static and dynamic behavior of general structures based on these analyses

This research contributes a better understanding of the influence of FRP NSM method on the static and dynamic behaviors of RC beams. This study is considered to be preliminary in reference to the use of numerical models for replacing or modifying the parameters of the full-scale tests with externally bonded FRP systems. Additionally, the results of the study are also premise to conduct further studies for impact issues in terms of higher velocity levels and various strengthened methods on RC structures.

References

A. F. Fossum and J. T. Fredrich. Cap plasticity models and compactive and dilatant pre-failure deformation. American Rock Mechanics Symposum, 2000.

A. H. Abdullah, M. R. A. Kadir, "NSM FRP Reinforcement for Strengthening Reinforced Concrete Beams-Overview," ZANCO Journal of Pure and Applied Sciences, vol. 28, pp. 178-200, 2016.

A. Naaman, S. Y. Park, M. Lopez et al., "Glued-on fiber reinforced plastic (FRP) sheets for repair and rehabilitation," The University of Michigan, Department of Civil and Environmental Engineering, MI 48109-2125, 1977.

Crawford, J.E., Magallanes, J.M., Lan, S., and Wu, Y. "User's manual and documentation for release III of the K&C concrete material model in LS-DYNA," TR-11-36-1, Technical Report, Karagozian & Case, Burbank, CA, November, 2011

Crawford, J.E., Malvar, L.J., Wesevich. J.W., Valancius, J., and Reynolds, A.D. "Retrofit of reinforced concrete structures to resist blast effects," *ACI Structural Journal*, vol. 94, p371-377, 1997

Demetrios M. Cotsovos. A simplified approach for assessing the load-carrying capacity of reinforced concrete beams under concentrated load applied at high rates. International Journal of Impact Engineering 37 (2010) 907-917.

Guide for the Design and Construction of Externally Bonded FRP Systems for Strengthen Concrete Structures" of ACI 440.2R-08.

Hua Jiang, Jidong Zhao. Calibration of the continuous surface cap model for concrete. Finite Elements in Analysis and Design 97 (2015) 1-19.

Hua Jiang, Xiaowo Wang, Shuanhai He. Numerical simulation of Impact test on reinforced concrete beam. Material and Design 39 (2012) 111-120.

Kritsada Srikho, Hiroshi Masuya, Akira Sato and Sachio Nakamura. Fundamental study on evaluation of deflection of H-beam under impact load aimed for the performance based design. Journal of Structural Engineering Vol 58.A, March 2012, 991-999.

Leonard E Shwer, Yvonne D Murry. Continuous surface cap model for geometrical modeling. 7th International LS-DYNA Users Conference, and 2. A. F. Fossum and J. T. Fredrich.

LS-DYNA Keyword user's manual Ver. 971, Livermore Software Technology Corporation, LSCT, 2010.

Malvar L, Crawford J. Dynamic increase factor for steel reinforcing bars [C]. 28th DDESB Seminar Orlando, USA; 1998.

Malvar, L.J., Wesevich, J.W., and Crawford, J.E. "Procedures for including fragment loading and damage in the response predictions of reinforced concrete slabs," Eighth International Symposium on Interaction of the Effects of Munitions with Structures, McLean, VA, April 1997

Norimitsu Kishi, Masato Komuro, Yusuke Kurihashi, Hiroshi Mikami, Takashi Funaki. Experimental study on upgrading of impact resistant capacity for RC beams strengthened with NSM-AFRP rods. Civil Engineering Society, 2017.

R. Parretti and A. Nanni, "Strengthening of RC Members Using Near-Surface Mounted FRP Composite: Design Overview," Journal of Advances in Structural Engineering, Vol. 7 No. 5, 2004.

Rubin MB. Simple, convenient, isotropic failure surface. J Eng Mech (1991); 117 (2): 348-569.

Sayoko Tachibana, Hiroshi Masuya and Nakamura. Performance based design of reinforced concrete beams under impact. Natural Hazards and Earth System Sciences 10 (2010) 1069-1078.

Thong M Pham and Hong Hao. Behavior of fiber-reinforced polymer-strengthened reinforced concrete beams under static and impact loads. International Journal of Protective Structures 2016, 1-22.

W. Jung, J. Park et al., "Flexural Behavior of Concrete Beam Strengthened by Near-Surface Mounted CFRP Reinforcement Using Equivalent Section Model," Journal of Hidawi, Advances in Materials Science and Engineering, Article ID 9180624, 2017.

Weichen Xue, Yuan Tan and Lei Zeng. Flexural response predictions of reinforce concrete beams strengthened with pre-stressed CFRP plates. Composite Structures 92 (2010) 612-622.

Yinzhi Zhou, Mingkang Gou, Fengyu Zhang, Shoujun Zhang and Dan Wang. Reinforced concrete beams strengthened with carbon fiber reinforced polymer by friction hybrid bond technique: Experimental investigation. Materials and Design 50 (2013) 130-139.

Chapter 3 Dynamic behavior of rockfall protection fence

Essential requirements for the protection of structures in mountainous areas against rockfalls have led to the development of various types of protection fences. Herein, a series of impact tests conducted on the protection fence by changing the heights of posts, the lengths of spans and collision positions to evaluate adequately and precisely the absorbable capacity of the impact energy. In all experimental cases, the protection fence, which built both vertically and horizontally, exhibited an outstanding capacity for dissipating low-to-medium impact energy in accordance to a rational arrangement of energy absorbers, which caused the effective slipping of wire ropes. Additionally, the simplest possible assumptions adopted in numerical simulations are presented clearly and in detail in terms of the choice of finite element shapes, constitutive laws, and contact conditions, so that the model of the numerical simulation can reproduce successfully the dynamic behavior of the protection fence. Furthermore, this numerical model can aid or replace the full-scale tests to attain an improved capacity for absorbing the energy of rockfall.

3.1 Overview

Natural hazards has always been an issue of concern owing to their dangerous influences on infrastructures, assets, and human lives. Therefore, protective structures, such as protection fences, have been developed in recent years against rockfalls. The principal advantages of a protection fence are its rapid erection and easy maintenance. Many different types of protection fences have developed in various countries including Japan, Italy, Switzerland, France, United States, and others. In Europe, different types of fences were constructed to establish many practical design and construction solutions, and to establish guidelines for the approval of rockfall protection kits (ETAG–027, 2008; Gerber, 2001; Peila and Ronco, 2009). In Japan, a wide rage of impact tests has been conducted for rockfall protection structures to confirm their ultimate capacity (Tachibana et al., 2010; Berger et al., 2010; Masuya and Yamamoto, 1999; Masuya, 2008). Correspondingly, the revised version of the handbook of rockfall measures (Japan Road Association, 2017) has been recently published in which the concept of performance-based design has been adopted.

Conversely, developing designs based on the use of various computer programs is playing a key role in the study and design of the structures of protection fences. The software ABAQUS is used to model a typical dynamic event of a net barrier against rockfall (Spadari et al., 2011; Critina et al., 2012). These models can be useful in supplementing real-scale tests when the barrier needs to be investigated at different impact conditions. The software FARO is also used to reproduce the falling rock as a rigid body by using a special contact algorithm for the interaction with the barrier, and the simulation can address effectively the connection of net elements and rope elements (Axel, 2005). The software LS–DYNA is one of the most popular programs used to analyze the dynamic behavior of protective structures (Berger et al., 2011; Tam and Masuya, 2013; Dhakal et al., 2011; Phuc et al., 2012). The characteristic values of collision, such as the impact force, displacement, kinetic energy, and others, can be verified and compared adequately and rationally using this program.

This study deals with the protection fence against rockfalls with low-to-medium impact energy, as shown in Figure 3.1. These fences have many advantageous characteristics, including easy installation, removal, and maintenance management, so that the fences can be built without heavy equipment, and with minimal environmental pollution. The fences are constructed using posts, wire ropes, wire nets, and energy absorbers, and possesses increased capacity in preventing rockfalls owing to the rational connection of their components. In addition, numerical simulations based on finite element methods (FEM) are also presented clearly and in detail and aim towards easy and convenient modeling in accordance to the programme's user manual (LS–DYNA, 2016). The dynamic characteristics of the protection fence are reproduced adequately by the consideration of nonlinear geometrical, constitutive laws, and the rational contact conditions of the numerical model.

(a) Vertical model (b) Horizontal model

Figure 3.1 Experimental models of protection fence against rockfalls

3.2 Vertically experimental models of protection fence

3.2.1 Experimental procedure

The structure of the fence consists of steel posts STK400, wire ropes, energy absorbers, and net, as shown in Figure 3.2. The posts are designed with diameters of 89 mm, and thicknesses of 3.2 mm, which are kept in position by wire ropes 3×7 G/O (the ropes is produced by J-WITEX Corporation with construction symbol 3×7 applied diameters of 12 mm, Galvanization G/O, and breaking load of 78.8 kN). Suspension ropes are strained between the posts, and within the span of the nets. Wire meshes (type Z–GS7) is designed by Japanese Industrial Standards, JIS G 3547, and made from galvanized iron wire with a diameter of 4 mm. The wire meshes are loosely connected in diamond configurations with dimensions of 50×50 mm^2. The weight used to emulate the rockfall as it impacted the fence was a reinforced-concrete (RC) block with a weight of 2 kN. In our case, it fell along an arc from a height of 25 m. In the conducted tests, the positions of application of the impact forces (A, B, C, and D) and the heights of the posts (2 m and 3 m) vary, as shown in Fig. 2. Particularly, the weight impacted the middle of the span at positions A and B, at a distance of 1 m away from the left span for position C, and at the post for position D. All collision heights were set at a distance of two-thirds of the height of the post.

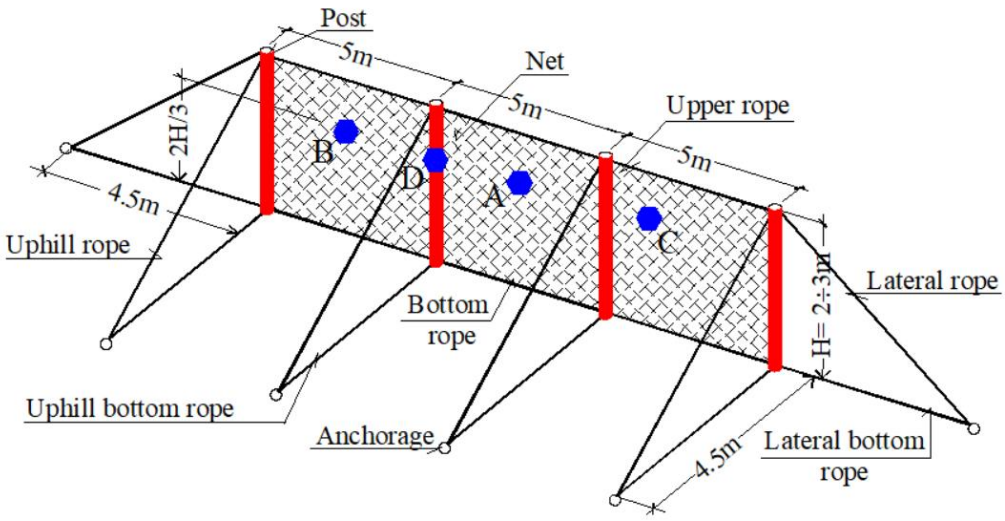

Figure 3.2 Structure of vertically models and impact positions

Figure 3.3 shows the positions of energy absorbers. Herein, there are two types of energy absorbers, including types M and F, which were made of metal blocks to join tightly the wire ropes by their bolts and nuts. In the case of the type-F absorber, wire ropes could slip in the same direction when the rope tension reached 10 kN, whereas the tension of 5 kN caused the slipping of the wire ropes in the opposite direction in the case of the type-M absorber. The wire

ropes installed in energy absorbers were provided with an extra length of at least 3 m so that the slipping could occur, the wire ropes always were restrained by the absorbers of types M or F. As a result, these flexible fence characteristics can dissipate effectively the impact energy of the rockfall. After the impact, the RC block was caught perfectly without the breakage of wire ropes or the wire net.

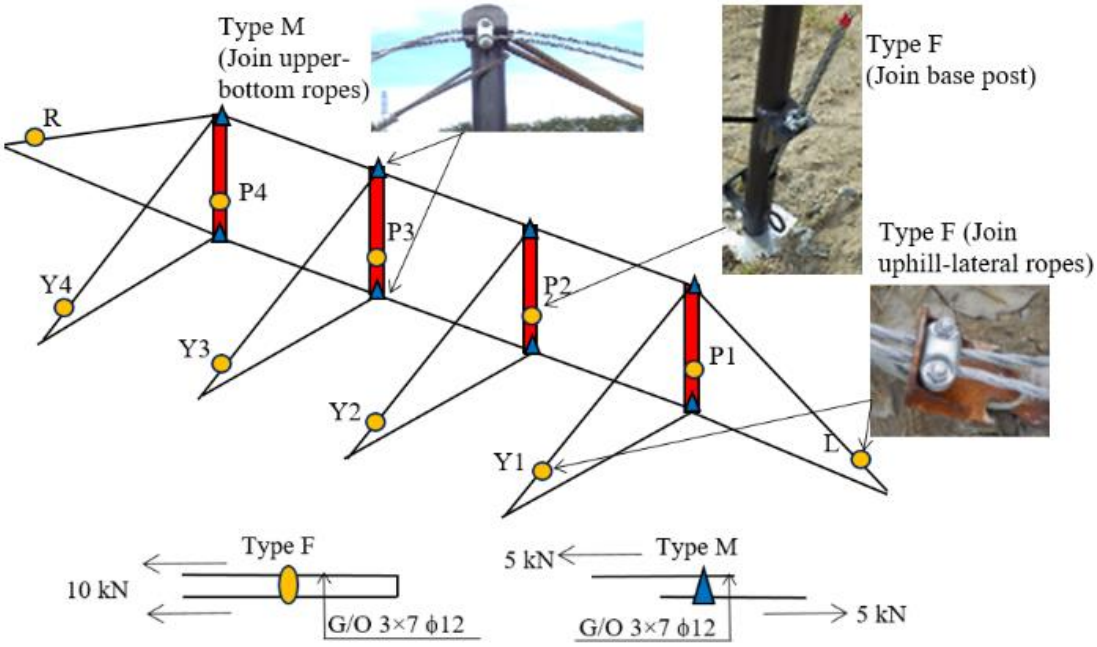

Figure 3.3 Positions of energy absorbers

In addition, the fence was placed on sand and various devices were installed to verify adequately the dynamic behaviors of the protection fence under impact. For instance, measurements were conventionally conducted acquired to locate the impact direction of the rockfall using the three-directional accelerometer, and the optoelectronic sensors were used to trigger the release of the RC block. The tension on the wire ropes was confirmed by strain gauges. A high-speed camera was placed in front of the fence to allow the characterization of the overall fence behavior and the estimation of deformation. After the impact, the slipping length of the wire rope was measured exactly with the use of energy absorbers.

Regarding the impact tests, two cranes were used in the experimental procedure, as shown in Figure 3.4. The first crane (500 kN) lifted its top to the center of the arc of the prescribed rock's motion, and the second crane (250 kN) pulled the RC block up to the specific height which was associated with the location of the corresponding impact (impact energy of 50 kJ). In order to execute the pendulum method, a proper arc was needed to ensure successful completion of the process by pulling using the second crane. When released by the first crane, the RC block fell along the arc like a pendulum, while the release by the second crane at the

movement direction of the RC block was along the horizontal direction such that the block impacted on the fence at defined positions (A, B, C, and D).

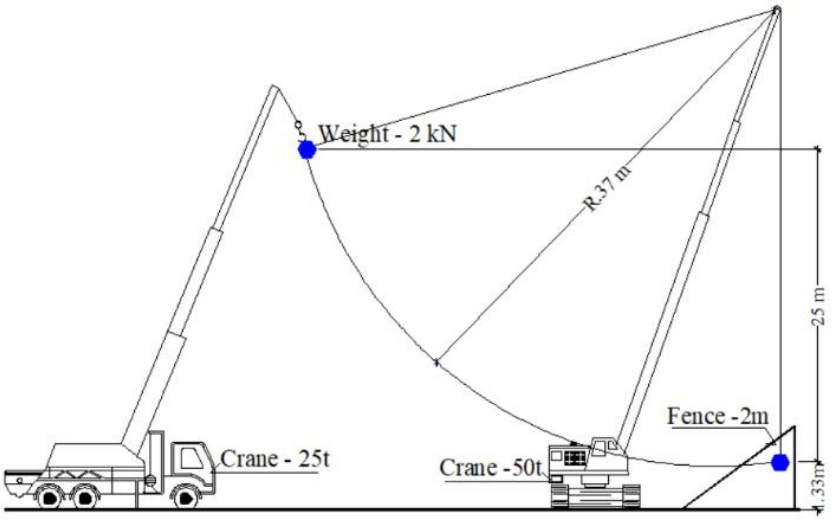

Figure 3.4 Pendulum method of experiment

3.2.2 Displacement and impact force outcomes

The main parameters are summarized in Table 3.1, and the photographs of the deformable states are illustrated in Figure 3.5. In all experimental cases, the protection fence with a span width of 5 m and post heights of 2 m and 3 m, could successfully absorb an energy impact of the order of 50 kJ. The maximum displacement of the fence at position C (case 1–3) was approximately 3.5 m, and this number guarantees the safety of the design of the protection fence because its structure is firmly established without breaks of wire nets or wire ropes after they absorb the impact energy. It is worth noting that when the RC block impacted directly the posts at position D (cases 1–4, 2–4), the deformation angle of the post at the height of 3 m tended to be larger that at 2 m. These angles were measured to be equal to 52 ° and 82 °, respectively. This means that the post at a higher height can perform worse regarding its deformation response under direct impact.

Table 3.1 Experimental results of vertically models

Case	Post (m)	Impact position	Rock mass (kN)	Falling height (m)	Impact energy (kJ)	Impact force (kN)	Maximum Displacement (m)	Residual height (m)	Remarks
1-1	2	A	2	25	50	29	3.3	0.9	Initial impact
1-2	2	B	2	25	50	27	2.8	0.9	Repeated impact
1-3	2	C	2	25	50	20	3.5	0.7	Repeated impact
1-4	2	D	2	25	50	24	52^0	1.2	Repeated impact
2-1	3	A	2	25	50	-	3.4	1.9	Initial impact
2-2	3	B	2	25	50	-	3.1	0.7	Repeated impact
2-3	3	C	2	25	50	-	-	-	Repeated impact
2-4	3	D	2	25	50	-	82^0	1.2	Repeated impact

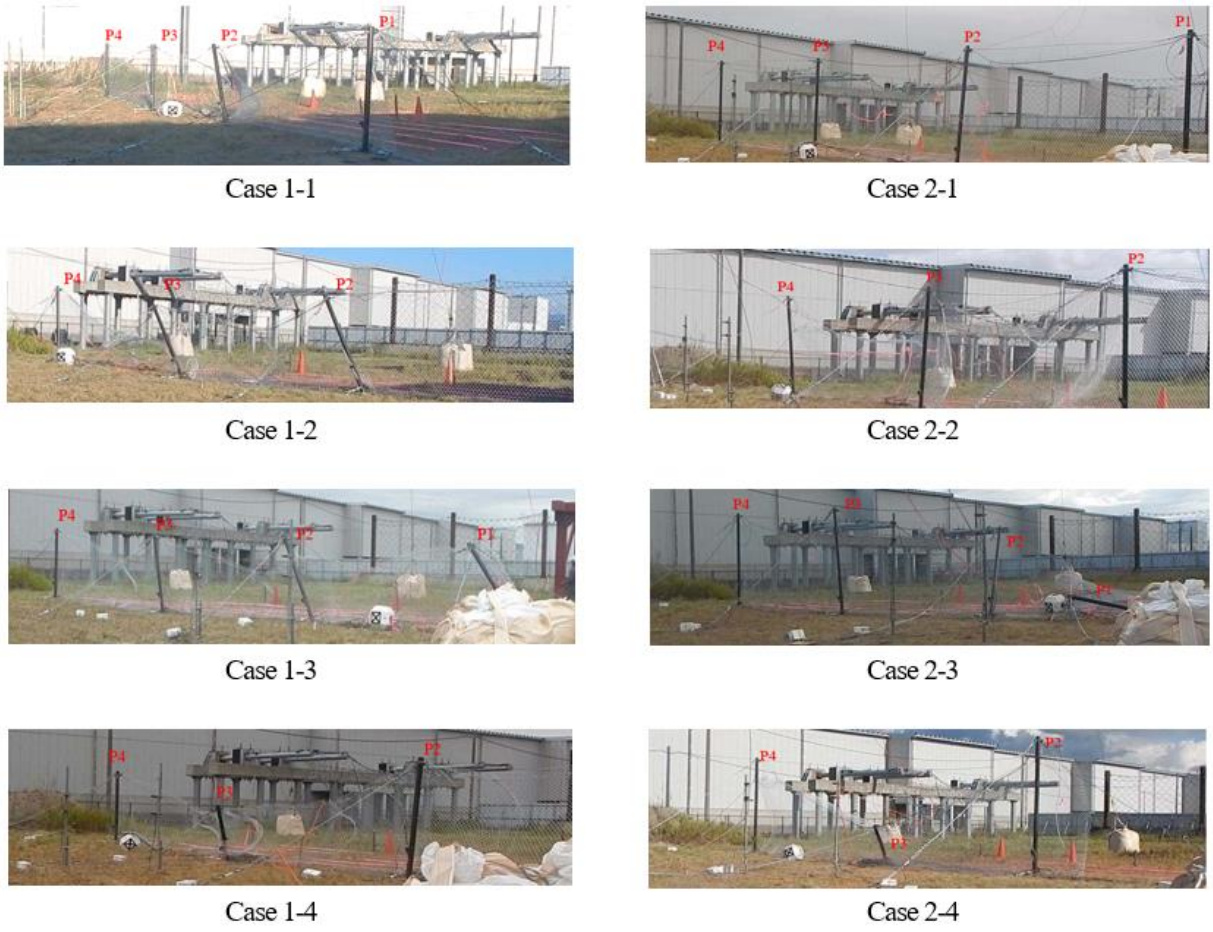

Figure 3.5 Deformation situations of vertically models

Regarding the residual height of the fence, it exhibited a downward trend compared to the initial impact in cases 1–1 and 2–1, and the repeated impacts in cases 1–2, 1–3, and 2–2. This phenomenon was applicable to the elongation of the wire net, wire ropes, and the movement of anchorages. In addition, the change of the post's height was also surveyed to evaluate the effectiveness of experimental models after impact. When this change is compared in cases 1–1 (from 1970 mm to 910 mm) and 2–1 (from 3000 mm to 1890 mm), which involved only the initial impact, the rate of decrease in the height of the fence was approximately 50 % in case 1–1, and approximately 40 % in case 2–1. As expected, the protection fence with a post of 3 m could respond more effectively when the collision occurred at the middle of the span. It can be thought that the residual heights of the fence depend on the change of the post's height; the post at a higher height can perform a smaller residual height.

The relations of impact force, displacement, and absorbed energy are illustrated in Figure 3.6. Herein, there are unfortunately no fence data available at a height of 3 m owing to the failure of measurements. The values of the impact force are calculated by the multiplication of the obtained acceleration with the mass of rock. Regarding the relationship between the

absorbed energy and displacement in cases 1–1 and 1–4, there is a rapid growth of absorbed energy up to the point at which the maximum displacement was reached.

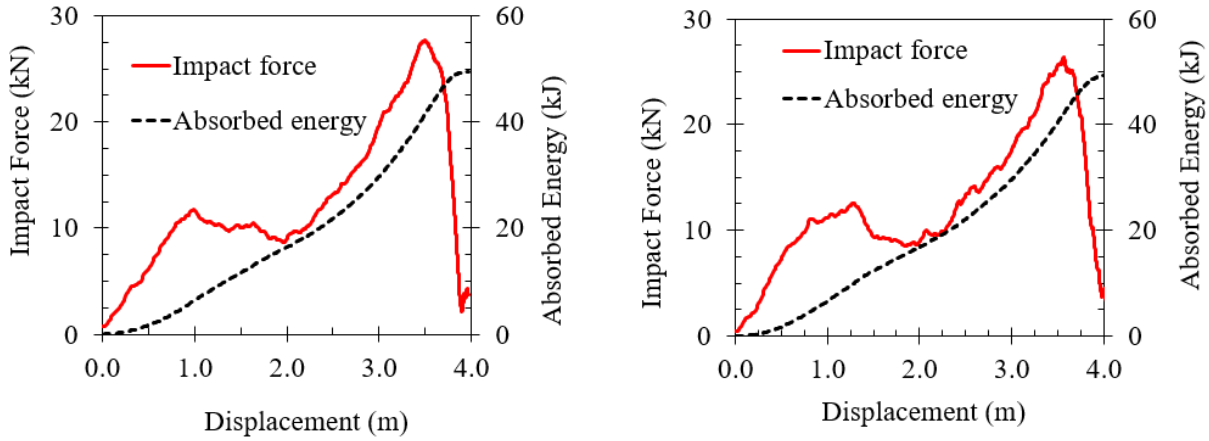

(a) Case 1-1 (b) Case 1-4

Figure 3.6 Relations of impact force, displacement and absorbed energy

3.2.3 Rope tension

The positions of wire ropes and the time history of rope tension are shown in Figures 3.7 and 3.8, respectively, and the maximum values of the rope tensions are summarized in Table 3.2. Based on the results of all experimental cases in Table 3.2, the lateral rope (L6) possesses the greatest tension, which is approximately 13.99 kN in case 2–2, while the maximum tension of an uphill rope (L3) is 10.45 kN in case 1–1. It can be said that the rope tension reaches its maximum values when the impact occurs at the middle point of the span, at positions A and B. In addition, the rope tension tends to increase significantly compared to the rope tension for the fences that consisted of posts with heights of 2 m and 3 m because the protection fence is set up with higher posts, and the height of the impact point was correspondingly set at a higher location.

The comparison of the rope tensions of cases 1–1 and 2–1 involved impacts at the center span, as shown in Figures 3.8(a) and 3.8(b), respectively, and indicated that the rope tension exhibited nearly the same fluctuation. Additionally, the use of a short time span to increase the maximum tension also yielded the same fluctuation at approximately 0.2 s. Moreover, the increase of the rope tension of the lateral and uphill ropes (L1÷L6) was more abrupt compared to that of the bottom lateral and bottom uphill ropes (L7÷L12). Accordingly, the bottom ropes were unnecessary for the installation of energy absorbers of type F, whereas absorber installations at the lateral and uphill ropes became effective in order to limit their tensions.

When the RC block impacted directly the post in cases 1–4 and 2–4, as shown in Table 3.2, the rope tension reached the maximum values only in ropes L4 and L10 because these ropes

linked directly to the post. In addition, the initial impacts of cases 1–1 and 2–1, and the repeated impacts of cases 1–2, 1–3, 1–4, 2–2, 2–3, and 2–4, were assessed, and the outcomes are listed in Table 3.2. Elicited outcomes indicate a trend of rapid decrease in the rope tension for the cases of repeated impact. This phenomenon was caused by the elongation of the wire ropes and the movement of anchorages. Anchorages were reinforced on sand background in order to hold uphill and bottom ropes in experimental models. The boundary condition is not rigid, so the anchorages occurred the small-scale movement under repeated impact.

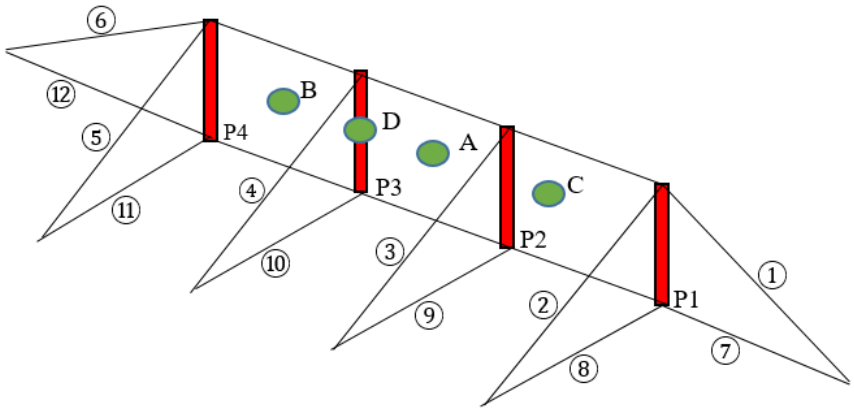

Figure 3.7 Location of each wire rope

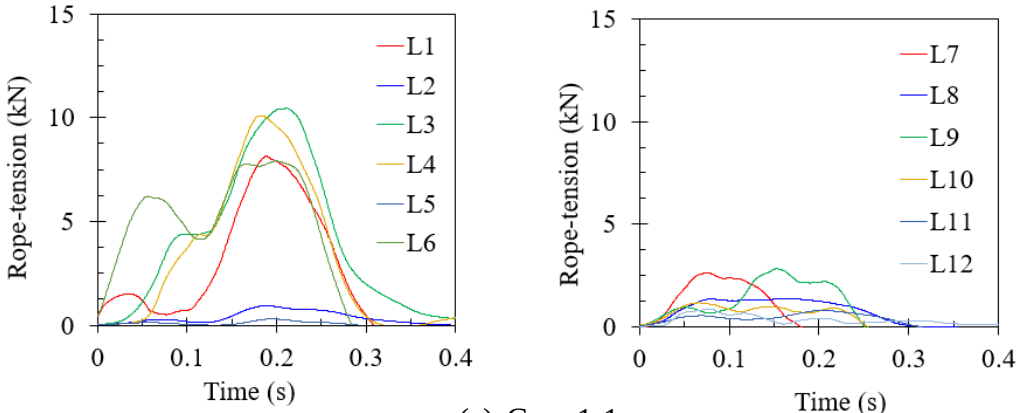

(a) Case 1-1

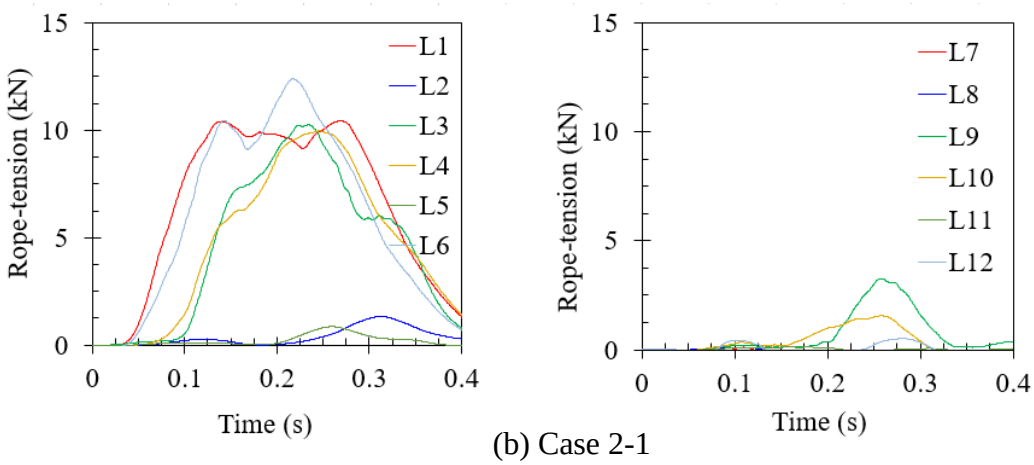

(b) Case 2-1

Figure 3.8 Time curve of rope tension

Table 3.2 The maximum tension of wire ropes

Ropes	Case 1-1	Case 1-2	Case 1-3	Case 1-4	Case 2-1	Case 2-2	Case 2-3	Case 2-4
L1	8.14	5.28	5.87	4.65	10.44	8.14	6.69	4.18
L2	0.93	0.77	7.68	0.08	1.33	0.12	5.87	-
L3	10.45	1.14	8.94	1.82	10.25	1.37	4.79	3.09
L4	10.10	6.94	0.76	11.19	9.98	11.20	2.87	6.89
L5	0.30	9.26	0.13	2.24	0.86	11.50	0.33	5.06
L6	7.92	7.82	4.40	3.59	12.39	13.99	7.10	4.70
L7	2.61	0.12	3.30	0.07	0.12	0.00	2.04	2.13
L8	1.38	0.42	1.79	0.76	0.12	1.26	0.71	-
L9	2.83	0.19	3.67	0.66	3.26	0.51	7.53	0.31
L10	1.17	5.28	0.14	12.11	1.56	2.34	0.42	7.36
L11	0.79	0.91	0.02	0.29	0.13	0.59	0.10	0.00
L12	0.87	1.79	0.00	0.07	0.52	3.02	0.04	1.07

3.2.4 Energy absorbers

Table 3.3 The slipping length of wire ropes (mm) and the energy absorption of types M and F

Measured Position	Case 1-1		Case 1-2		Case 1-3		Case 1-4		Case 2-1		Case 2-2		Case 2-3		Case 2-4		Remarks (*)
	Left	Righ	Left	Right	Left	Right	Lef	Righ	Left	Right	Left	Righ	Left	Righ	Left	Righ	
Upper P1	0	980	0	0	0	0	0	0	210	0	0	0	0	0	0	0	Type M
Bottom P1	0	20	0	0	0	0	0	0	0	20	0	0	0	0	0	0	Type M
Upper P2	0	25	345	1140	1180	660	0	0	10	0	375	180	520	0	0	30	Type M
Bottom P2	0	0	70	70	1260	35	0	0	10	900	350	0	116	3	28	0	Type M
Upper P3	650	0	0	0	0	0	0	0	900	0	0	20	60	80	1260	0	Type M
Bottom P3	1215	0	1060	0	720	10	39	0	0	0	630	10	740	10	320	35	Type M
Upper P4	0	0	0	0	0	0	0	0	200	0	0	159	0	0	270	0	Type M
Bottom P4	0	0	0	0	0	0	0	0	0	50	155	0	140	0	740	0	Type M
Base P1	0	0	0	0	0	0	0	0	0	0	0	0	0	0	0	0	Type F
Base P2	15	0	0	0	0	0	0	0	0	0	0	0	15	0	0	0	Type F
Base P3	0	0	25	0	0	0	30	0	0	0	0	0	0	0	0	0	Type F
Base P4	0	0	0	0	0	0	0	0	0	0	0	0	0	0	0	0	Type F
Y1	0	0	0	0	0	0	0	0	0	0	0	0	0	0	0	0	Type F
Y2	0	0	0	0	0	0	0	0	200	0	0	0	0	0	0	0	Type F
Y3	0	0	0	0	0	0	0	0	0	0	0	0	0	0	0	0	Type F
Y4	0	0	0	0	0	0	0	0	0	0	0	0	0	0	0	0	Type F
L	0	0	0	0	1020	0	0	0	0	0	0	0	0	0	0	0	Type F
R	0	0	0	0	0	0	0	0	20	0	0	0	0	0	0	0	Type F
Type M (**)	2890		2685		3865		390		2300		3310		2781		2683		
Type F (**)	15		25		1020		30		220		0		15		0		
Absorbed energy	14.60 kJ		13.68 kJ		29.53 kJ		2.25 kJ		13.70 kJ		16.55 kJ		13.74 kJ		13.42 kJ		

* The slipping length of wire ropes is measured at the positions of Types M or F.
** Total slipping length of wire ropes through Types M and F.

The installation of absorbers of types M and F are illustrated in Figure 3.3, and the slipping length of the wire ropes and energy absorption are listed in Table 3.3. The value of the energy absorption for these devices can be calculated by the multiplication of the total slipping length with the tensions of 5 kN and 10 kN, respectively. It can be observed from the results in Table

3 that the slipping of the wire ropes through the energy absorbers of type F did not occur in many experimental cases because this phenomenon only involved the positions of energy absorbers next to the impact area.

When the total slipping lengths were compared for the type M absorber for their initial and repeated impacts, the length significantly increased. For instance, the initial impacts associated with cases of 1–1 and 2–1 elicited slipping lengths of the order of 2.89 m and 2.30 m, respectively, whereas the wire ropes slipped by 3.86 m and 2.78 m in the repeated impact cases of 1–3 and 2–3, respectively. This situation could be attributed to the fact that the bolts and nuts of the metal block can be worn out by friction caused by the tension of the upper and bottom ropes when collisions occurred repeatedly. Therefore, it is recommended that the energy absorbers need to be replaced in the experimental cases in terms of repeated impacts.

Regarding the initial impact, the fence with 2 m posts in case 1–1 absorbed 14.60 kJ with type-M and F absorbers, while 13.70 kJ was absorbed by the fence with 3 m posts in case 2–1. It can be inferred that the energy absorptions of the M and F-type absorbers were not significantly different when the post height changed from 2 m to 3 m. Moreover, the smallest value of 2.25 kJ was absorbed in case 1–4 in which the RC block impacted directly the post. It can be considered that the impact energy was absorbed by these devices (types M and F), but also by the deformed post.

3.3 Horizontally experimental models of protection fence

3.3.1 Experimental cases

Table 3.4 shows the experimental cases, herein there are nine cases designed distinctly about impact positions, length of spans and applied load. The series of experiment were conducted for five impact positions A, B, C, D and E as shown in Figure 3.9. The distance of all collision points was set at 1 m far from the base; except for position A. The distance was 1.3 m far from the base of post. The spans 1, 2 and 3 were designed with a lengths of 5 m or 5.5 m, which depends on the impact position. The weight used the rockfall impacted the fence which was a reinforced-concrete (RC) block with a weight of 3400 kg. Drop height was 32 m corresponding to the collision velocity 25 m/s. The collision was a single impact for positions A and C. The collision at other positions B, D and E was repeated.

Table 3.4 List of experimental cases

Case	Impact Positions	Spans 1& 3 [m]	Span 2 [m]	Weight of rockfall [kg]	Drop height [m]	Applied load
1	A	5.0	5.5	340	32	Single impact
2	B	5.0	5.5	340	32	Repeated impact
3	C	5.0	5.5	340	32	Single impact
4	D	5.0	5.5	340	32	Repeated impact
5	C	5.0	5.0	340	32	Single impact
6	D	5.0	5.0	340	32	Repeated impact
7	E	5.0	5.0	340	32	Repeated impact
8	C	5.5	5.5	340	32	Single impact
9	D	5.5	5.5	340	32	Repeated impact

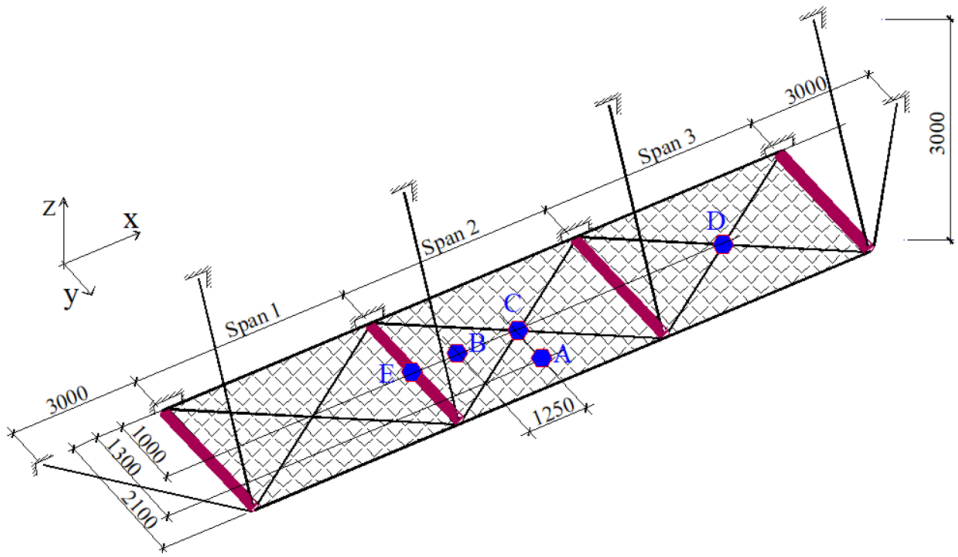

Figure 3.9 Impact positions in horizontal experiment

3.3.2 The structure of horizontal protection fence

Figure 3.10 shows the structural components of the fence. The structure of the fence consists of steel posts, wire ropes, wire mesh, suspension ropes, energy absorbers, and anchorages etc. Steel post is STK400 with diameters of 114.3 mm and thicknesses of 4.5 mm, which are kept in position by wire ropes 3×7 G/O (the ropes is produced by J-WITEX corporation with construction symbol 3×7 applied diameters of 12 mm, Galvanization G/O, and breaking load of 78.8 kN). Suspension ropes are tensioned between the posts, and within the span of the nets. Wire meshes (type Z–GS7) are designed by Japanese Industrial Standards JIS G 3547, and made from galvanized iron wire with a diameter of 4 mm. The shape of meshes is similar the diamond chain link net, the wire meshes are loosely connected in diamond configurations with dimensions of 50×50 mm^2.

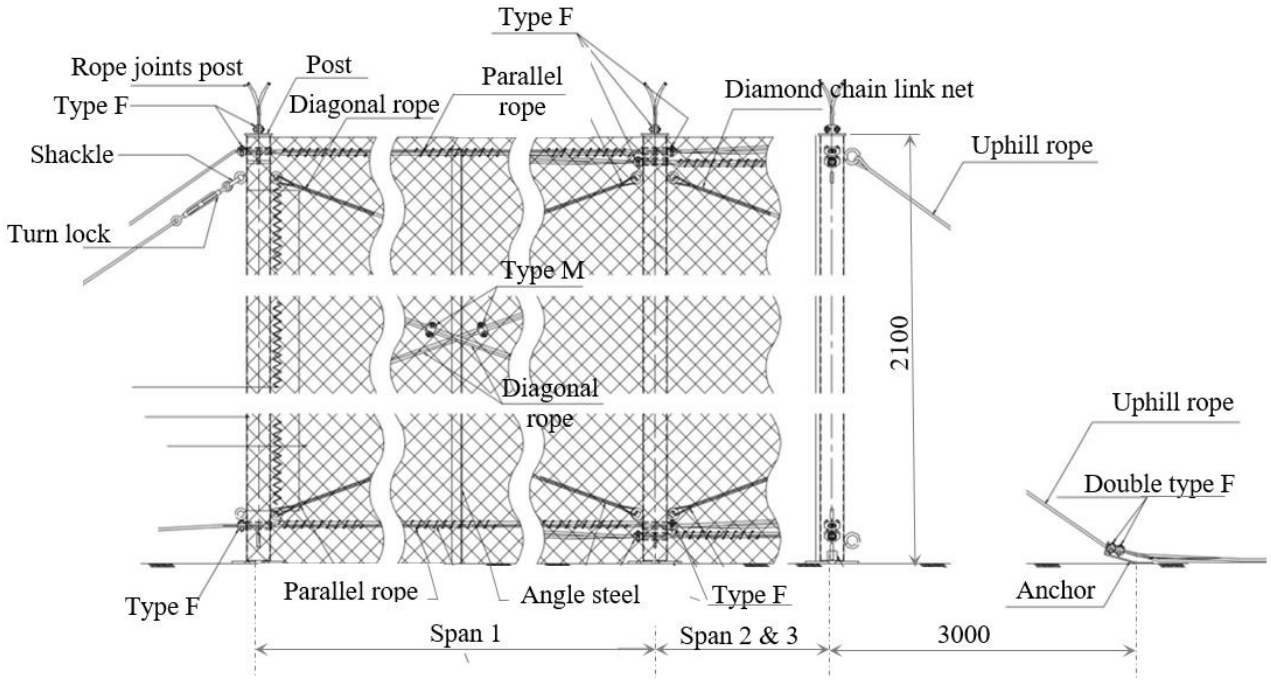

Figure 3.10 Structural components

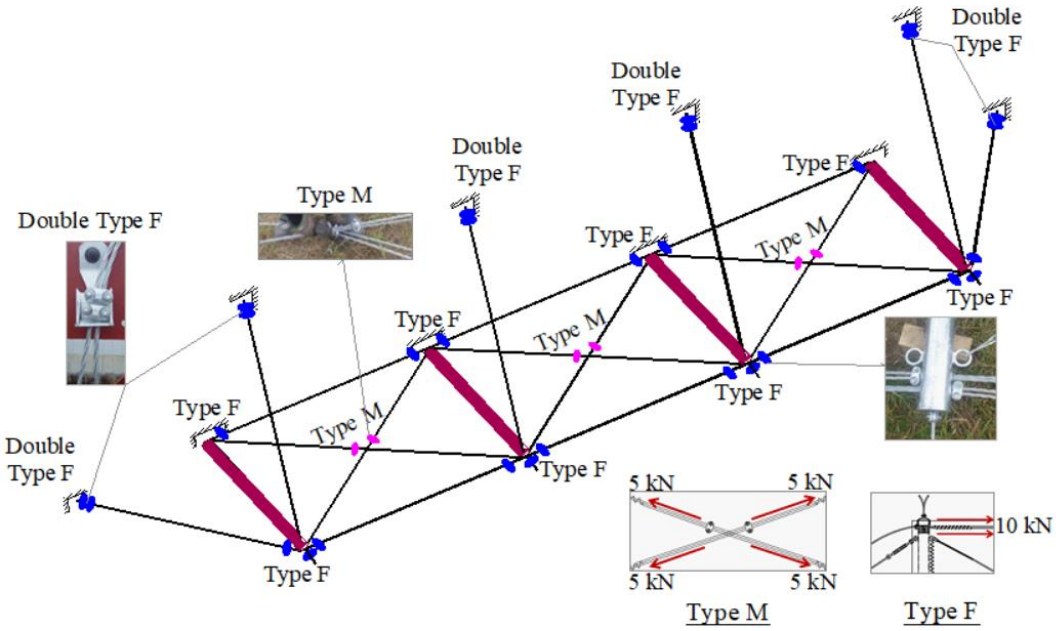

Figure 3.11 Positions of energy absorbers

Figure 3.11 shows the positions of energy absorbers. Herein, there are two types of energy absorbers, Type M and Type F. They were made of metal blocks to join tightly the wire ropes by their bolts and nuts. In the case of the Type F absorber, wire ropes can slip in the same direction when the rope tension force reaches 10 kN at the positions joined the head and base of posts. In the case of Type M absorber, wire ropes can slip in the opposite direction when the tension force of 5 kN, because diagonal ropes are joined together. In addition, double absorbers of Type F were used to join between wire rope and the anchorages, so the tension was 20 kN. The wire ropes installed in energy absorbers were provided with an extra length of at least 3 m

so that the slipping could occur, the wire ropes always were restrained by the absorbers of type M or type F. As a result, these flexible fence characteristics can dissipate effectively the impact energy of the rockfall.

There were three static test of energy dissipators, including type M, type F, and double Type F before they were used in these experiment. Energy dissipators are made of metal blocks to semi-fastened the wire ropes by their bolts and nuts. When pulled with the tensions 5, 10, and 20 kN, the ropes can slip through type M, type F, and double type F absorbers respectively. It is fairly reasonable to simplify the working load of energy dissipators to constant load because the wire rope dose not slip from these devices until the magnitude of the friction force exceeds a allowed value, which can be controlled by tightening the bolts.

3.3.3 Procedure of experiment

The fence was placed horizontally on the steel frame and various devices were installed to verify adequately the dynamic behaviors of the protection fence under impact. Measurements were conventionally conducted acquired to locate the impact direction of RC block as a rockfall using the three-directional accelerometer, and the optoelectronic sensors were used to trigger the release of the RC block. The tension on the wire ropes was confirmed by strain gauges. A steel plate was inserted to the tensile wires towards the uphill anchors, and the side anchors as well. A high-speed camera was placed in front of the fence to allow the characterization of the overall fence behavior and the estimation of deformation.

A crane was used in the experiment. The crane (capacity 500 kN) pulled the RC block up to the specific height which was associated with the location of the corresponding impact (impact energy of 106 kJ). When RC block was released, the block impacted on the fence at defined positions (A, B, C, D and E) with the corresponding velocity of 25 m/s. During the impact, the deformations of meshes, wire ropes, posts, etc. were observed visually. The slipping lengths of the wire rope through energy absorbers were measured exactly.

This horizontal model was carried out with the nine cases of impact tests. These cases divided in four cases 1, 3, 5 and 8 by single impact and five cases 2, 4, 6, 7 and 9 by repeated impact. The validity of the experimental data involves in the out-of-plane displacement, impact force, absorbed energy and rope tensions.

3.3.4 Deformation results

Table 3.5 List of main results of horizontal models

Case	Absorbed energy of Type M and Type F [kJ]	Maximum rope tension [kN]	Maximum displacement [m]	Residual height [m]	Remarks
1	71	32	3.4	1.73	RC block was caught perfectly
2	68	33	3.5	-	RC block was caught perfectly
3	60	36	3.7	1.55	RC block was caught perfectly
4	65	33	3.6	1.60	RC block was caught perfectly
5	59	34	-	-	The wire mesh was damaged
6	71	39	3.8	-	RC block rebounded and fell out the fence
7	-	38	-	-	The wire mesh was damaged after the block hit directly the post
8	76	35	3.7	1.40	RC block was caught perfectly
9	66	38	3.6	1.60	RC block was caught perfectly

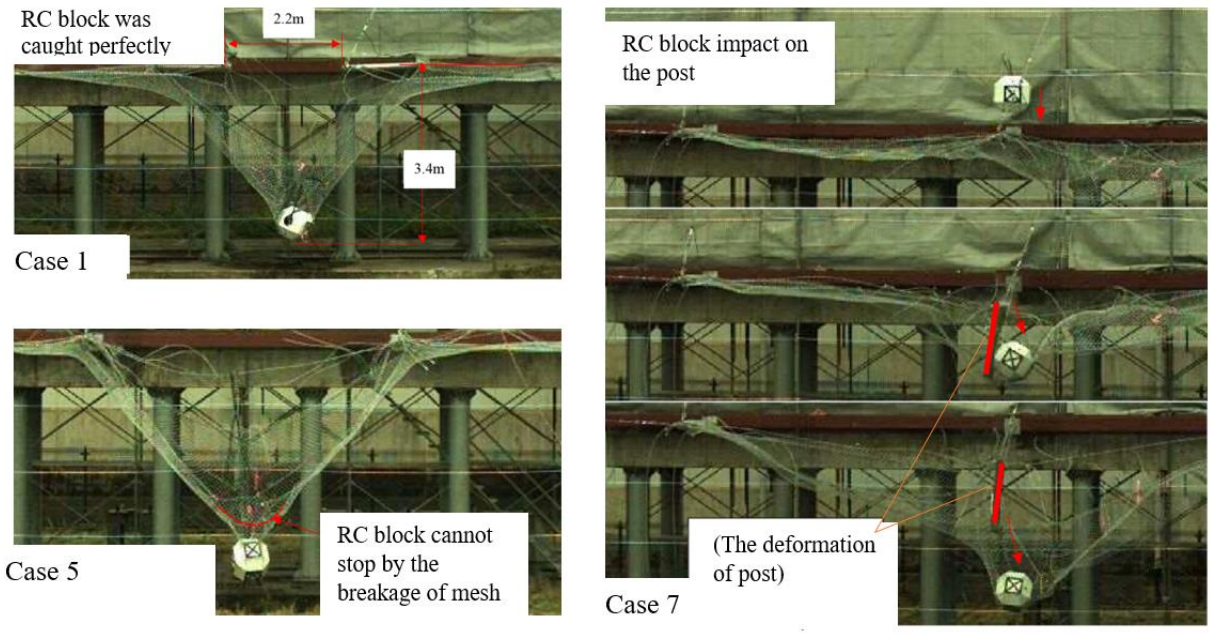

Figure 3.12 Situations of deformable of horizontal fence in experiment

The main parameters are summarized in Table 3.5, and the photographs of the situations of deformation are illustrated in Figure 3.12. In many cases 1, 2, 3, 4, 8 and 9, the protection fence with post heights of 2 m and a span width of 5 m and 5.5 m could successfully absorb an impact energy of 106 kJ. The maximum displacements of the fence were approximately from 3.4 m to 3.7 m, which can guarantees the safety of the design of the protection fence because its structure is firmly established without breaks of wire nets or wire ropes after they absorb the impact energy. In addition, the maximum displacement measures nearly equal at impact

position C for cases 3 and 8 in which the length of end spans was designed to be 5 m and 5.5 m, respectively. It can be thought that a change of the length of end spans 1 and 3 could not effect on the result of displacement.

On the other hand, a change of the length of middle span 2 could lead to an unexpected result. For example, span 2 decreased 10 % length of span (0.5 m) in cases 5, 6 and 7, these experimental models with length of mid-span of 5 m cannot catch RC block due to the breakage of wire mesh, the rebound of RC block or the deformation of post as shown in Figure 3.12. Regarding the residual height of the fence, it exhibited a downward trend compared to the single impact in cases 1, 8 and the repeated impacts in cases 4, 9. This phenomenon was applicable to the elongation of the wire net, wire ropes. In addition, the change of the height of fence was also surveyed to evaluate the effectiveness of experimental models after impact. When this change is 1.60 m for both case 4 and case 9, which involved only the repeated impact. As expected, the residual heights of the fence do not depend on the change of length of span when the collision occurred at the middle of end span.

3.3.5 Impact force and absorbed energy

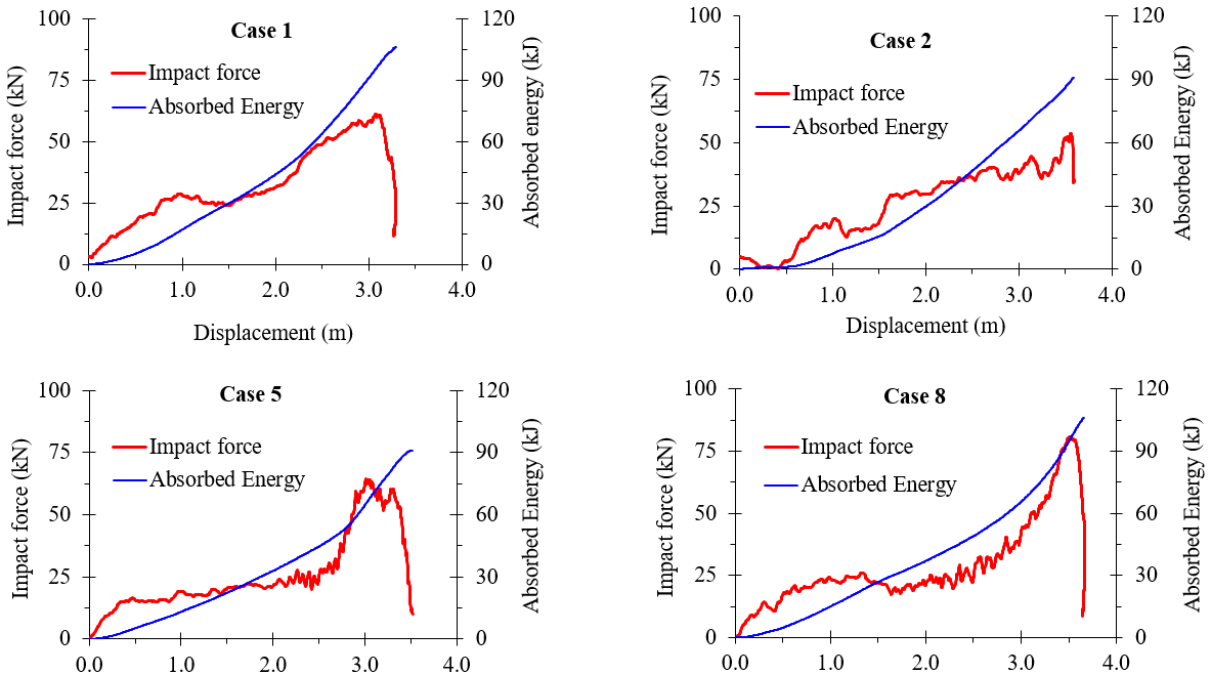

Figure 3.13 Relations of impact force, displacement and absorbed energy

The relations of impact force, displacement, and absorbed energy are illustrated in Figure 3.13. The values of the impact force are calculated by the multiplication of the obtained acceleration with the mass of rock. In cases 1 and 2, the experimental models were set up with the same length of spans, the maximum value of impact forces were no significant differences,

nearly 59.52 kN and 50.94 kN. However, the models were set up with the different lengths as case 5 (spans of 5 m) and case 8 (spans of 5.5 m), the impact forces were clearly distinguishing because their values peaked at 63.02 kN and 95.88 kN, respectively. It is said that the impact force of the fence with longer spans tends to be higher that of the fence with shorter spans. In addition, the maximum value of the total energy reached 106 kJ for cases 1 and 8, and there was a significant increase in the absorbed energy until it reached the maximum impact force.

Regarding energy absorbers, types M and F. Their installation is illustrated in Figure 3.11, and the value of the energy absorption for these devices are listed in Table 3.5. Their values can be calculated by the multiplication of the total slipping length of the wire ropes through types M, F and double F with the tensions of 5 kN, 10 kN, and 20 kN respectively. It can be observed that the slipping of the wire ropes through the energy absorbers of type F did not occur in many experimental cases because this phenomenon only involved the positions of energy absorbers next to the impact area. Based on the results of all experimental cases in Table 3.5, the value of the devices ranges from 59 kJ to 76 kJ, so they can dissipate effectively from 56 % to 71 % the total impact energy of the rockfall (106 kJ).

3.3.6 Rope tensions

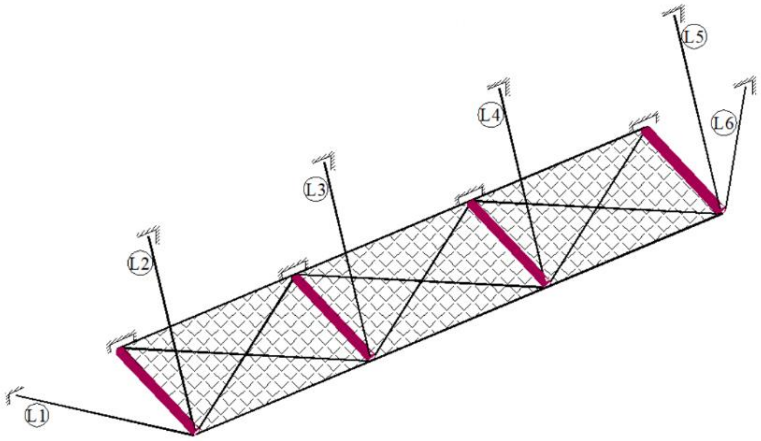

Figure 3.14 Locations of each rope

The positions of wire ropes and the time history of rope tension are shown in Figures 3.14 and 3.15, respectively. The lateral rope (L6) possesses the greatest tension, which is approximately 39.42 kN in case 06, while the maximum tension of an uphill rope (L4) is 32.90 kN in case 01. It can be thought that the rope tension reaches its maximum values when the impact occurs at the middle point of the span, at positions A and D. In addition, the rope tension tends to decrease compared to the rope tension for the fences that consisted of spans with lengths of 5.5 m (case 8) and 5 m (case 5) because when the comparison of the rope tensions of these cases involves single impacts at the center span. There is only one rope L3 exceeded 20 kN in case 8; whereas there are many ropes L1, L3, L4 and L6 reached over 20 kN in case 5.

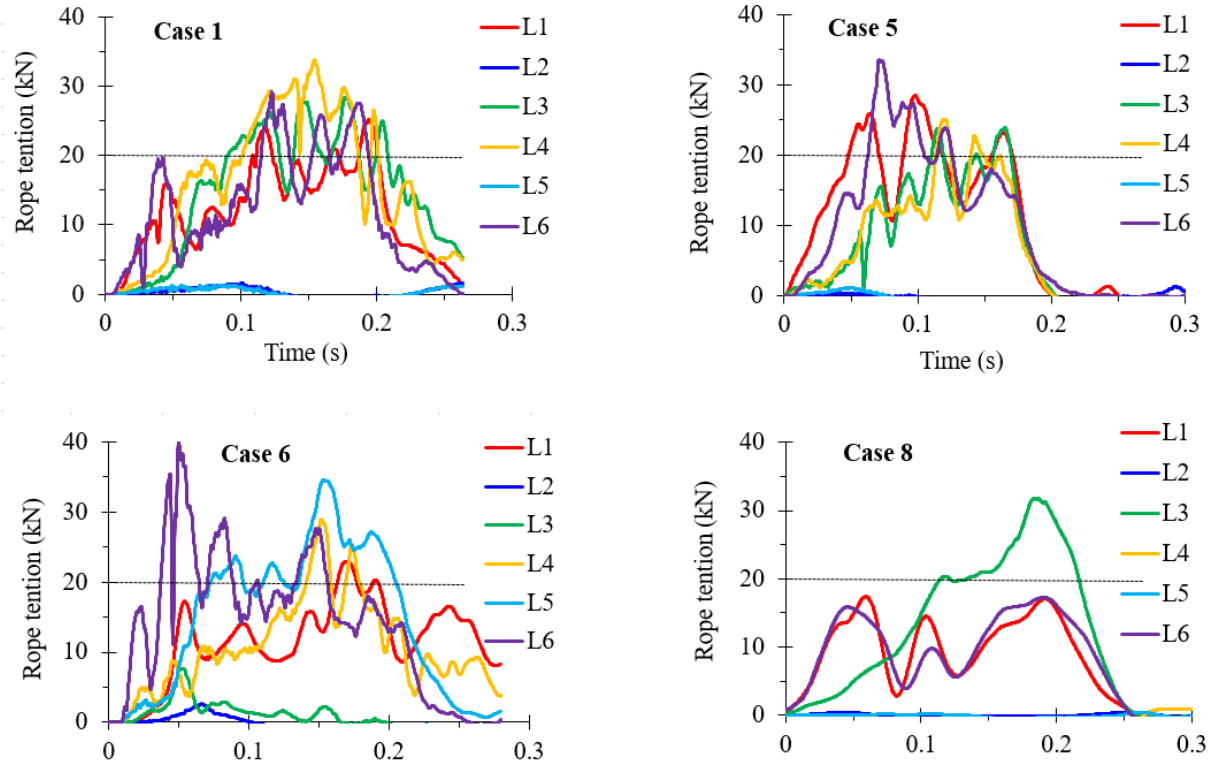

Figure 3.15 Time curve of rope tension

3.4 Numerical modelling of the fences

The model of the numerical simulation is illustrated in Figure 3.16, whereby the fence was built along the vertical direction and the impact of the RC block was in the horizontal direction. For purposes of numerical simulation, the simplest possible assumptions in terms of the choice of finite elements, constitutive laws, contact conditions, etc., are presented clearly and are detailed in order to reproduce adequately the dynamic behavior of the protection fence. Moreover, this numerical model can be useful not only for someone who is interested in modeling the protective structures using the LS–DYNA, but also for the addition or replacement of full-scale tests which normally require large budgets, and sometimes elicit poor results.

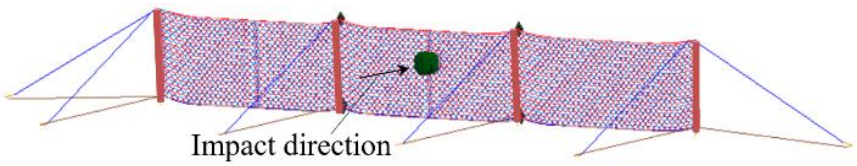

Figure 3.16 Protection fence built in LS-Dyna

3.4.1 Used assumptions for simulation

Table 3.6 Material properties

Structural component	Type	Yield stress (MPa)	Density (kg m^{-3})	Young's modulus (GPa)	Poisson's ratio
Wire net	Z-GS7	250	7850	200	0.3
Wire rope	3×7 G/O	750	7850	139	0.3
Post	STK400	235	7850	200	1.82
Rock	Concrete	-	2300	30	0.167

Firstly, the choice of finite element and material models involved the use of wire nets with dimension of 50 × 50 mm^2, and ϕ 4.0. There are different studies in terms of the simulation of such a net, including the Belytschko–Tsay shell elements and fabric material (MAT_034) that were adopted to model this wire net (Dhakal et al., 2011). A cable element and cable discrete material (MAT_071) were also used to simulate such wire net without the compressive force (Phuc et al., 2012). In this study, the elements of the wire net were modeled by truss elements that was built-in to LS–DYNA. This choice emulated the real behavior of the wire net under collision. When the rockfall impact occurred, failure strain was exerted on the wire net that may break it at the impact location. Therefore, truss elements were more suitable for such situations compared to others. The material properties of wire nets are shown in Table 3.6.

The numerical model of wire net aims to be as close as possible to experimental model, the net was modelled as a diamond meshwork of truss elements (diameters of 4 mm and lengths of 80 mm) with no flexural rigidity. The truss elements were arranged in a reasonable configuration like the real shape of the eyes-net. This means that each of the truss elements were connected together along the Z direction and created vertically separate chains, and then the chains were woven loosely along the X direction, as shown in Figure 3.17. After impact, the loose connections of the chains become tightly connected with each other, as shown in Figure 3.17. In order to implement such connections, the keyword of Contact_Automatic_General_Edgeonly (LSTC, 2016) was defined to model the contacts of the chains of truss elements, in which each chain cannot translate relative to another in any direction, their connectivity is free.

The wire ropes were modeled by the section of the cable elements. The nonlinear material model (MAT_071), Mat_Cable_Discrete_Beam, was calibrated with a constitutive law, as shown in Figure 3.18(a). The rate effect of the strain was not considered on the overall performance of the fence because of the low-speed of the rockfall impact, as compared to that of the blast or the projectile (Malvar and Crawford, 1998; Hua Jiang et al., 2012), and the slip

of the wire ropes through energy absorbers which were inserted on the wire ropes. The material properties of wire ropes are shown in Table 3.6.

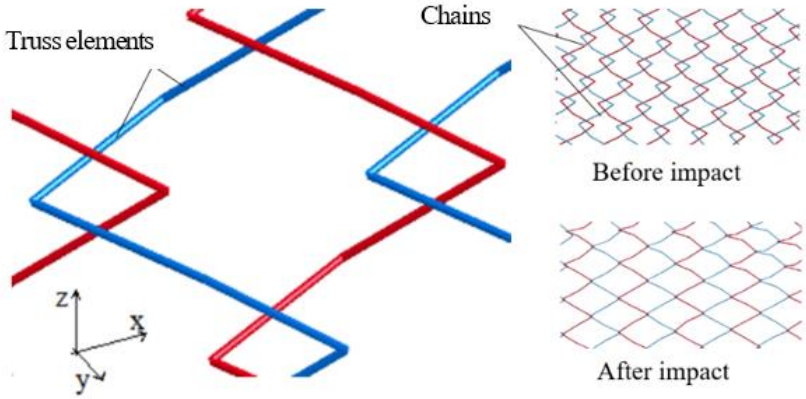

Figure 3.17 The configuration and deformation of wire net

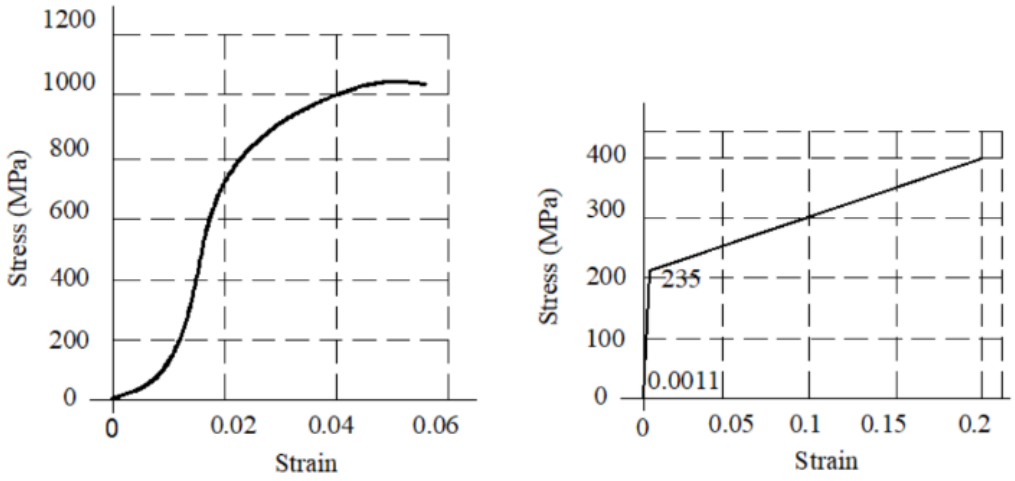

(a) Wire rope (b) Post

Figure 3.18 Stress-strain relation of wire rope and post

The posts were modeled by the beam elements and the constitutive law of the Platic_Kinematic material (MAT_003), as shown in Figure 3.18(b). Middle posts P2 and P3 were modelled with special devices at their heads and bases as shown in Figure 3.19, which can intercept the movement of the wire net when the impact occurred. The elicited behavior in accordance to the numerical analysis was similar to that elicited in the real experiment. However, in the case of the actual experiment, the wire net could move along the upper and bottom ropes, but it was prevented at the heads and bases of the middle posts. These interceptions were modeled by the Belytschoko–Tsay shell elements with MAT_003, and with the application of the keyword of Contact_Automatic_Nodes_To_Surface. This contact can prevent nodes when they move through a surface. Herein, these nodes were defined as the slave part; shell elements were the master part, and the coefficients of friction was set to 0.4.

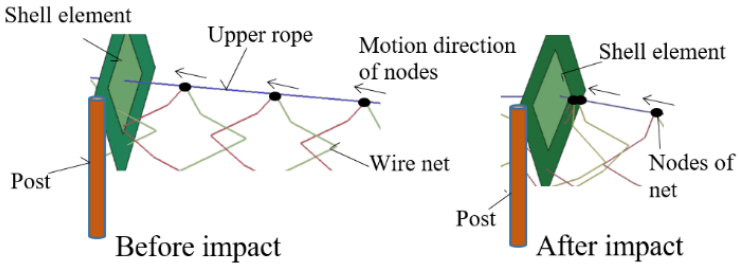

Figure 3.19 Shell element at the left head of post P2

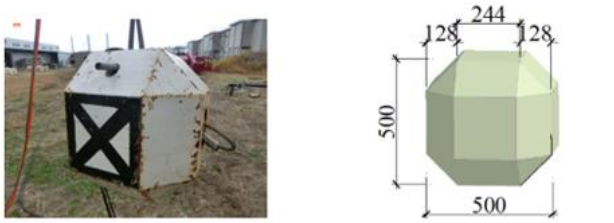

(a) RC block (b) Elastic-solid elements

Figure 3.20 The shape of rockfall

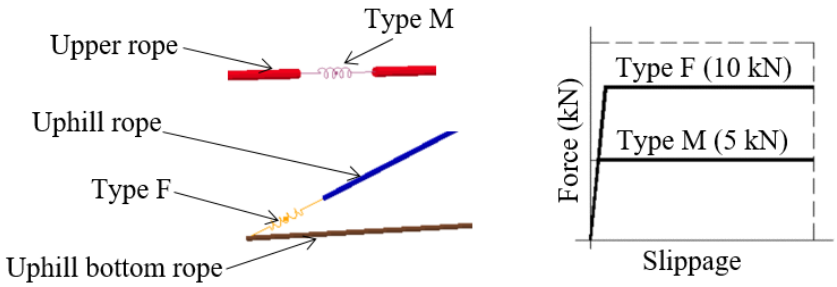

Figure 3.21 The energy absorbers

The block was made from a steel shell with a polygonal shape which was filled with concrete, as shown in Figure 3.20, according to the European technical approval guidelines (ETAG–027, 2008). The maximum height of the block was 0.5 m, and its mass was 0.2 ton, with an initial velocity of 22.15 m s^{-1} (kinetic energy of 50 kJ) at the impact locations. The block was modeled using solid elements, as shown in Fig. 13b, and was assigned to an elastic (MAT_001) material. The concrete properties used to mould the block in the experiment are shown in Table 4. The keyword of the contact algorithm Automatic_Beams_To_Surface, which was built-in to LS–DYNA, was adopted herein. This technique provided a way of treating the interactions between the block and net, respectively, as the master and slave parts. It is useful for impacting solid elements over beam elements, and for the coefficients of friction was set to the constant value of 0.4.

Finally, the energy absorbers were modeled in an equivalent manner using spring elements, and these elements could be compatible with the slippages of the type-M and type-F absorbers

shown in Figure 3.21. The selections of the section and material for the spring elements were also rational and sufficient to their characteristics, and the keywords of Section_Discrete and Spring_Elastoplastic (MAT_S03) were selected to reproduce the slipping behavior of these devices. This material provided an elastoplastic translational or rotational spring. Correspondingly, the values of the slipping forces of 5 kN and 10 kN were applied to the absorbers with types M and F, respectively. All anchorage nodes, including the hinged bases of energy absorbers connected to the ropes and posts, were restrained against translation in all directions.

3.4.2 Model conditions

The model of the movement of the nodes of the wire net along the wire rope was built without the fixed connection between the nodes of the wire net and the rope. Otherwise, every node of the wire net could move freely along the rope. This phenomenon corresponded mostly to the real shackles. The nodes of the wire net and the ropes were completely different, and they did not share any nodes. Therefore, the nodes of the wire net were designed close to the nodes of the rope. Additionally, at the initial position, the nodes of the wire net (1÷7) were not at the same place as the nodes of the rope denoted by I, II, III and IV, as shown in Figure 3.22. The nodes of the wire net were linked to the cables elements of the rope by the contact algorithm of Guided_Cable. This is one of the unique features of LS–DYNA because the nodes of the net can move freely along the cable elements when adopted by this contact condition. Herein, the coefficients of friction were set to 0.15. (Critina et al., 2012; Phuc et al., 2012). The value of 0.15 is applied to obstruct the slipping, resulted in the rational raise of rope tensions when comparing between experiment and simulation.

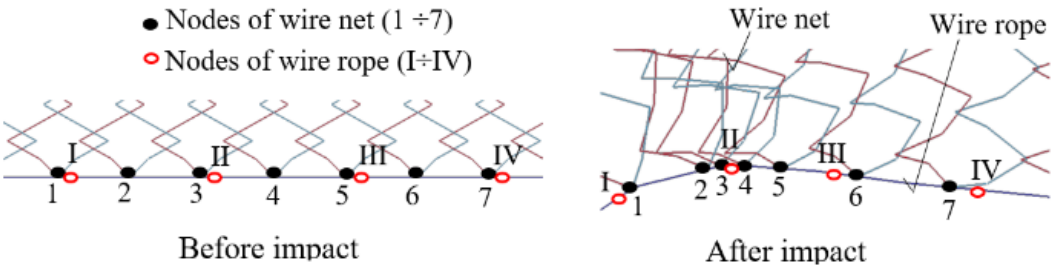

Figure 3.22 The movement of nodes

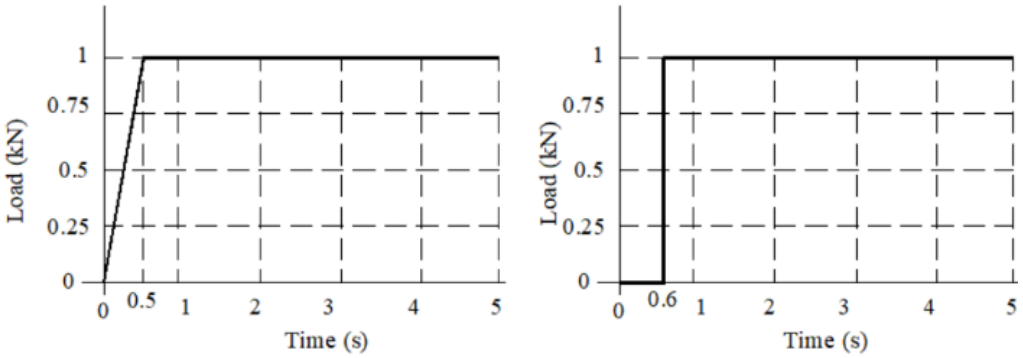

(a) Wire net, ropes and posts (b) RC block

Figure 3.23 The gravity load of components.

Conversely, the protection fence was loaded by its dead load and the impact force of the rock. Firstly, the gravity of the fence was gradually increased until its quasistatic equilibrium was reached. Subsequently, the rock moved and hit the wire net. The load of the components included the wire net, rope, etc., as illustrated in Figure 3.23(a), except for the rock. The load increased gradually to avoid numerical instability and numerical noise. The load was introduced by the use of the command lines *Load_Body_Parts, *Load_Body, and *Define_Curve. As usual, the first few seconds, from 0 s to 0.5 s, were set up to the initial sag of the protection fence. The earth pressure was then set up to vary continually as a function of time (0.5 s ÷ 5 s).

In fact, the gravity and the earth load are both applied in the same vertical direction, as shown in Figure 3.16. In this figure, the structure is placed vertically but with the movement of the rock is in the horizontal direction. Therefore, the dead load of the rock was set up at the same time when the rock was released at approximately 0.6 s, and easily hit the wire net at the impact position at two-thirds of the height of the fence. The command line *Load_Gravity_Part and *Define_Curve in Figure 3.23(b) was adopted to define the dead load of the rock.

In addition, the velocity of the rock of 22.20 ms^{-1} corresponds to a falling height of 25 m, or to an impact energy that is equal to approximately 50 kJ. In numerical analyses, the rock was placed next to the wire net with the aim of reducing the execution time, and the motion of the rock was modelled using the keyword *Boundary_Prescribed_Motion_Set. All nodes of the rock were set in motion from the birth of the command line at 0.60 s to the death of the command line at 0.63 s at a speed of 22.20 ms^{-1}. After a period of 0.62 s, these nodes were not anymore subject to the boundary kinematic conditions and their movement followed the physical laws.

Another condition, hourglass control (*Hourglass) was defined in stiffness form (IHQ = 4) to prevent zero energy deformations for the quadrilateral shell and hexahedral solid elements. This keyword could be used to redefine the default values of the hourglass control type and coefficient. In order to reduce the number of elements for the sake of reducing the analysis time consumed by the software, the wire-net was simulated with one layer which comprised a 150 ×

150 mm square grid. In fact, the analyzed results of the impact force, displacement, kinetic energy, etc., were not noticeable different when surveyed for grid sizes of 50 and 150 mm. This model consisted of 11,227 nodes and 16,863 elements in total, with 15,878 beams, 24 discrete, 20 shells, and 941 solids. Finally, the explicit analysis was carried out to simulate the dynamic and nonlinear responses of the protection fence for an impact energy of 50 kJ. The average computation time of the model using an ordinary PC was approximately two hours.

3.4.3 Displacement, impact force, and rope tension results

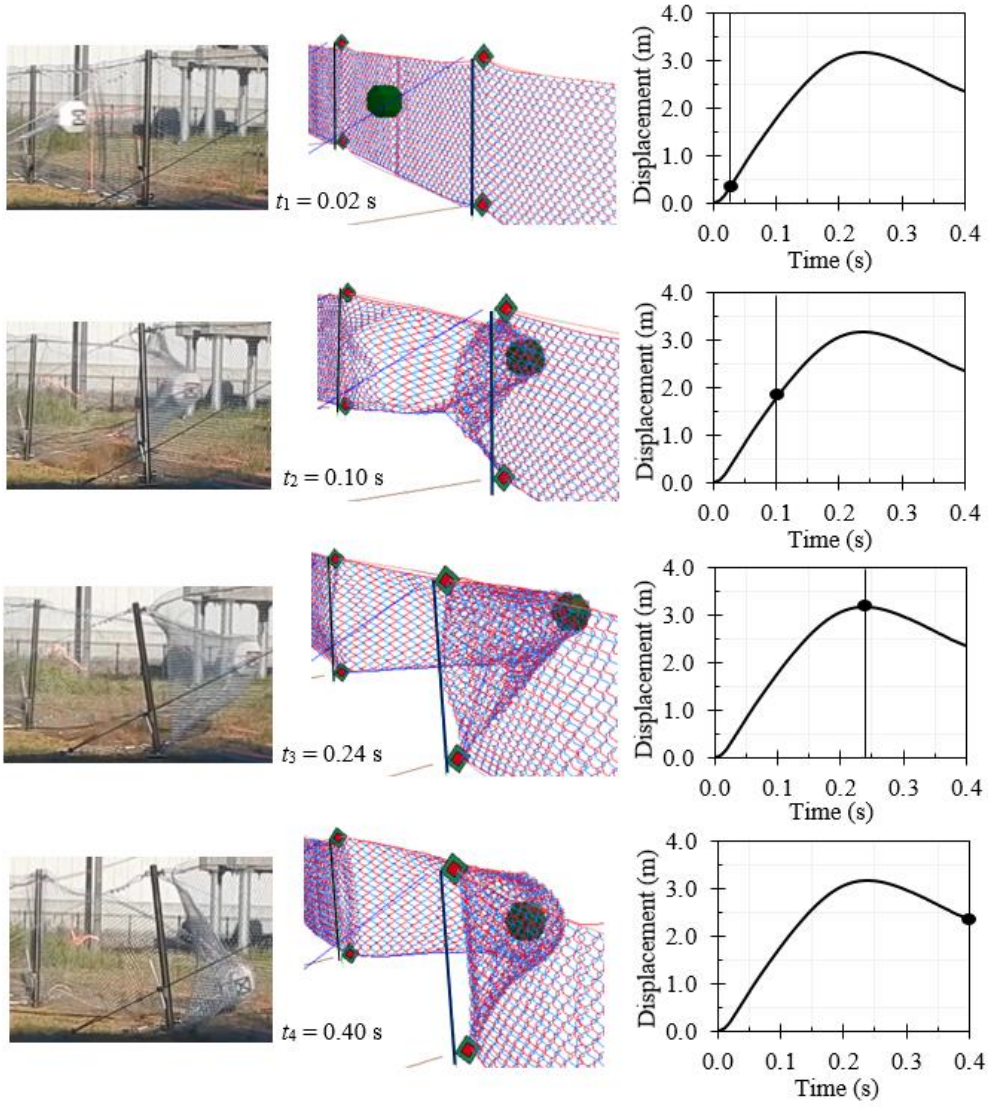

Figure 3.24 Deformation of fence at the time of 0.02 s, 0.1 s, 0.24 s and 0.4 s

It has been identified that the out-of-plane displacement may be one of the most essential performances used to estimate the effectiveness of numerical models compared to the experimental model. The fluctuation of impact force was also considered to evaluate the contact of the wire net and the rock, and the dynamic behavior of protection fence as well. Moreover,

the tension of the wire ropes and their slipping through the energy absorbers may be necessary to survey fully their efficiencies.

Firstly, the comparisons of the displacement between the experiment (Exp) and finite element method (FEM) involved a fence with a span of 5 m, 2 m posts, and the impact position at point A (case 1–1), as shown in Figure 3.24. Specifically, the first column shows a selection of the high-speed, front-view camera frames, acquired during the full-scale experiment, and the second column illustrates the deformed shapes of the corresponding model. In the third column, the time–displacement curves describe the deformation of the fence over a time period of 0.4 s. In the graphs, the black dot was marked to track the value of the maximum displacement for each frame. Four different time-points were chosen to observe the fence responses, including two before, one at the peak, and one after the impact.

The overall response of the fence was satisfactorily reproduced using the numerical simulation. The maximum displacement of the prototype derived from the camera (δ_{max} = 3.30 m) was 3 % larger than that of the simulation (δ_{max} = 3.19 m). This small difference can be attributed to the slip of the wire ropes through the energy absorbers in the numerical simulation and experiment. The deformed shapes of both the experimental and analytical models were essentially the same because they could perfectly catch the rock without breaking the wire net. Accordingly, the ability of the numerical simulation successfully replicated the fence's fundamental behavior under dynamic conditions.

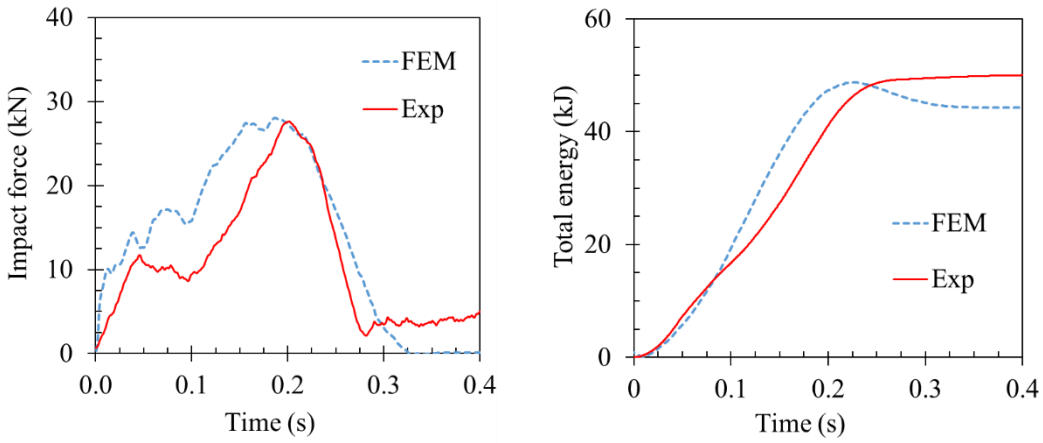

(a) Impact force (b) Total energy

Figure 3.25 Impact force and total energy between experiment and numerical simulation in case 1-1

The impact forces of case 1–1 are shown in Figure 3.25(a). It can be observed that the curves between experiment and analysis fluctuated in similar manners. The maximum values were approximately 27 kN and 28 kN in the cases of the numeric analysis and experiment, respectively, and their values peaked at approximately 0.2 s. Therefore, there were no significant differences in the shape and timing of the peak values of the two curves. In addition, the variation of the total energy is illustrated in Figure 3.25(b). The maximum value of the total energy reached 50 kJ approximately for both the experimental and numerical simulations, and there was a significant increase in the absorbed energy until it reached the maximum impact force at 0.2 s.

Lastly, the experimental and numerical simulation of rope tension in cases 1-1 and 2-1 are illustrated in Figures 3.26 and 3.27, respectively. Generally, the values agreed fairly well for the tensile force of the uphill ropes. However, the tensile ropes of experimental model tended to decrease in some positions compared to that of numerical model. For instance, the tensile force of the lateral ropes (L1, L6) in the experiment peaked at approximately 2 kN lower than those elicited by the numerical simulation in case 1-1, and their fluctuations were different. The reasons for these differences were firstly attributed to the fact that the shapes of the curves depended on the definition of the time step. The numerical values were listed every 0.002 s to decrease the analytical time. The experimental equipment was measured by a time step of 0.0005 s. Thus, the time step of the numerical simulation was larger. Therefore, the curves of the numerical solution exhibited wide variations within very short intervals, whereas the experimental variations exhibited smooth force variations. Another reason was attributed to the different values of the rope tensions caused by the slip of the wire rope through the type-M energy absorbers that were placed at the upper and bottom posts P2 and P3 in case 1-1. The maximum slipping length of the bottom post P3 observed in the experiment was 1215 mm, but that in the numerical simulation was 850 mm. Moreover, the movement of anchorage in the experimental model can lead to a decrease in the rope tension.

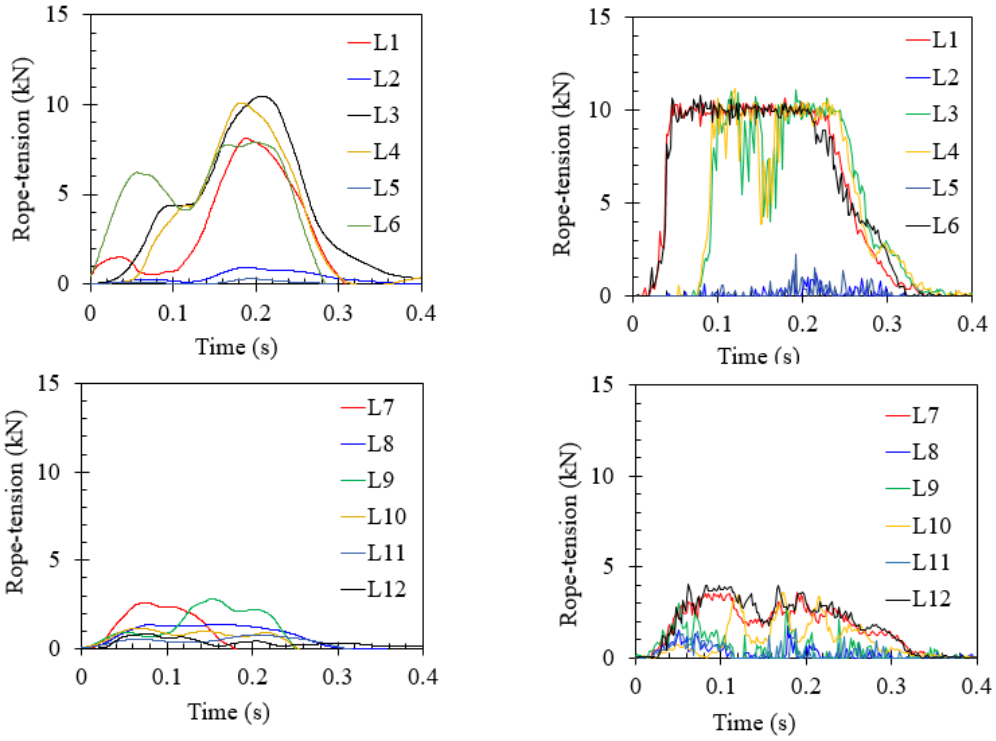

(a) Experiment (b) Numerical simulation

Figure 3.26 Time history of rope tension in case 1-1

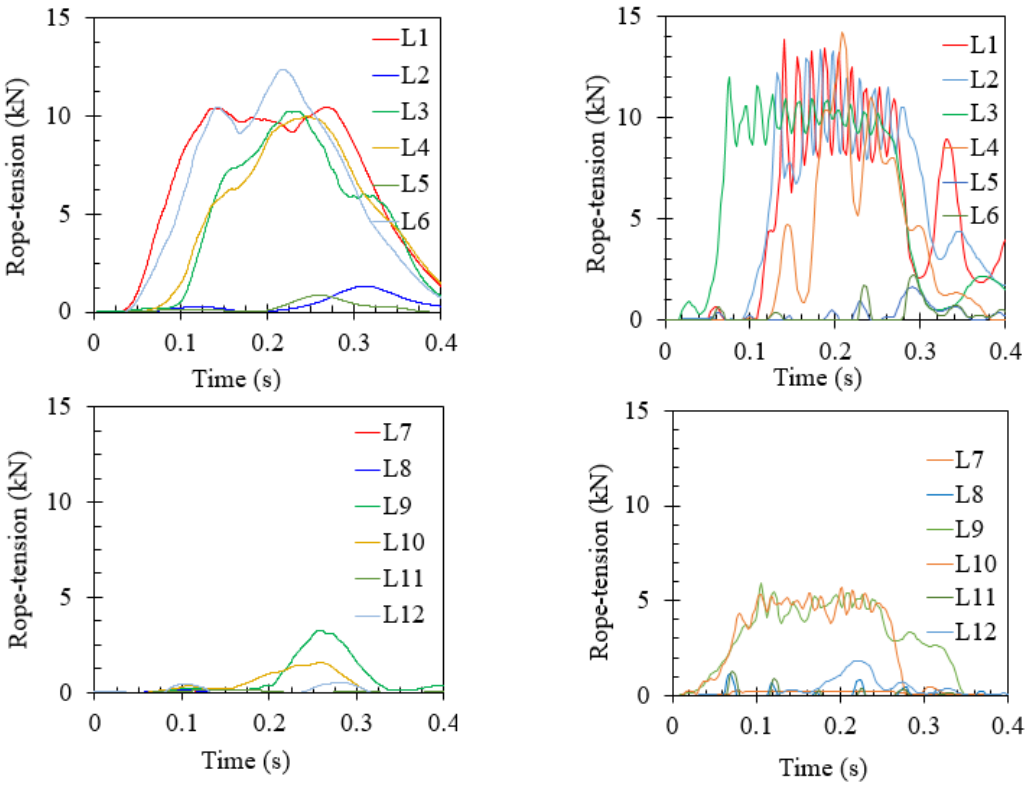

(a) Experiment (b) Numerical simulation

Figure 3.27 Time history of rope tension in case 2-1

3.5 Summary of outcomes

In horizontally experimental models, the fence with 5 m and 5.5 m spans and a post height of 2 m had successfully absorbed falling rock with a 106 kJ impact energy at different impact positions. It was verified that those fence have enough performance for the assumed design condition of rockfall. The achievement in this content are summarized as follows:

1) The maximum displacement of the fence reached 3.7 m approximately without breaking the wire net or wire ropes after it absorbed the impact energy
2) A change of the length of end spans could not effect on the result of maximum displacement
3) RC block cannot stop when the experimental models decreased 10 % length of mid-span from 5.5 m to 5m for Case 5, 6 and 7
4) The residual heights of the fence do not depend on the change of length of span when the collision occurred at the center of end span.
5) The impact force of the fence with longer spans tends to be higher that of the fence with shorter spans
6) Energy absorbers can dissipate effectively from 56 % to 71 % the total impact energy of the rockfalls
7) The rope tension reaches its maximum values when the impact occurs at the middle point of the spans.

In vertically models, the fences with 2 m and 3 m heights and a span length of 5 m had successfully absorbed falling rock with a 50 kJ impact energy , and these numerical models were also modeled successfully. The obtained results summarized as follows:

8) The maximum displacement of the fence reached 3.5 m approximately without breaking the wire net or wire ropes after it absorbed the impact energy
9) When the rockfall impacted directly the posts, the deformation of the post tended to increase when the height of the posts increased, and the impact energy was absorbed by the type-M and type-F absorbers and the deformed post
10) The protection posts of the fence with heights of 3 m could respond more effectively when the collision occurred at the middle of the span in the case of the initial impact, such as case 2–1
11) The maximum impact forces of the protection fence that corresponded to the impact energy of 50 kJ are approximately equal in the cases of the numerical analysis and experiment

12) The slipping behaviors of the wire ropes through the energy absorbers and the movement of anchorages caused a decrease in the rope tension. However, these forces increased when fences with 2 m and 3 m posts were compared
13) The energy absorbers needed to be replaced in the experimental cases in repeated impact paradigms owing to the damage of the bolts and nuts of the metal block
14) The dynamic behaviors of the numerical model, such as the motion of nodes along the wire rope, and the deformation of the wire net, were reproduced successfully
15) Advanced simulations identified the higher capacity of the protection fence with a span of 5 m and 3 m posts which could absorb an impact energy of 125 kJ
16) Some numerical simulation results agreed fairly well with experimental results, and this constituted an effective and reliable design tool in order to study the impact behavior of general structures based on these analyses.

REFERENCES

Axel Volkwein, Numerical simulation of flexible rockfall protection systems. International Conference on Computing in Civil Engineering (2005)

Christoph Berger, Yoichi Nishita, Tomohiro Fujii, Full-scale testing of rock fall barriers for small-scale impact energy. Proceedings of the 10th Symposium on Impact Problem of Structures, Japan Society of Civil Engineering. 271-276 (2010) http://library.jsce.or.jp/jsce/open/00565/2010/10-0271.pdf

Critina, G. Laura, G. Stefato, de M. Guido, G and Francesco, U. Three-dimensional numerical modelling rock protection barriers. Computers and Geotechnics. 44, 58–72 (2012)

ETAG-027, Guideline for European technical approval of falling rock protection kits, European Organization for Technical Approvals (2008)

Gerber W, Guide for the approval of rockfall protection kits. Swiss Agency for the Environment, Forests and Landscape (SAEFL) and Swiss Federal Research Institute WSL Berne (2001)

Hua Jiang, Xiaowo Wang, Shuanhai He. Numerical simulation of impact test on reinforced concrete beam. Material and Design. 39, 111–120 (2012)

Japan Road Association, Rockfall Mitigation Handbook, Maruzen (2017)

LS-DYNA Keyword user's manual Ver. 971, Livermore Software Technology Corporation, (2016)

M. Spadari, A. Giacomini, O. Buzzi, and J. P. Hambleton, Prediction of the Bullet effect for rockfall barriers, a scaling approach. Rocck Mech Rock Eng. doi 10.1007/s00603–011–0203–0 (2012)

Malvar L, Crawford J. Dynamic increase factor for steel reinforcing bars. 28th DDESB Seminar Orlando, USA (1998)

Masuya, H. and Yamamoto, M., Load resistant factor of rock-sheds in heavy snow area. Proceeding of Joint Japan Swiss Scientific Seminar on Impact Load by Rock Falls and Design of Protection Structure, 121–127 (1999)

Masuya, H., Performance based design of protection structure under impact action. Proceeding of International Symposium on Structure under Earthquake, Impact, and Blast Loading, 217–224 (2008)

P. V Tran, K. Maegawa, S. Fukada Experiments and dynamic finite element analysis of a wire-rope rockfall protective fence, Rock Mech. Rock Eng, doi 10.1007/s00603–012–0304–0 (2012)

Peila, D and Ronco, C.: Technical Note: Design of rockfall net fences and the new ETAG 027 European guideline. Nat. Hazards Earth Syst. Sci. 9, 1291–1298 (2009)

S. Dhakal, N.P. Bhsndary, R. Yatabe and N. Kinoshita Experimental, numerical and analytical modelling of a newly developed rockfall protective cable-net structure, Nat. Hazards Earth Syst. Sci. 11, 3197–3212 (2011)

S. Tachibana, H. Masuya, S. Nakamura, Performance based design of reinforced concrete beams under impact. Natural Hazards and Earth System Sciences. 10, 1069–1078 (2010)

Tam Sy Ho, Hiroshi Masuya, Finite element analysis of the dynamic behavior of sand-filled geocells subjected to impact load by rockfall. International Journal of Erosion Control Engineering (2013).

Chapter 4 Applicability for performance based design

With the aim of contributing to design and construct for externally bonded fiber-reinforced polymer (FRP) bars to the tensile region of reinforced concrete (RC) structures by Near-Surface Mounted (NSM) method, calculated equations based on codes American Concrete Institute (ACI), have been shown to predict the flexural strength of the beam and the number of strands of FRP bars. Furthermore, the additional numerical simulations of protection fence are executed with higher impact energies to gain a deeper understanding on the dynamic behavior.

4.1 Overall

The codes of externally bonded fiber-reinforced polymer (FRP) bars have been developed in Europe, Japan, Canada, and the United States. In Europe, the International Federation for Structural Concrete (FIB) published a bulletin on design guidelines for externally bonded FRP bars for RC structures (International Federation for Structural Concrete 2001). In Japan, the Japan Society of Civil Engineers (JSCE), the Japan Concrete Institute (JCI), and the Railway Technical Research Institute (RTRI) published several documents related to the use of FRP bars in concrete structures. The Canadian Standards Association (CSA) have developed guidelines for FRP systems, “Fibres reinforced structures” of Canadian Highway Bridge Design Code was completed in 2006. In the United States, standards for evaluating FRP systems are available to American Concrete Institute (ACI) such as “Guide for the Design and Construction of Externally Bonded FRP Systems for Strengthen Concrete Structures” of ACI 440.2R-08, and “Guide for the Design and Construction of Structural Concrete Reinforced with FRP Bars” of ACI 440.1R-15 and ACI 381-05.

This study involves the flowchart for application of design is shown based on the codes of ACI with the addition of calculating the number of strands of FRP bars for the implementation by NSM method. In addition, the numerical simulation of protection fence against rockfall with higher impact energy was modelled successfully and this model can aid or replace the full-scale tests, which normally incurs a large budget, and sometimes obtains the poor results.

4.2 Flowchart of design for FRP NSM method

4.2.1 Assumptions in the computation of flexural strength

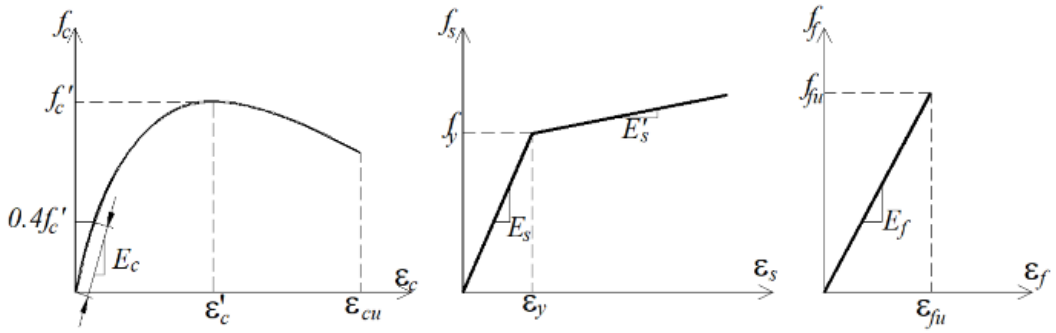

(a) Concrete (b) Reinforcing bars (c) FRP bar

Figure 4.1 Stress-strain relationship

The simple assumptions involve in principles of force equilibrium, strain compatibility, constitutive laws of the materials, and make reference to the codes of ACI 440.2R-08, ACI 440.1R-15 and ACI 381-05. The computation of the flexural strength of a cross section with an external application of FRP NSM reinforcement has used the assumptions as follows:

- The computation is based on dimensions, the arrangement of reinforcing bars, and constitutive laws of concrete, steel, and FRP bars;
- The equilibrium between tensile forces (in steel and FRP bars) and compressive forces (in concrete) always remains;
- There is no bonding failure between external FRP bars and the concrete substrate;
- The stress-strain relationship of FRP bars is linear elastic.

The constitutive of material models are assumed as bellows. Firstly, regarding the stress-strain relationship for concrete in compression as shown in Figure 4.1(a), the slope of the initial part of the diagram is reasonably constant. When the stress increases gradually, the relationship become nonlinear elastic until the peak occurs where very little extra stress causes a large increase in strain. The peak in stress is known as the compressive strength of concrete ($f_c^{'}$) and the corresponding compressive strain is denoted ($\varepsilon_c^{'}$). At a certain ultimate strain (ε_{cu}) the concrete crushes regardless of the level of stress. The maximum usable compressive strain in the concrete is assumed to 0.003.

Secondly, regarding the stress-strain relationship of reinforcing bars as shown in Figure 4.1(b), the elastic modulus (E_s) is equal to the slope of the linear portion. ACI 440. 2R-08

allows a mean value of 200.000 N/mm^2 to be assumed for E_s. The modulus in the plastic region is set as $E_s^{'} = 0.01E_s$ (W. Jung, et al, 2017). The ultimate stress is assumed as follows:

$$for\ \varepsilon_s \le \varepsilon_y \tag{4.1}$$

$$f_s = f_y + E_s^{'}(\varepsilon_s - \varepsilon_y)\ \ for\ \varepsilon_s \ge \varepsilon_y \tag{4.2}$$

Where $f_y - \varepsilon_y$ and $f_s - \varepsilon_s$ are stress-strain in the reinforcing bars at yielding and ultimate stage, respectively.

Finally, the stress-strain curve of FPR bar as shown in Figure 4.1(c) is assumed linear elastic. The material properties are reported by manufacturers including the ultimate tensile strength (f_{fu}^*) and the ultimate rupture strain (ε_{fu}^*) that typically do not consider long-term exposure to environmental conditions. Therefore, calculating the ultimate tensile strength and rupture strain is used according to the recommendation of environmental reduction factor (c_E) as shown in Table 4.1

$$\begin{aligned} f_{fu} &= c_E f_{fu}^* \\ \varepsilon_{fu} &= c_E \varepsilon_{fu}^* \end{aligned} \tag{4.3}$$

Table 4.1 Environmental reduction factor c_E

Exposure condition	Fiber type	c_E
Interior exposure	Carbon	0.95
	Glass	0.75
	Aramid	0.85
Exterior exposure (bridges, piers and unenclosed parking garages)	Carbon	0.85
	Glass	0.65
	Aramid	0.75
Aggressive environment (chemical plants and wastewater treatment plants	Carbon	0.85
	Glass	0.50
	Aramid	0.70

4.2.2 The flexural strength of rectangular section.

The distribution of strain and stress for the rectangular section under static load is illustrated in Figure 4.2. The different forces act on an RC section in sag region include the compression

(F_c) of concrete above the neutral axis (c), the tension (F_s) and compression $(F_s^{'})$ of reinforcing bars, the tension (F_{fe}) of FRP bars.

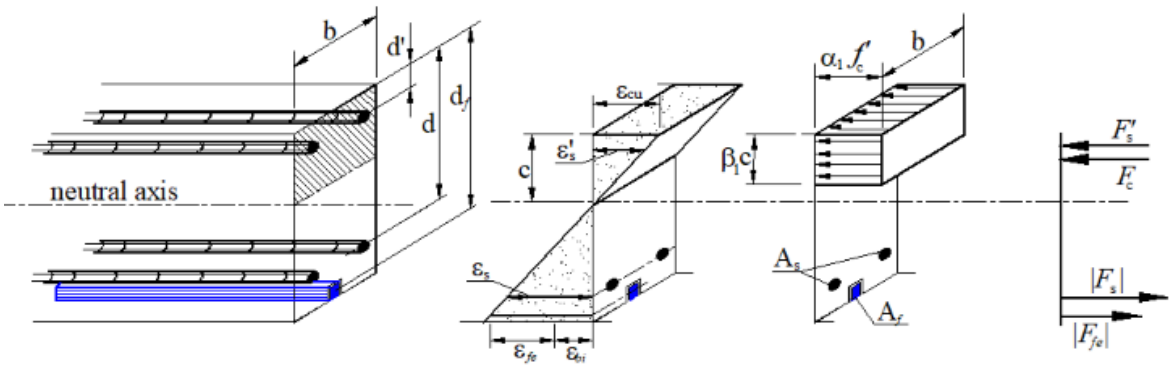

(a) Section (b) Strain distribution (c) Stress block (d) Axis force

Figure 4.2 Stress-strain distribution for a rectangular section

By equilibrium, the sum of the compressive forces have to equal zero, that is:

$$F_c + F_s^{'} - F_s - F_{fe} = 0 \tag{4.4}$$

Therefore,

$$\alpha_1 f_c^{'} \beta_1 cd + A_s^{'} f_s^{'} - A_s f_s - A_f f_{fe} = 0 \tag{4.5}$$

where A_s, f_s are the area and stress of the tensile area of reinforcing bars, $A_s^{'}$, $f_s^{'}$ are the area and stress of the compressive area of reinforcing bars, A_f, f_{fe} are the area and effective stress of FRP bars, b is width of compression face of beam. The concrete stress block factors (α_1, β_1) relate to the depth of equivalent rectangular stress block and depth of neutral axis depth (c). ACI 381-05 calculates the factors based on the parabolic stress-strain relationship for concrete as follows:

$$\beta_1 = \frac{4\varepsilon_c^{'} - \varepsilon_c}{6\varepsilon_c^{'} - 2\varepsilon_c} \tag{4.6}$$

$$\alpha_1 = \frac{3\varepsilon_c^{'}\varepsilon_c - \varepsilon_c^2}{3\beta_1 \varepsilon_c^{'}} \tag{4.7}$$

where $(\varepsilon_c^{'})$ is strain corresponding to the compressive strength of concrete $(f_c^{'})$ calculated as follows:

$$\varepsilon_c^{'} = \frac{1.7 f_c^{'}}{E_c} \tag{4.8}$$

An assumption of the depth to neutral axis (c) is described by a trial-and-error method (ACI 440.2R-08). The initial assumption of neutral axis (c) is 0.2d (d is distance from extreme compression to the centroid of tension reinforcement) to calculate the level of strain and stress corresponding to concrete, steel and FRP bar, and to check the internal force equilibrium afterward. If the result is different with the initial assumption, the calculation procedure needs to be repeated by using the revised assumption.

For any assumption of the depth to the neutral axis, the strain level in concrete (ε_c) the tensile (ε_s) and compressive $(\varepsilon_s^{'})$ strain of reinforcing bars, and FRP bar (ε_{fe}) can be calculated by similar triangles as follows:

$$\varepsilon_c = \left(\varepsilon_{fe} + \varepsilon_{bi}\right)\left(\frac{c}{d_f - c}\right) \tag{4.9}$$

$$\varepsilon_{fe} = \varepsilon_{cu}\left(\frac{d_f - c}{c}\right) - \varepsilon_{bi} \le \kappa_m \varepsilon_{fu} \tag{4.10}$$

$$\varepsilon_s = \left(\varepsilon_{fe} + \varepsilon_{bi}\right)\left(\frac{d - c}{d_f - c}\right) \tag{4.11}$$

$$\varepsilon_s^{'} = \varepsilon_{cu}\left(\frac{c - d^{'}}{c}\right) \tag{4.12}$$

where κ_m is a bond dependent coefficient to limit the strain in the FRP reinforcement, and ACI 440.2R-08 allows a value of κ_m from 0.6 to 0.9. ε_{fu} is the design rupture strain of FRP bars, d_f is the effective depth of FRP bars, $d^{'}$ is the distance from extreme compression to the centroid of compression reinforcement. The initial strain level on bonded substrate (ε_{bi}) can be determined from the moment of dead loads (M_{DL}) and second moment of inertia (I_{cr}) as shown in Equation 4.13.

$$\varepsilon_{bi} = \frac{M_{DL}\left(d_f - k.d\right)}{I_{cr}E_c} \tag{4. 13}$$

Here,

$$\mathrm{k} = \sqrt{2\rho\mathrm{n} + \left(\rho n\right)^2} - \rho n \tag{4. 14}$$

$$\rho = \frac{A_s}{bd}; n = \frac{E_s}{E_c} \tag{4. 15}$$

where *k* is the ratio of the depth of neutral axis to reinforcement depth measured from extreme compression fiber, *n* is the modular ratio of elasticity between steel and concrete, ρ is reinforcement ratio, *b* is width of compression face of the member.

The moment-curvature distribution of RC beams strengthened by FRP NSM method can be classified into three cases. Firstly, the cracking moment (M_{cr}) is given by Equation 4.16, where the gross second moment (I_g) neglects presence of reinforcement. Secondly, yielding moment (M_y) involves in the stress curve of reinforcing bars that is not beyond the yield stress yet as shown in Equation 4.17. Finally, maximum moment (M_n) occurs at the post-yielding stage as shown in Equation 4.18. Calculation for these moments is respectively based on the equilibrium of all forces as follows:

$$M_{cr} = \frac{0.62\sqrt{f_c^{'} I_g}}{y_t} \tag{4.16}$$

$$M_y = A_s f_y \left(d - \frac{\beta_1 c}{2} \right) + \psi_f A_f f_{fe} \left(d_f - \frac{\beta_1 c}{2} \right) - A_s^{'} f_s^{'} \left(d^{'} - \frac{\beta_1 c}{2} \right) \tag{4.17}$$

$$\phi M_n = \phi \left[A_s [f_y + E_s^{'} (\varepsilon_s - \varepsilon_y)] \left(d - \frac{\beta_1 c}{2} \right) + \psi_f A_f f_{fe} \left(d_f - \frac{\beta_1 c}{2} \right) - A_s^{'} f^{'}_s \left(d^{'} - \frac{\beta_1 c}{2} \right) \right] \tag{4.18}$$

where y_t is the distance from centroid axis of the gross section to tension face, ψ_f is an addition reduction factor of 0.85 recommended to take into account for the strength contribution of FRP bars (ACI 440.2R-08). The strength reduction factor (ϕ) is given by Equation 4.19.

$$\phi = \begin{cases} 0.9 \, for, \varepsilon_s \geq 0.005 \\ 0.65 + \dfrac{0.25(\varepsilon_s - \varepsilon_y)}{0.005 - \varepsilon_y} \, for, \varepsilon_y < \varepsilon_s < 0.005 \\ 0.65 \, for, \varepsilon_s \leq \varepsilon_y \end{cases} \tag{4.19}$$

4.2.3 Flowchart of FRP NSM method.

The design flexural strength of the beams (M_n) is required exceedingly the factored moment (M_u) as indicated by (20). The design flexural strength refers to the nominal strength of the beams multiplied by a strength reduction factor (ϕ) as shown in Equation 4.19, and the factored moment (M_u) at a section refers to the moment calculated from the dead-load moment (M_{DL}) and live-load moment (M_{LL}) given by Equation 4.21.

$$\phi M_n \geq M_u \tag{4.20}$$

$$M_u = 1.1M_{DL} + 0.75M_{LL} \tag{4.21}$$

NSM method consists of installing rectangular or circular FRP bars in a groove cut into the concrete surface and bonded in place using an adhesive as shown in Figure 4.3. The groove should be dimensioned to ensure adequate adhesive around the bars, and typical groove dimensions for various types of FRP bar are referred to Abdullah and Kadir, 2016. For FRP round bars, the minimum dimension of the grooves should be taken at least 1.5 times the diameter of the FRP bars. For FRP rectangular bars, the minimum size of groove is $3.0a_f \times 1.5b_f$ (a_f, b_f are the width and height of FRP bar). The space of grooves for FRP bars should be greater than twice the depth of the groove to avoid overlapping of the tensile stresses around the FRP bars. In addition, a clear edges distance of four times the depth of the NSM groove should be provided to minimize the debonding failure of FRP bars (ACI 440.2R-08). Flowchart to design FRP NSM method for the beams is shown in Figure 4.4.

The physical properties of materials made FRP bars are summarized in Table 4.2. In this study, these properties are referred to the Tonen Corporation including density (ρ) of 1.8 g/cm^3, tensile strength (f_{fu}^*) of 3990 MPa, strain (ε_{fu}^*) of 0.0168 mm/mm and modulus of elasticity (E_f) of 237 GPa corresponding to Forca Tow Anchors (FTA-C1-48-250 and FTA-C1-72-250) of Nippon Steel Sumikin Co., Ltd. The area of FRP bars is given by Equation 4.22, where g is fineness and n' is the number of strands per a sheet.

$$A_f = \frac{g.n'}{\rho} \times 1000 \tag{4.22}$$

When calculating the area (A_f) of externally bonded FRP bars, its initial assumption can be $0.333b$ (b is the width of the cross section). The length of FRP bar depends on many factors such as cross-sectional shape, dimensions, and material properties. The equilibrium condition of FRP bars with an embedded length involves its developed length (l_d). According to a triangular stress distribution, the average bond strength (τ_b) can be half of the maximum bond strength ($\tau_{\max}$). Average bond strength for FRP bars can range from 3.5 to 20.7 MPa (ACI 440.1R-15), the following equations for development length can be given:

$$l_d = \frac{d_f}{4(\tau_b)} f_{fe} \text{ for round bars} \tag{4.23}$$

$$l_d = \frac{a_f \times b_f}{2(a_f + b_f)\tau_b} f_{fe} \text{ for rectangular bars} \tag{4. 24}$$

Table 4.2 Physical properties of FRP bar

Properties	GFRP	CFRP	AFRP
Typical density (ρ) g/cm^3	11.25 to 2.10	1.50 to 1.60	1.25 to 1.40
Tension strength (f_{fu}^*) Mpa	483 to 690	600 to 3690	1720 to 2540
Elastis modulus $(E_f)\times 10^3$ Gpa	35.0 to 51.0	120.0 to 580.0	41.0 to 125.0
Rupture strain, percent	1.2 to 3.1	0.5 to 1.7	1.9 to 4.4

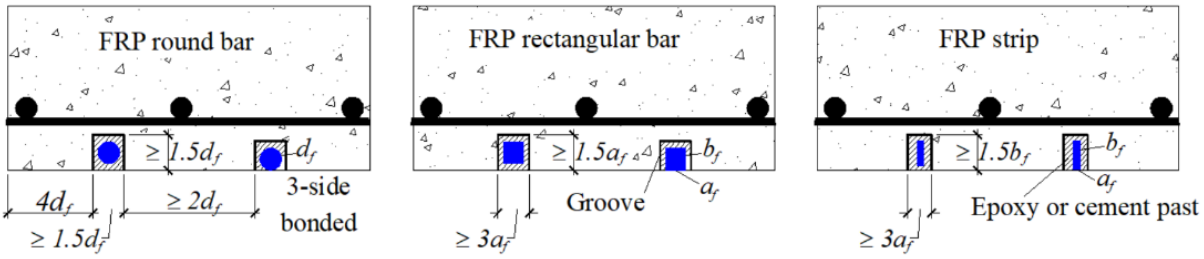

Figure 4.3 Variety of FRP bars and minimum dimensions of grooves

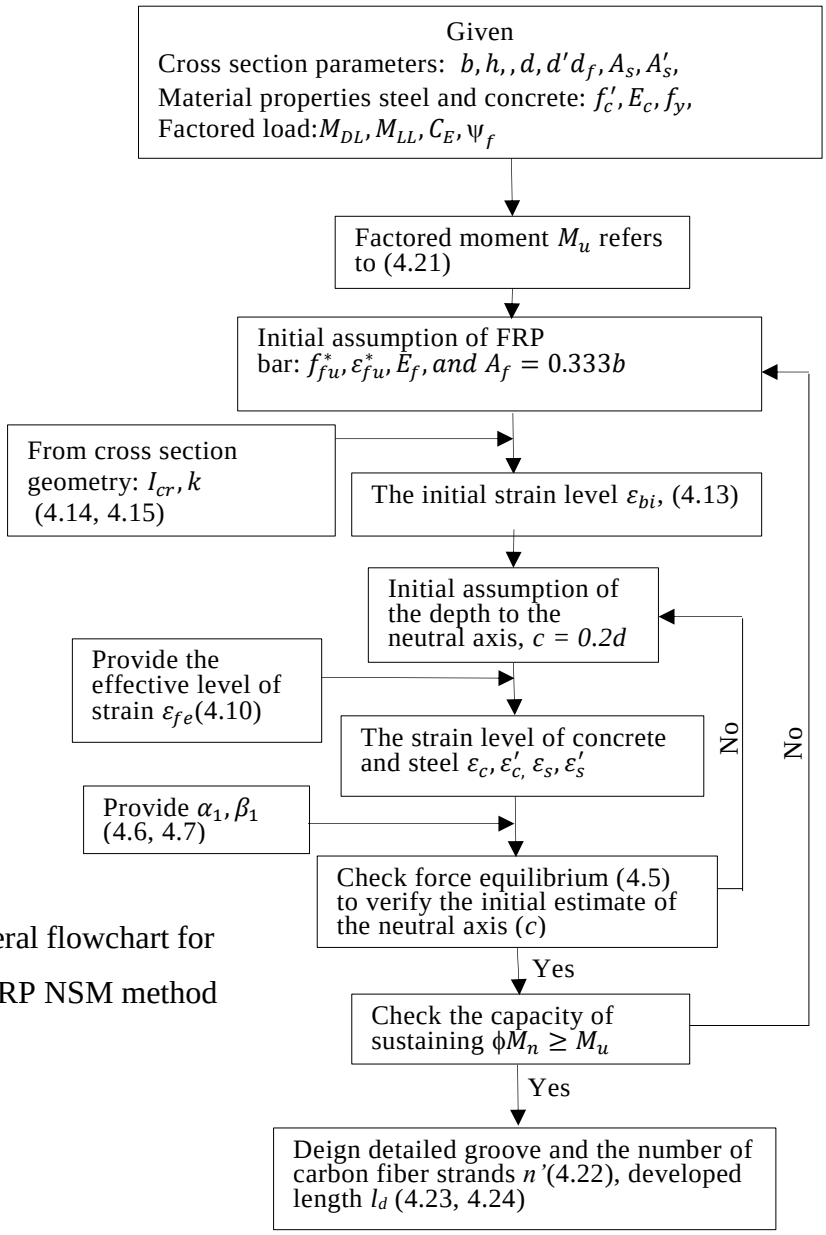

Figure 4.4 General flowchart for application of FRP NSM method

4.2.4 Verification and design FRP NSM method

Table 4.3 Results of experiment and theory and simulation

Specimens		SR48-1	SR48-2	SR72-1	SR72-2
Yielding Moment (kN·m)	Experiment	58.13	60.00	61.13	61.88
	Theory	58.35	58.35	66.20	66.20
	Simulation by FEM	61.88	61.88	63.75	63.75
	(Experiment-Theory)/Theory (%)	*-0.39*	*2.83*	*-7.67*	*-6.53*
	(Simulation-Theory)/Theory (%)	*6.04*	*6.04*	*-3.70*	*-3.70*
Maximum Moment (kN·m)	Experiment	67.13	70.50	71.25	74.63
	Theory	67.98	67.98	75.75	75.75
	Simulation by FEM	67.50	67.50	72.00	72.00
	(Experiment-Theory)/Theory (%)	*-1.26*	*3.71*	*-5.94*	*-1.49*
	(Simulation-Theory)/Theory (%)	*-0.71*	*-0.71*	*-4.95*	*-4.95*

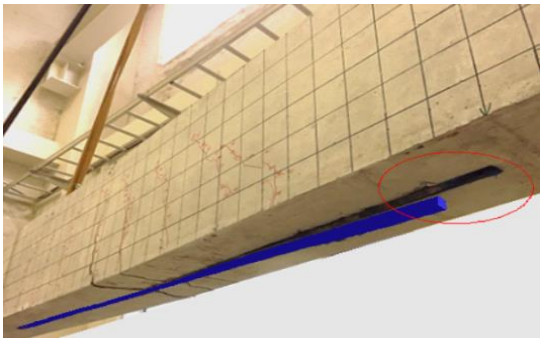

Figure 4.5 Peeling of FRP bar, beam SR48-1

Table 4.3 compares the values of yielding moment and maximum moment for specimens computed from experiment, numerical simulation and theory. The experimental and numerical values are evaluated by the schematic of the applied load with $M_n = 0.235Pl$ $(l = 1600mm)$ and the theoretical values are calculated by the code of ACI (the maximum moment of beam SR48 is shown in appendix A). For the yielding moment, the discrepancy between experimental and theoretical results ranges from 0.39 % to 7.67 % and between simulation and theory accounts for from 3.7 % to 6.04 %. While, this discrepancy trends to be less for the maximum moment, nearly from 1.26 % to 5.94 % between experiment and theory, and from 0.71 % to 4.95 % between simulation and theory. It can be said that the calculated equations in this study can predict the static ultimate flexural strength of RC beams strengthened by FRP NSM method

with relatively high accuracy, and the results of experiment and numerical simulation are reliable as well.

When comparing the calculated values, a small error of under 8% can be explained by the initial assumptions. While some of these initial assumptions are necessary for the sake of computational ease, the assumptions do not accurately reflect the true fundamental behavior of FRP bars by NSM method. In the experimental procedure, bonding failure at the epoxy-concrete interface caused by peeling of FRP bars and the substrate of concrete as shown in Figure 4.5. Whereas the initial assumption did not consider such a separation.

4.3 Additional numerical simulations of protection fence

Figure 4.6 Performance of catching rockfall with impact energy of 125 kJ of vertical model

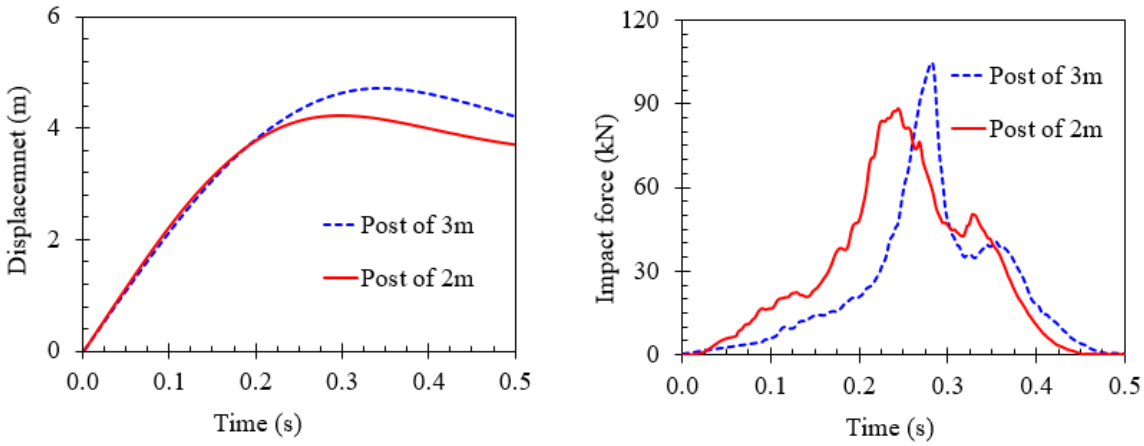

(a) Displacement (b) Impact force

Figure 4.7 Impact force and displacement at position C with impact energy of 125kJ

From the experimental observations, the protection fences designed verically with the span of 5 m, and 2 m and 3 m posts, were able to perform with a greater capacity for dissipating the impact energy of 50 kJ based on a rational arrangement of the energy absorbers. However, it was difficult to carry out additional experiments to confirm this. Therefore, the numerical models were carried out with higher impact energies to gain a deeper understanding on the

dynamic behavior of the protection fence. In order to determine the capacity of energy absorption, many numerical analyses have been carried out by the gradual increase of the impact energy at 25 kJ increments, resulting in impact energies of 75 kJ, 100 kJ, and 125 kJ, for the fence with a span of 5 m and 2 m and 3 m posts.

As expected, the numerical model of the simulated protection fence with a span of 5 m and a post of 3 m can also capture successfully rockfall at the impact energy of 125 kJ at position C, as shown in Figure 4.6. In this case, the maximum displacement was approximately 4.71 m, as shown in Figure 4.7(a). Compared to this value, the maximum displacement of 5 m was elicited in the case of the fence with a span of 10 m, a post of 3 m, and an impact energy of 100 kJ (Berger et al., 2010). Based on the performance of this structure, the fence with a span of 5 m and a post of 3 m was effective and rational. Moreover, advanced simulation can identify increases in the impact force on the fence in terms of the height of the post. Comparison of the fences with 2 m and 3 m posts, respectively elicited force peaks at 85 kN and 100 kN, as shown in Figure 4.7(b).

4.4 Summary of outcomes

In this chapter, the calculated equations based on codes ACI are present to calculate the flexural strength of the beam with and without the strengthening of FRP NSM method under static load. Moreover, the simulation of vertical fence is added to survey its dynamic behavior under higher impact energies. The achievements of chapter are summarized as follows:

1) The flexural strength of RC beams strengthened FRP NSM method can be calculated accurately by the use of two guides published by ACI
2) When comparing the yield and maximum moment values of the beams, the values calculated from experiment, theory and simulation is less than 8 %.
3) The flowchart for application of design is shown based on the code of ACI with the addition of calculating the number of strands of FRP bars for the implementation by NSM method
4) Advanced simulations identified the higher capacity of the protection fence with a span of 5 m and 3 m posts which could absorb an impact energy of 125 kJ
5) Some numerical simulation results agreed fairly well with experimental results, and this constituted an effective and reliable design tool in order to study the impact behavior of general structures based on these analyses

Appendix

APPENDIX A. The flexural strength of beam SR48

Example illustrates the design of flexural strength of RC beam strengthened by 48 CFS by NSM method as shown in Figure 4.8 and material properties are described in Table 4.4. The steps of calculation are presented as follows:

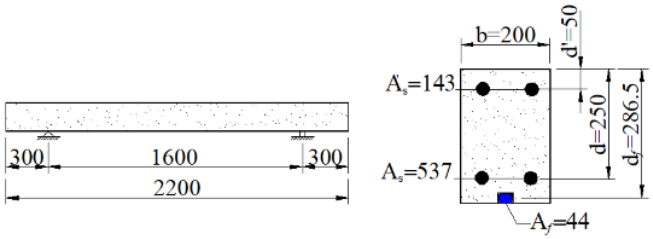

Figure 4.8 Schematic of the idealized simply supported beam with FRP bar. Unit: N, mm

Table 4.4 Material properties

Material	Properties	Value	Unit
Concrete	Compressive strength of concrete, f_c'	35.81	N/mm^2
	Young modulus, E_c	28.43	kN/mm^2
Steel	The strain of yielding stage, f_y	345	N/mm^2
FRP (48 carbon fiber strands)	Ultimate tensile strength, f_{fu}^*	3990	N/mm^2
	Rupture strain, ε_{fu}^*	0.0168	mm/mm
	Modulus of elastic E_f	237	kN/mm^2

1. Determining the design values of FRP bar by the use of environmental reduction factor as shown in Table 1, where c_E = 0.95

$$f_{fu} = c_E f_{fu}^* = 0.95 \times 3990 = 3790.5 N / mm^2$$
$$\varepsilon_{fu} = c_E \varepsilon_{fu}^* = 0.95 \times 0.0168 = 0.0159 mm / mm$$

2. Calculating the initial strain level on the bonded substrate (ε_{bi}) by (4.13). The analysis of cracked section relates to k = 0.329, I_{cr} =167×10^6 mm^4 and the dead-load moment (M_{DL}) is 29 kN·m

$$\varepsilon_{bi} = \frac{M_{DL}\left(d_f - k.d\right)}{I_{cr} E_c} = \frac{29 \times 10^6 \left(286.5 - 0.329 \times 250\right)}{167 \times 10^6 \times 28.430}$$
$$\Rightarrow \varepsilon_{bi} = 0.0012 mm / mm$$

3. Assuming initially the depth to the neutral axis, $c = 0.2d = 0.2\times250 = 50$ mm, this value is adjusted after checking equilibrium.
4. Confirming the effective level of strain in the FRP bar by (4.10), where the dimensionless bond-dependent coefficient for flexural, $\kappa_m = 0.6$

$$\varepsilon_{fe} = \varepsilon_{cu}\left(\frac{d_f - c}{c}\right) - \varepsilon_{bi} = 0.003\left(\frac{286.5-50}{50}\right) - 0.0012$$
$$= 0.0129 mm/mm > \kappa_m \varepsilon_{fu}$$
$$\left(\kappa_m \varepsilon_{fu} = 0.6\times0.0159 = 0.0096 mm/mm\right)$$

Hence, $\varepsilon_{fu} = 0.0096 mm/mm$

5. Determining the level of strains in concrete and reinforcing bars by (4.9, 4.11, 4.12).

$$\varepsilon_c = \left(\varepsilon_{fe} + \varepsilon_{bi}\right)\left(\frac{c}{d_f - c}\right) = \left(0.0096 + 0.0012\right)\left(\frac{50}{286.5-50}\right) = 0.0023 mm/mm$$

$$\varepsilon_s = \left(\varepsilon_{fe} + \varepsilon_{bi}\right)\left(\frac{d - c}{d_f - c}\right) = \left(0.0096 + 0.0012\right)\left(\frac{250-50}{286.5-50}\right) = 0.0092 mm/mm$$

$$\varepsilon_s^{'} = \varepsilon_{cu}\left(\frac{c - d'}{c}\right) = \left(\frac{50-50}{50}\right) = 0$$

6. Determining the level of stress the reinforcing bars and FRP bar from Hooke's law:

$$f_s = E_s \times \varepsilon_s = 200,000\times0.0092 = 1830.6 N/mm^2$$
$$\Rightarrow f_s > f_y = 345 N/mm^2$$
$$f_{fe} = E_{fe} \times \varepsilon_{fe} = 237,000\times0.0096 = 2269.5 N/mm^2$$

7. Checking force equilibrium to verify the initial assumption of the neutral axis (c), where the parameters of $\alpha_1, \beta_1, \varepsilon_c^{'}$ are calculated as shown in (4.6, 4.7, 4.8), respectively.

$$\varepsilon_c^{'} = \frac{1.7 f_c^{'}}{E_c} = \frac{1.7\times35.81}{28,430} = 0.0021 mm/mm$$

$$\beta_1 = \frac{4\varepsilon_c^{'} - \varepsilon_c}{6\varepsilon_c^{'} - 2\varepsilon_c} = \frac{4\times0.0021 - 0.0023}{6\times0.0021 - 2\times0.0023} = 0.759$$

$$\alpha_1 = \frac{3\varepsilon_c^{'}\varepsilon_c - \varepsilon_c^2}{3\beta_1\varepsilon_c^{'}} = \frac{3\times0.0021\times0.0023 - 0.0023^2}{3\times0.759\times0.0021} = 0.907$$

$$c = \frac{573\times345 + 44\times2269.5}{0.907\times35.81\times0.759\times200} = 60.39 mm \neq 50 mm$$

Revising the assumption of the neutral axis (c), and repeating from steps 4 to 7 until the equilibrium is achieved.

8. Adjusting the depth to the neutral axis (c = 56.94 mm) until the equilibrium is satisfied and the final results are ε_s = 0.0091, β_1 = 0.786, α_1 = 0.928

$$c = \frac{573 \times 345 + 44 \times 2269.5}{0.928 \times 35.81 \times 0.786 \times 200} = 56.94mm$$

9. Calculating the maximum moment based on Equation 4.18.
   - The contribution of steel bars in the tension region:

$$M_s = 573\left[345 + 2000\left(0.0091 - 0.0017\right)\right]\left(250 + 0.5 \times 0.786 \times 56.94\right)$$
$$\Rightarrow M_s = 46.92kN \cdot m$$

   - The contribution of FRP bars:

$$M_f = 44 \times 2269.5\left(286.5 - 0.5 \times 0.786 \times 56.94\right)$$
$$\Rightarrow M_f = 26.37kN \cdot m$$

   - The contribution of steel bars in the compression region:

$$M_{s'} = 142.7 \times 345\left(50 - 0.5 \times 0.786 \times 56.94\right)$$
$$\Rightarrow M_{s'} = 1.36kN \cdot m$$

   - The maximum moment

$$M_n = 46.92 + 0.85 \times 26.37 - 1.36$$
$$\Rightarrow M_n = 67.98kN \cdot m$$

APPENDIX B. Design for FRP NSM method

Figure 4.9 illustrates the dimension of FRP bar and material properties of concrete and steel are described in Table 4.4. The steps of design are presented as follows:

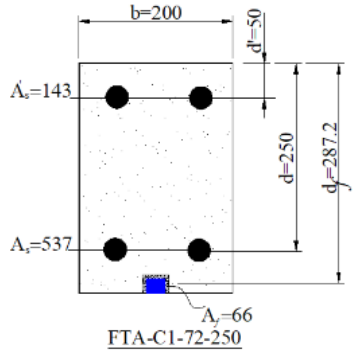

Figure 4.9 Section of strengthened beam.
Unit: N, mm

1. Determining factored moment (M_u) as shown in (4.21) with assumption M_{DL} = 29 kN·m, and the live moment (M_{LL}) is assumed to be 45 k N·m

$$M_u = 1.1M_{DL} + 0.75M_{LL} = 1.1\times 29 + 0.75\times 45$$
$$\Rightarrow M_u = 65.65kN\cdot m$$

2. Determining the design values of FRP bar using the environmental reduction factor as shown in (4.3) with $C_E = 0.95$ and preliminary calculating the area (A_f) of externally bonded FRP bar is asumpted to be $0.333b$

$$f_{fu} = C_E f_{fu}^* = 0.95\times 3990 = 3790.5N/mm^2$$
$$\varepsilon_{fu} = C_E\varepsilon_{fu}^* = 0.95\times 0.0168 = 0.0159mm/mm$$
$$A_f = 0.333b = 0.333\times 200 \approx 66mm^2$$

3. Calculating the initial strain level on bonded substrate (ε_{bi}) by (4.13) with k= 0.329; M_{DL}= 29 kN·m and I_{cr} =175×10^6 mm^4

$$\varepsilon_{bi} = \frac{M_{DL}\left(d_f - k.d\right)}{I_{cr}E_c} = \frac{29\times 10^6\left(287.2 - 0.329\times 250\right)}{175\times 10^6\times 28.430}$$
$$\Rightarrow \varepsilon_{bi} = 0.0011mm/mm$$

4. Assuming and adjusting the depth to the neutral axis (c) until the equilibrium is satisfied and the final results are:

c = 64.8 mm, β_1 = 0.851, ε_s = 0.0096, f_{fe} = 2269.5 N/mm^2

5. Calculating the ultimate flexural strength of the section by (4.18), where ϕ = 0.9

$$M_n = M_s + \omega M_f - M_{s'} = 45.98 + 0.85\times 36.31 - 1.10$$
$$\Rightarrow \phi M_n = 0.9\times 75.75 = 68.17kN\cdot m > M_u = 65.65kN\cdot m$$
The required design of the flexural strength exceed the factored moment.

6. Designing the details of FRP bar by (4.24).
The number of FRP (density and fineness show in Table 4.2)

$$n' = \frac{A_f\times\rho}{g} = \frac{66\times 1.8\times 1000}{1650} = 72strands$$
(FTA-C1-72-205)

The dimensions of groove

$$3a_f\times 3a_f = (25\times 25)mm$$
$$(3a_f = 3\sqrt{66} \approx 25mm \Rightarrow a_f = b_f = 8.3mm)$$

The developed length of FRP bar
$$l_d = \frac{a_f\times b_f}{2\left(a_f + b_f\right)\tau_b} f_{fe} = \frac{8.3\times 8.3}{2\left(8.3+8.3\right)6.9}2269.5$$
$$\Rightarrow l_d \approx 685mm$$

References

A. H. Abdullah, M. R. A. Kadir, “NSM FRP Reinforcement for Strengthening Reinforced Concrete Beams-Overview,” ZANCO Journal of Pure and Applied Sciences, vol. 28, pp. 178-200, 2016.

ACI 318-05, “Building Code Requirements for Structural Concrete,” American Concrete Institute, 2005.

ACI 440.1R-15, “Guide for the Design and Construction of Structural Concrete Reinforced with Fiber-Reinforced Polume (FRP) Bars,” American Concrete Institute, 2015.

ACI 440.2R-08, “Guide for the Design and Construction of Externally Bonded FRP Systems for Strengthening Concrete Structures,” American Concrete Institute, 2008.

Christoph Berger, Yoichi Nishita, Tomohiro Fujii, Full-scale testing of rock fall barriers for small-scale impact energy. Proceedings of the 10th Symposium on Impact Problem of Structures, Japan Society of Civil Engineering. 271-276 (2010) http://library.jsce.or.jp/jsce/open/00565/2010/10-0271.pdf

Critina, G. Laura, G. Stefato, de M. Guido, G and Francesco, U. Three-dimensional numerical modelling rock protection barriers. Computers and Geotechnics. 44, 58–72 (2012)

ETAG-027, Guideline for European technical approval of falling rock protection kits, European Organization for Technical Approvals (2008)

LS-DYNA “Keyword user’s manual,” Livermore Software Technology Corporation, 2016.

P. V Tran, K. Maegawa, S. Fukada Experiments and dynamic finite element analysis of a wire-rope rockfall protective fence, Rock Mech. Rock Eng, doi 10.1007/s00603–012–0304–0 (2012)

Peila, D and Ronco, C.: Technical Note: Design of rockfall net fences and the new ETAG 027 European guideline. Nat. Hazards Earth Syst. Sci. 9, 1291–1298 (2009)

R. Parretti and A. Nanni, “Strengthening of RC Members Using Near-Surface Mounted FRP Composite: Design Overview,” Journal of Advances in Structural Engineering, Vol. 7 No. 5, 2004.

S. Dhakal, N.P. Bhsndary, R. Yatabe and N. Kinoshita Experimental, numerical and analytical modelling of a newly developed rockfall protective cable-net structure, Nat. Hazards Earth Syst. Sci. 11, 3197–3212 (2011)

W. Jung, J. Park et al., “Flexural Behavior of Concrete Beam Strengthened by Near-Surface Mounted CFRP Reinforcement Using Equivalent Section Model,” Journal of Hidawi, Advances in Materials Science and Engineering, Article ID 9180624, 2017.

Chapter 5 Conclusions

In this study, a series of impact tests conducted on reinforced concrete (RC) beams strengthened with fiber-reinforced polymer (FRP) bar by Near-Surface Mounted (NSM) method and protection fences against low-to-medium impact energy. The results obtained are shown below

1. It can be said that the technique of externally bonded FRP bars by NSM method to tensile side of RC structures effects reliably on their flexural strength. This research contributes a better understanding of the influence of FRP NSM method on the static and dynamic behaviors of RC beams.

2. The externally bonded FRP bars to the tensile region of RC beams by NSM method has enhanced clearly in the flexural strength, and resisted to the expansion of cracks under static and impact loading condition. Strengthened beams performed the clearest linear elastic behavior until the applied static load over 150 kN, and the tensile capacity of FRP bar can achieve nearly 50% its design capacity under ultimate load. The strengthened beams finally discontinued due to peeling of FPR bars from the substrate under static and impact load. Therefore, the reinforcement of FRP NSM method with 48 and 72 fiber strands do not positive effect on the impact characteristics such as impact force, reaction force and the time duration.

3. Numerical simulation results agreed fairly well with experimental results, and this constituted an effective and reliable design tool in order to study the static and dynamic behavior of general structures based on the assumptions of constitutive models and contact conditions of the components of the beam. This study is considered to be preliminary in reference to the use of numerical models for replacing or modifying the parameters of the full-scale tests with externally bonded FRP systems.

4. When comparing the yield and maximum moment values of the beams, the values calculated from experiment, theory, and simulation is less only than 8 %, so the flexural strength of RC beams strengthened FRP NSM method in this case can be calculated accurately by the use of two guides published by ACI. The flowchart for application of design is shown based on the codes of ACI with the addition of calculating the number of strands of FRP bars for the implementation by NSM method.

5. Regarding protection fences, actually, the experimental models in this study are also possessed some specifications involved the previous studies, such as building structural components or applying the pendulum method in impact tests. However, this study is carried out to meet construction needs at the mountain areas in Japan. Therefore, these fences are designed more rationally about the length of span, the height of posts, and the arrangement of energy absorbers, but their dynamic behaviors in terms of the absorbed capacity of impact energy, displacement, rope tensions, etc. perform well as that of previous studies.

6. In horizontally experimental models, the fence with 5 m and 5.5 m spans and a post height of 2 m had successfully absorbed falling rock with a 106 kJ impact energy at different impact positions. The maximum displacement of the fence reached 3.7 m approximately without breaking the wire net or wire ropes. RC block cannot stop when the experimental models decreased 10 % length of mid-span from 5.5 m to 5m. The residual heights of the fence do not depend on the change of length of span when the collision occurred at the center of end span. Energy absorbers can dissipate effectively from 56 % to 71 % the total impact energy of the rockfalls.

7. In vertically models, the fences with 2 m and 3 m heights and a span length of 5 m had successfully absorbed falling rock with a 50 kJ impact energy. The maximum displacement of the fence reached 3.5 m when the rockfall impacted at middle span, and the deformation of the post tended to increase when the height of the posts increased. The posts of the fence with heights of 3 m could respond more effectively when the collision occurred at the middle of the span in the case of the initial impact. The maximum impact forces of the protection fence that corresponded to the impact energy of 50 kJ are approximately equal in the cases of the numerical analysis and experiment. Moreover, advanced simulations identified the higher capacity of the protection fence with a span of 5 m and 3 m posts, which could absorb an impact energy of 125 kJ.

8. Although this study has obtained noticeable achievements, limitations are unavoidable. Firstly, there is no control the peeling of FPR bars from the substrate under static and impact load. Secondly, the study ignores the effect of shear strength of strengthened beams, and how to strengthen FRP bars prevents shear cracks as well. Finally, the impact speed of rockfall is not so high, but the strain rate is high around the collision point. The strain rate effect is not still considered in this case.